THE UNIVERSITY OF CHICAGO

DEVELOPMENT OF ERBIUM-DOPED OXIDE THIN FILMS FOR QUANTUM COMMUNICATION PLATFORMS

A DISSERTATION SUBMITTED TO
THE FACULTY OF THE PRITZKER SCHOOL OF MOLECULAR ENGINEERING
IN CANDIDACY FOR THE DEGREE OF
DOCTOR OF PHILOSOPHY

BY
GREGORY DAVID GRANT

CHICAGO, ILLINOIS
DECEMBER 2024

To my family

"Any sufficiently advanced technology is indistinguishable from magic."

– Arthur C. Clarke

TABLE OF CONTENTS

LIST OF FIGURES

LIST OF TABLES

ACKNOWLEDGMENTS

This work is primarily supported by Q-NEXT, a U.S. Department of Energy Office of Science National Quantum Information Science Research Center under Award Number DE-FOA-0002253. Additional support for cryogenic and optical infrastructure development was provided by the U.S. Department of Energy, Office of Science; Basic Energy Sciences, Materials Sciences, and Engineering Division. Use of the Center for Nanoscale Materials, an Office of Science User Facility, use of the Advanced Photon Source at Argonne National Laboratory, and the EPR work in the Chemical Sciences and Engineering Division were supported by the U.S. Department of Energy, Office of Science, Office of Basic Energy Sciences, under Contract No. DE-AC02-06CH11357. This work also made use of the Jerome B. Cohen X-Ray Diffraction Facility supported by the MRSEC program of the National Science Foundation (DMR-2308691) at the Materials Research Center of Northwestern University and the Soft and Hybrid Nanotechnology Experimental (SHyNE) Resource (NSF ECCS-1542205). Computational work was completed in part with resources provided by the University of Chicago's Research Computing Center.

Regarding personal acknowledgements, I would like to first thank my advisor, Professor Supratik Guha, for being an excellent teacher and sponsor of our group and my research throughout this foray into materials-focused quantum science. I would also like to thank the members of my committee, Professor David Awschalom and Dr. F. Joseph Heremans, who along with Professor Guha have provided peerless leadership and mentorship during this research.

I would further like to acknowledge all of my fellow graduate students, postdocs, staff, and professors with whom I have pursued this work. In particular: Dr. Jiefei Zhang, Dr. Swarnabha Chattaraj, Dr. Kathryn Sautter-Montoya, Dr. Alan Dibos, Dr. Koichi Tanaka, Ignas Masiulionis, Cheng Ji, Connor Horn, Sagar Seth, Claire McDermott, Priyadarshini Mirmira, and Anchita Addhya.

My family, also, has been endlessly supportive and excited regarding my research and pursuit of my PhD. To Mom and Dad, my sister Madeleine, Grandma Sandy, Uncle Dave, Aunt Melissa, and William – thank you all both for for being patient with me as I express the profound stress I've found myself under, and also for being patient with me as I expound excitedly about the crystals I've grown and gotten to shoot lasers at.

Finally, to my dear partner Amanda, thank you for your endless grace and support over the course of these past five years of effort. You have my thanks – and my admiration – for listening and engaging so attentively that you likely could have given my defense presentation if pressed to do so!

ABSTRACT

Optical quantum communication represents a new generation of information technology, with applications from quantum cryptography for secure communication to shared quantum computing resources for solving novel computational problems. However, quantum memory is required to facilitate synchronized operations across long communication channels. Erbium (Er) is an ideal defect for such quantum memory applications: Er emits in the telecom C-band, exhibits spin coherence times in excess of a millisecond in the literature, and can be integrated into a variety of crystalline materials. In this thesis, we initiate development of erbium-doped cerium dioxide (CeO_2) thin films on silicon as a quantum memory platform, finding half-microsecond spin and optical coherence times even in un-optimized CeO_2 thin films. We additionally discuss integration of CeO_2 onto other substrates, and selection of other material hosts based on additional criteria such as Er optical emission rate.

To benchmark Er-doped CeO_2 (Er:CeO_2), we grow thin films of Er:CeO_2 on (111)-oriented silicon by molecular beam epitaxy (MBE) with a range of Er doping levels. Microstructural characterization confirms the structure of the CeO_2 host, while Er spin measurements confirm its embedding into the CeO_2 matrix. Characterization of the Er optical spectrum additionally confirms the remainder of the energy level structure relevant to our work. We establish a baseline for this material in the context of key metrics for rare-earth doped defects systems: as-grown CeO_2 films on silicon with 2-3 ppm Er doping show spin linewidths as narrow as 245(1) MHz, optical inhomogeneous linewidths down to 9.5(2) GHz, and an optical excited state lifetime as long as 3.5(1) ms. To complete our benchmark of Er:CeO2, we find a homogeneous linewidth of 440 kHz for the Y_1-Z_1 optical transition, and Er spin coherence of 0.66 μs in the single-ion limit. These coherence times, currently limited by grown-in defects and high Er doping concentrations, may be increased through optimization of our CeO_2 growth conditions and heterostructure design – but are already sufficiently long to warrant further exploration of MBE-grown Er:CeO_2 as a quantum memory platform.

We additionally explore CeO_2 on (001)-oriented substrates, for increased compatibility with standard nanofabrication platforms such as silicon-on-insulator (SOI). We found that, when grown on Si(001) or (001)-oriented strontium titanate (STO), the inhomogeneous linewidth and spectral diffusion linewidth of Er:CeO_2 are both broader than on Si(111). We also find that the multiple domains of CeO_2(110) that result upon Si(001) substrates do not appear to cause additional inhomogeneous broadening when compared to single-crystal CeO_2(001) on STO(001), corroborating similar results in other materials. We aim to identify a route towards improving optical properties of CeO_2 on Si(001) to match or surpass those found on Si(111), again with an eye towards future integration on (001)-oriented SOI.

Finally, through high-throughput computational methods, we compute oscillator strengths for Er embedded in ∼58,000 materials to identify which hosts result in higher optical relaxation rates. We find that careful host selection could lead to order of magnitude greater Er emission rates compared to current hosts of interest such as CeO_2. Combined with nanophotonics engineering, we speculate that this could push Er-based quantum memory into the 1 GHz bandwidth regime. The next step for this project is to obtain Er-doped samples of promising hosts to experimentally confirm their brightness, and thus verify our host selection process using this technique.

Over the course of this thesis we have taken three major steps in the advancement of quantum communication, taking a defect-first approach towards development of our chosen platform. We have identified a viable quantum communication qubit platform in Er:CeO_2(111) grown on Si(111); we have extended the viability of Er:CeO_2 integration to include Si(001) substrates; and we established computational survey techniques to target additional materials that could provide alternative benefits such as faster optical transitions – all in the development of rare-earth based quantum communication technologies.

CHAPTER 1

INTRODUCTION

1.1 The goal of quantum communication

The field of quantum communication represents a new generation of information technology, with applications from quantum cryptography for secure communications to shared quantum computing resources for solving novel computational problems.[1] Long-distance communication is best performed by using photons as "flying qubits" that may be used to link stationary qubits, per the DiVincenzo criteria.[2] Indeed the most-explored communication modes of using ground-to-satellite communication[3,4] or transmission through optical fibers[5] with photons as the carrier for quantum states.

However, any sort of photonic communication is inherently limited by the optical attenuation of the transmission medium. For example, telecom C-band photons with a wavelength of ~ 1.5 μm are minimally attenuated in telecommunication optical fiber at a rate of ~ 0.2 dB per kilometer, translating to a 1 in 10 chance of a single photon successfully navigating a mere 30 miles of fiber.[6] In classical communication this issue would be mitigated with intermittent amplifiers, but for quantum communication, where the duplication of states is forbidden by the no-cloning theorem,[7] this poor likelihood of transmission is instead mitigated by adding "quantum repeaters". Quantum repeaters act as intermediaries for entangling two ends of a long channel, with transmission lines being divided into short, low-loss segments with repeaters in between.[8,9]

First-generation quantum repeaters will likely use either heralded entanglement generation or heralded entanglement purification procedures for overcoming loss or operator errors, respectively.[10] In both cases, the procedure for entanglement distribution will require (1) interconversion between flying and stationary qubits and (2) storage of quantum states while awaiting operations at other nodes of the network. Quantum memory is therefore funda-

mental to quantum repeater construction per the latter requirement, though it must satisfy both of these in order for quantum communication networks to become a reality.

In this thesis, we focus our interest on the development of quantum memory meant to interface with terrestrial optical fiber networks, with an eye to future development of metropolitan scale quantum networks. Such transmission lines are already in use by telecommunications companies for classical communication, and using existing infrastructure removes a significant barrier to the initial setup and testing of quantum communication protocols. Projects such as the quantum loop testbed between Argonne National Laboratory and the University of Chicago[11] are studying exactly such a pre-existing system, to the benefit of quantum communications research now made directly applicable to real-world solutions.

1.2 Developing quantum memory platforms for quantum communication

The specific implementation of quantum memory platforms for interfacing with terrestrial optical fiber networks, such as the quantum loop testbed, is still an open question. However, for quantum communication applications, there are a set of criteria that guide our implementation choices.

The first criterion is that of the wavelength of photon to be used. We certainly want to use photons as our information carrier, since optical photons are easily delivered over long distance with minimal loss. In particular then, we want 1.5 μm wavelength photons to be our interface, since that is the wavelength at which optical fibers have minimum attenuation.[6] However, this still leaves us with a large number of possible quantum memory systems to choose from.[12,13]

Our second criterion is implied by the concept of metropolitan-scale light-based communication: a storage qubit in such a network must have a long coherence time, such that information can be held for the duration required for light to travel between nodes – for ex-

ample, to await synchronized swap operations.[9] For example, Chicago to Detroit is a ~ 400 kilometer journey, in excess of a light-millisecond. As such, a quantum memory for optical fibers connecting metropolitan distances with a quantum communication network require coherence times in excess of a millisecond.

The third criterion is that we want our quantum memory qubit to be integrated into a solid-state system. This is primarily so that our quantum memory platform may eventually be integrated with semiconductor devices for on-chip memory control, photon detection, and multiplexing operations – all necessary for participating in a robust, complex quantum networking operation.

Putting these three criteria together, we identify erbium as an ideal qubit defect for quantum communication-focused quantum memory applications. Erbium emits at 1.5 μm,[14] is demonstrated in the literature to have coherence times in excess of a millisecond in its spin transition,[15,16,17] and can be integrated into a large variety of crystalline materials via a multitude of methods.[18,19] As a valuable side effect of selecting erbium, working with a rare-earth ion such as erbium allows us to leverage the past several decades of spectroscopic study of rare-earths for lasing and other applications – work that may now be brought to bear on the grand scientific challenge of quantum communication.

1.3 Motivation for erbium-doped oxide thin films

Having selected erbium (Er) as our quantum memory defect of choice, we then must identify the host into which erbium shall be placed. The intrinsic spin-photon interface and long coherence times of erbium[14] have inspired an array of studies for Er integration into solid-state hosts – including systems such as Er:TiO_2,[20,21,22] Er:Y_2O_3,[23,24] Er:$CaWO_4$,[16,25] Er:Y_2SiO_5,[15] Er:MgO,[26] Er:YVO_4,[27] Er:$LiNbO_3$,[28] and Er:Si[29,30] in order to explore desirable characteristics of the various hosts, and how those characteristics interplay with the suitability of Er as a memory defect.

To select an optimal host for quantum communication purposes, we recall our second criterion from the previous section – we are interested in maximizing the coherence time of our quantum memory defect. We anticipate the use of the erbium electron spin as our storage state, and so optimizing the electron spin coherence of the trivalent Er ion (Er^{3+}) for quantum memory applications necessitates selection of an environment with minimal decoherence sources. A recent computational study identified that cerium dioxide (CeO_2) is an optimal host for maximizing electron spin coherence,[31] due to the near-zero natural abundance of nuclear spins in its constituent elements.[32] Indeed, oxide hosts in general represent a class of materials well-suited for enabling long coherence times.[31]

We also must consider the form taken by our solid state host. While bulk oxide crystals present largely defect-free environments, Er-doped thin film hosts, including wide band-gap oxides grown on silicon, have begun to be demonstrated as a promising quantum memory platform due to their compatibility with established semiconductor platforms[23,21] and the potential for scalable on-chip integration.[33,34,22]

With thin films on silicon as a viable avenue towards chip-scale integration, CeO_2 is additionally attractive as a host for Er^{3+} due to having a lattice constant (5.41 Å) close to that of Si (5.43 Å).[35]

Thus we have converged upon a quantum memory platform to develop: trivalent erbium (Er^{3+}) doped into cerium dioxide (CeO_2) thin films integrated atop silicon substrates.

1.4 Scope of this thesis

This thesis is divided into three main parts.

This introduction plus Chapters 2 through 5 comprise the first part, and include the background necessary to understand the theoretical and experimental methods used in developing rare-earth doped oxide quantum memory platforms. The second part of this thesis is contained in Chapter 6, and follows the benchmarking of Er-doped CeO_2 as a candidate for

rare-earth doped oxide quantum memory. The third part of this thesis develops across Chapters 7 and 8, and explores new directions for developing rare-earth doped thin film platforms for scalability and improved optical properties for quantum communication applications.

In addition to goals implicit in the aforementioned structure, I have been tasked with writing this thesis in part as an introduction to quantum memory defect development for graduate students new to the field. This leads to the extended nature of the first part of the thesis and the emphasis on understanding the structure of rare-earths within crystalline hosts. My hope also is, though I present these studies primarily from the perspective of erbium-doped oxide, that the general approach found in this thesis should be appropriate to other systems as well.

Finally, this thesis will not discuss any manner of nanofabrication, but rather all of the steps leading up to that point in terms of preparing the defect-host system. The goal of this thesis is specifically to navigate the maximization of defect quality (and subsequently those defects' hosts), such that subsequent engineering of the platform into devices is in turn maximally viable.

CHAPTER 2

ENERGY STRUCTURE OF ER-DOPED OXIDE SYSTEMS

2.1 Describing the rare-earth ion

To effectively discuss the development of the erbium-doped oxide platform, we must first understand how the energy structure of the rare-earths comes about. Our focus is on the 1.5 μm optical transition of erbium and its electron spin transition for flying/stationary interconversion[6,2] and coherent state storage[16] respectively, but knowing how these states arise and are linked is vital to implementing any sort of quantum memory protocol.

The rare-earths are split into the lanthanides (the elements with atomic numbers between lanthanum and lutetium) and the actinides (the elements with atomic numbers between actinium and lawrencium). The actinides are largely not as useful for quantum memory purposes, given their propensity towards being radioactive and/or hard to synthesize.

As such we will focus on the lanthanides – of which erbium is a member – for our analysis of rare-earth structure. Lanthanides are atoms that consist of a xenon core with electron configuration $1s^2 2s^2 2p^6 3s^2 3p^6 3d^{10} 4s^2 4p^6 4d^{10} 5s^2 5p^6$, plus a set of electrons in the $4f$, $5d$, and $6s$ shells.[36] The triply oxidizied state (also called the trivalent state, or signified by M^{3+} for an element M) is most stable for rare-earths (though in the specific cases of cerium and terbium, Ce^{4+} and Tb^{4+} are similarly stable). In the trivalent state, the valence shell is always $4f$, with the number of electrons in the $4f$ shell ranging from 1 for Ce^{3+} in the $4f^1$ configuration, to 14 for Lu^{3+} in the $4f^{14}$ configuration.

One particularly poignant aspect of the rare-earths is the so-called "lanthanide contraction," where the majority of the $4f$ electron wavefunction rests inside the extent of the $5s$ and $5p$ electron wavefunctions that are part of the xenon core, with greater contraction of the $4f$ electron towards the nucleus with increasing atomic number of the rare-earth.[36] Because of this we refer to the $4f$ electrons of rare-earths as being "shielded," a shorthand descrip-

tion for how the $4f$ electrons of rare-earths do not strongly participate in ligand bonding and so are only slightly perturbed by ligand environment.[14] The shielded nature of the $4f$ electrons is not immediately obvious as we explore the energy structure of the rare-earths, but it is important to note prior to the discussion as context for, e.g., the relatively small perturbation of the crystal field upon the rare-earth levels as explored in Section 2.1.2.

Descriptions of the rare-earth ions often rely on the closed-shell approximation, wherein the electrons in shells below $4f$ are treated as not interacting with the $4f$ electrons. Under this assumption, we may treat a rare-earth as an N-electron atom, where N is simply the number of electrons in the $4f$ shell. In this chapter, we begin with the Hamiltonian expression of such an N-electron atom, and then go through the perturbations that generate the familiar rare-earth energy structure we wish to use for quantum memory. We also address the influence of external fields, and how the energy structure of erbium in particular may be truncated for practical purposes of evaluating experimental work.

2.1.1 A basic N-electron atom

We begin our analysis of the rare-earth energy structure by stating the Hamiltonian for an N-electron atom with a nuclear charge Ze.[37]

$$H = -\frac{\hbar^2}{2m}\sum_{i=1}^{N}\nabla_i^2 - \sum_{i=1}^{N}\frac{Ze^2}{r_i} + \sum_{i<j}^{N}\frac{e^2}{r_{ij}} \tag{2.1}$$

Schrödinger's equation is not solvable for more than one electron, so we use the "central field" approximation, assuming that each electron moves independently in the field of the nucleus and surrounding electrons. We describe the electron "cloud" as generating an additional potential field caused by the spherically averaged potentials of the other electrons. The combined spherically symmetric potential on a single electron at a position r_i is called $U(r_i)$, and becomes a component of the central field Hamiltonian H_{CF}. The remaining inter-electron interactions become the Coulombic perturbation terms labelled H_c.

$$H = H_{\mathrm{CF}} + H_c, \quad H_{\mathrm{CF}} = \sum_{i=1}^{N} \Big(-\frac{\hbar^2}{2m}\nabla_i^2 + U(r_i) \Big) \tag{2.2}$$

The central field part of the Hamiltonian is analagous to the hydrogenic Hamiltonian, and so provides the following normalized wavefunctions ψ for an electron at coordinates (r, θ, ϕ) and with the hydrogenic quantum numbers (n, l, m), where the wavefunction is split into the radial part $R_{nl}(r)$ and the spherical harmonic part $Y_{lm}(\theta, \phi)$:

$$\psi(r, \theta, \phi, n, l, m) = \frac{1}{r} R_{nl}(r) Y_{lm}(\theta, \phi) \tag{2.3}$$

The spherical harmonics are well defined by the Legendre polynomial solutions to Laplace's equation in spherical coordinates. The radial part of the wavefunction depends on the central potential $U(r)$ and the electronic interactions within a particular species of ion.

Thus having a single-electron wavefunction, we obtain the wavefunction for all electrons in the atom by using the determinantal product state obtained by taking the Slater determinant across all the electrons in the atom for all the configurations populated by those electrons. This defines the basic N-electron atom, the starting point for our rare-earth Hamiltonian evaluation.

Once the N-electron atom is established, we then look at the Coulombic correction H_c of the Hamiltonian from Equation 2.2.

$$H_c = \sum_{i=1}^{N} \Big(-\frac{Ze^2}{r_i} - U(r_i) \Big) + \sum_{i>j=1}^{N} \frac{e^2}{r_{ij}} \tag{2.4}$$

The second term becomes the first correction to the central field Hamiltonian that actually requires evaluation. We shall call it the Coulombic interaction H_1, and it depends on the distance between pairs of electrons r_{ij}.

$$H_1 = \sum_{i>j=1}^{N} \frac{e^2}{r_{ij}} \tag{2.5}$$

The first summation in the central field Hamiltonian only shifts the entirety of a configuration, and all of our work will study a single configuration: so, we drop it from consideration.[37] However, electrons are still certainly subject to the central field potential, which imposes a second correction: the spin-orbit perturbation H_2, which takes the following form where we have the individual electron spin angular momentum $\boldsymbol{s}$, the individual electron orbital angular momentum $\boldsymbol{l}$, the reduced Planck constant $\hbar$, the electron mass m, and the speed of light c:

$$H_2 = \sum_{i=1}^{N} \xi(r_i) \boldsymbol{s}_i \cdot \boldsymbol{l}_i, \qquad \xi(r) = \frac{\hbar^2}{2m^2c^2r} \frac{\mathrm{d}U}{\mathrm{d}r} \tag{2.6}$$

Our total Hamiltonian, including our corrections for the electronic configuration energies, then becomes:

$$H = H_{\mathrm{CF}} + H_1 + H_2 \tag{2.7}$$

To evaluate the Hamiltonian once corrected by H_1 and H_2, we define the total orbital momentum $\boldsymbol{L}$ and total angular spin momentum $\boldsymbol{S}$:

$$\boldsymbol{L} = \sum_i \boldsymbol{l}_i \qquad \boldsymbol{S} = \sum_i \boldsymbol{s_i} \tag{2.8}$$

These total momenta then set their respective quantum numbers L and S, which have multiplicities of $(2L+1)$ and $(2S+1)$ respectively. We define a single combination of L and S as a "term" denoted by the notation ${}^{2S+1}L$, where L is represented in spectroscopic notation.†

†. Spectroscopic notation: $0 = S$, $1 = P$, $2 = D$, etc.

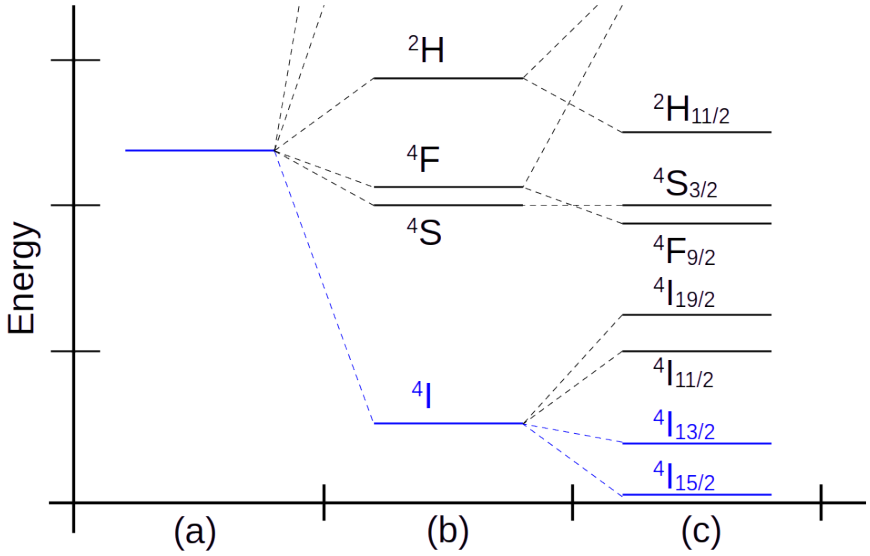

Figure 2.1: Schematic (not to scale) term and level splitting for the lowest few Er^{3+} states. Blue lines and labels correspond to the path from the unperturbed structure to our transition of interest. Column (a) represents the fully degenerate configuration energy, which is then split by H_1 to produce the terms in column (b). Column (c) then is the fully-split levels once H_2 is accounted for. The transition between $^4I_{15/3}$ and $^4I_{13/3}$ is then the 1.5 μm transition of interest, and remains at approximately 1.5 μm separation regardless of subsequent perturbations to the erbium Hamiltonian.

The H_1 term in the Hamiltonian corrections splits the terms with different numbers to become non-degenerate. In the case of erbium, the ground state is within the term ^4I, or rather where the spin has multiplicity $2S + 1 = 4$ and $L = 6$.

The H_2 term in the Hamiltonian corrections splits the degenerate states within each term according to the total angular momenta $\boldsymbol{J} = \boldsymbol{S} + \boldsymbol{L}$. In the multi-electron context, this summation is referred to as LS-coupling, or "Russel-Saunders" coupling, and is one of several available coupling schemes – in our case, it is the most intuitive for an experimentally-oriented discussion. The states in each term are split according to the corresponding quantum number J, which also establishes the z-quantized total angular momentum J_z. The end result is $2J+1$ degenerate "levels" denoted by the notation $^{2S+1}L_J$, which now completed we refer to as "term symbol". The splitting into the $^{2S+1}L_J$ levels as H_1 and H_2 are applied may be seen in Figure 2.1.

It is the level splitting that produces the 1.5 μm transition that we are interested in using as an optical interface for our Er^{3+} defects. Specifically, the $^4I_{15/3}$ level ($S = 3/2$, $L = 6$, $J = 15/2$) is the ground state, and the $^4I_{13/3}$ level ($S = 3/2$, $L = 6$, $J = 13/2$) is the first excited state, separated from the ground state by approximately 6500 cm^{-1}.[14†] Subsequent perturbations to the rare-earth will not deviate significantly from this value, due to the degree of 4f shielded-ness present for this late-in-the-series lanthanide.

Speaking of subsequent perturbations, we recall that these levels are still $(2J + 1)$-fold degenerate, but this degeneracy will be partially to fully lifted by the crystal field potential and external fields, as discussed in the following sections.

2.1.2 The crystal field potential

The third corrective term in the rare-earth Hamiltonian is that of the electric potential caused by the ions that make up the crystal surrounding our rare-earth ion of interest. In this situation, we assume that the electrons of our rare-earth ion are well-localized (reasonable given the contraction of the 4f shell) and that the remainder of the crystal lattice is spectroscopically inert (also reasonable, for wide bandgap materials such as the oxides selected for this project).[36]

The contribution to the rare-earth Hamiltonian may be labelled H_3, and is expressed as follows, where an electron i at position (r_i, θ_i, ϕ_i) is perturbed by the electric potential V_e produced by the crystal environment:

$$H_3 = -e \sum_i V_e(r_i, \theta_i, \phi_i) \tag{2.9}$$

In working with Er^{3+}, the crystal field potential may be expanded for a single unpaired electron within our ion of interest with coordinates (r, θ, ϕ).[37]

†. In various units for an optical photon: 6500 $cm^{-1} \sim 806$ meV ~ 195 THz ~ 1.54 μm

$$H_3 = \sum_{k,q} A_q^{(k)} r^k C_q^{(k)}(\theta, \phi) \tag{2.10}$$

Here we have the spherical harmonic operators $C_q^{(k)}$, with component q of rank k, where $k \in \mathbb{Z}_{\geq 0}$ and $q \in= [-k, -k+1, ..., k-1, k]$. In standard spherical harmonic notation Y_l^m, note l is the rank and m is the component. It is convenient to use these spherical harmonic operators, which are defined in terms of the spherical harmonics:

$$C_q^{(k)}(\theta, \phi) = \sqrt{\frac{4\pi}{2k+1}} Y_l^m(\theta, \phi) \tag{2.11}$$

A convenient spherical harmonic expansion for the electric potential V_e is that of a field of point charges Q_i at coordinates (R_i, Θ_i, Φ_i), as provided by Hutchings[38] for the case where the electron radial coordinate r fulfills $r < R_i \ \forall i$ – again, a reasonable approximation given the 4f contraction. Approximating all nearby ions as point charges is somewhat more egregious here, but remains a reasonable approximation for purposes of looking at site symmetries and trends in H_3 matrix elements.

$$V_e = \sum_{k,q} r^k \gamma_{kq} Y_k^q(\theta, \phi), \quad \gamma_{kq} = \sum_i \frac{4\pi}{2k+1} \frac{Q_i}{R_i^{k+1}} (-1)^q Y_k^{-q}(\Theta_i, \Phi_i) \tag{2.12}$$

We may easily recast this in terms of the spherical harmonic operators, and we may additionally turn the electric potential V_e into the perturbation H_3 by multiplying by the charge of the evaluated electron of interest Q_e. For simplicity we place the ion charge within the evaluation of $\gamma_k q$.

$$H_3 = \sum_{k,q} r^k \gamma_{kq} C_q^{(k)}(\theta, \phi), \quad \gamma_{kq} = \sum_i \frac{Q_e Q_i}{R_i^{k+1}} (-1)^q C_{-q}^{(k)}(\Theta_i, \Phi_i) \tag{2.13}$$

The definitions from Judd and Hutchings may be set equal to each other to recover the $A_q^{(k)}$ coefficients in terms of γ_{kq}. To find the coefficients, we may match terms in both sums

Er^{3+} *Level*	$^4I_{15/2}$	$^4I_{13/2}$	$^4I_{11/2}$	$^4I_{9/2}$
Num. Levels in Cubic Site Symmetry	5	5	4	3
Num. Levels in Non-Cubic Site Symmetry	8	7	6	5

Table 2.1: Number of crystal field levels encountered for different levels in Er^{3+}, per Wybourne 1965.[36]

using the spherical harmonic operators multiplied by r^k as a basis. We find that the $A_q^{(k)}$ and γ_{kq} are in fact the same parameter.

$$V = \sum_{k,q} A_q^{(k)} r^k C_q^{(k)}(\theta, \phi) = \sum_{k,q} r^k \gamma_{kq} C_q^{(k)}(\theta, \phi) \quad \Rightarrow \quad A_q^{(k)} = \gamma_{kq} \tag{2.14}$$

Thus we have a definition we may use in Judd's formalism. We also make the transformation into SI units and prepend the appropriate constants to the potential energy, and then promptly absorb those also into the definition of the expansion coefficients.

$$H_3 = \sum_{k,q} A_q^{(k)} r^k C_q^{(k)}(\theta, \phi), \quad A_q^{(k)} = \frac{1}{4\pi\epsilon_0} \sum_i \frac{Q_e Q_i}{R_i^{k+1}} (-1)^q C_{-q}^{(k)}(\Theta_i, \Phi_i) \tag{2.15}$$

As a practical consideration, the sum over charges to describe $A_q^{(k)}$ should include "all of the complete cells in a sphere of 30 Å radius"[39] when performing finite computational summations over the surrounding field of ions. This will become relevant in Chapter 8.

Per the previous section, the Er^{3+} levels hold $(2J + 1)$ degenerate states, based on the total angular momentum J. The crystal field environment splits these degenerate states. In the case of Er^{3+}, in the $^4I_{15/2}$ term there are up to 8 degenerate doublets (referred to as Kramers' doublets, defined as un-split electron spin states for one unpaired electron) for a total of 16 degenerate states, and in the $^4I_{13/2}$ there are up to 7 degenerate Kramers' doublets for a total of 14 degenerate states. The only exception to obtaining 8 and 7 doublets respectively is the case of a cubic crystal field site symmetry, where some doublets are not

fully split and there are instead 5 and 5 levels, per Table 2.1, with the corresponding increase in degeneracy.

The crystal field-split doublets are referred to as the "crystal field levels," and the energy separation between the crystal field levels depends on the strength of H_3 – and correspondingly the orientations and distances of the crystal field charges from the Er^{3+} site. Separation between crystal field levels is usually on the order of 1 to 5 meV, or 100 GHz to 2 THz splitting.[14] This makes the crystal field levels difficult to probe directly given the complexities of terahertz spectroscopy,[40] but we are able to probe the crystal field levels indirectly via photoluminescence measurements between the ${}^4I_{15/2}$ and ${}^4I_{13/2}$ terms as discussed in Chapter 6.

2.1.3 Other perturbations to the rare-earth ion

Beyond the first three perturbations, there are five more perturbations that come into play when evaluating Er^{3+} structure.[37] We discuss here the first three of those remaining perturbations, as they readily arise when studying the spin behavior of the Er^{3+} ion, and we present the latter two perturbations only as an initial point of reference for the interested reader.

The first of these additional perturbations is the effect of an external magnetic field, represented by H_4 for a magnetic field $\boldsymbol{H}$, the Bohr magneton β, and the gyromagnetic ratio of the elctron g_s.[36] This perturbation gives rise to the Zeeman effect for moderate magnetic field strengths.

$$H_4 = \beta \boldsymbol{H} \cdot (\boldsymbol{L} + g_s \boldsymbol{S}) \tag{2.16}$$

As a companion to the Zeeman term, the magnetic hyperfine interaction H_5 gives rise to hyperfine splitting of the Zeeman lines in the presence of a nuclear spin, which is $I = 7/2$ for ${}^{167}Er$ and $I = 0$ for any other Er isotopes. We now also invoke the nuclear magneton β_N

and the nuclear magnetic moment μ_N.

$$H_5 = \frac{2\beta\beta_N\mu_N}{I}\sum_i \frac{\boldsymbol{N}_i \cdot \boldsymbol{I}}{r_i^3},\ \boldsymbol{N}_i = \boldsymbol{l}_i - \boldsymbol{s}_i + \frac{3\boldsymbol{r_i}(\boldsymbol{r_i}\cdot\boldsymbol{s_i})}{r_i^2} \tag{2.17}$$

Evaluation of H_4 and H_5 is decidedly nontrivial, but fortunately the the combined terms may be represented by an approximate effective spin-S Hamiltonian H_{4-5} under the assumptions that all the states being evaluated are within the same J manifold, and that the primary contributor to splitting in H_4 is the electron spin. Thus we may write the following, where we have introduced the parameters $\boldsymbol{g}$ (the effective g-factor tensor) and A (the hyperfine splitting coefficient).

$$H_{4-5} = \beta\boldsymbol{B}\cdot\boldsymbol{g}\cdot\boldsymbol{S} + A\boldsymbol{S}\cdot\boldsymbol{I} \tag{2.18}$$

In the context of the lowest Er^{3+} crystal field level in both ${}^4I_{15/2}$ and ${}^4I_{13/2}$, this may be treated as an electron spin-1/2 system interacting with the nuclear spin-I system. Thus we may evaluate the shared spin states of the electron and nucleus when performing spin resonance measurements, as in Section 5.2.

Also in the context of spin resonance measurements, the last perturbation that we leverage in our measurements is the magnetic spin-spin interaction, H_6:

$$H_6 = 4\beta^2\sum_{i>j}\Big(\frac{\boldsymbol{s}_i\cdot\boldsymbol{s}_j}{r_{ij}^3} - \frac{3(\boldsymbol{r}_ij\cdot\boldsymbol{s}_i)(\boldsymbol{r}_ij\cdot\boldsymbol{s}_j)}{r_{ij}^5}\Big) \tag{2.19}$$

While this term does not dramatically affect multiplet splitting and does not modify the crystal field level structure significantly for a single Er^{3+} ion, this term does contribute inhomogeneous shifts across an ensemble of Er^{3+} ions plus other defects present within the crystal, contributing broadening to measured resonance lines. This term is explored in greater detail in Chapter 6 and Appendix B in the ensemble context.

The two remaining perturbations we will describe here are the nuclear quadrupole inter-

action H_7 and the spin-other-orbit interaction H_8.[37] H_7 includes the the electron charge e, along with values Q (which is defined according to matrix elements in the I and M_I quantum numbers) and $\boldsymbol{K}^{(2)}$ (which is a rank-2 tensor with components in the nuclear spin I). H_8 additionally invokes the reduced Planck constant $\hbar$, mass of the electron m, the speed of light c, the distance between two electrons r_{ij}, and the momentum of one electron $\boldsymbol{p}_i$.

$$H_7 = -\frac{e^2 Q}{I(2I-1)} \sum_i r_i^{-3} (\boldsymbol{C}_i^{(2)} \cdot \boldsymbol{K}_i^{(2)}) \tag{2.20}$$

$$H_8 = \frac{e^2 \hbar^2 \Xi}{2m^2 c^2}, \qquad \Xi = \sum_{i \neq j} \left(\nabla_i (r_{ij}^{-1}) \times \boldsymbol{p}_i \right) \cdot (\boldsymbol{s}_i + 2\boldsymbol{s}_j) \tag{2.21}$$

These terms do not produce significant deviation from the level structure explored in Sections 2.1.1 and 2.1.2 (indeed, part of the interaction in Ξ of H_8 is already accounted for in H_2 spin-orbit perturbation[41]), nor do they contribute additional splittings due to external fields or significant broadening that arises in our optical and spin resonance measurements. However, they are important to note for furture reference should explanations of observed Er phenomena based only on H_1 through H_6 fail.

2.2 A practical perspective on Er energy structure

In practice, when evaluating experimental work with Er^{3+} for quantum communication applications, we greatly reduce the complexity of the effective system from the eight Hamiltonian terms addressed in the previous sections.

The first approximation to arise out of practicality is that we take the central field Hamiltonian H_{CF}, the Coulombic interaction H_1, and the spin-orbit interaction H_2 as constant and pre-determined. These three expressions are rarely of interest in our experimental exploration other than to give rise to the ${}^4I_{15/2}$ and ${}^4I_{13/2}$ levels and to provide a basis in which to work. We additionally truncate the level structure to only include ${}^4I_{15/2}$ and ${}^4I_{13/2}$ levels,

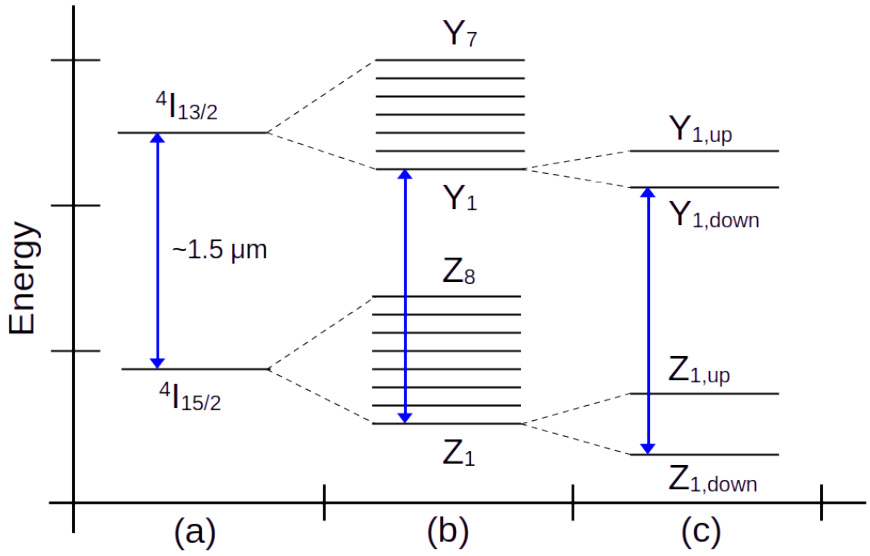

Figure 2.2: Schematic (not to scale) crystal field level and electron Zeeman splitting for the lowest few Er^{3+} levels. Blue arrows correspond to the ~ 1.5 μm optical transition and is shown between the lowest $^4I_{15/2}$ to lowest $^4I_{13/2}$ state, for visual reference. Column (a) shows the level structure developed in Figure 2.1(c), truncated to the two lowest Er^{3+} levels. Column (b) shows the application of the crystal field splitting per H_3, and the Z_i and Y_i levels produced (with maximum lifting of degeneracy to 8 and 7 levels respectively). Column (c) finally shows the splitting of the Z_1 and Y_1 crystal field levels into effective spin-up and spin-down states via Zeeman splitting.

---

as at liquid helium temperatures (~ 4 K) and lower there will be very near zero population of the $^4I_{11/2}$ level or higher; we also do not typically perform optical measurements to probe that high in energy.

Having reduced the number of levels to consider, we then apply the crystal field splitting via H_3 to obtain eight $^4I_{15/2}$ levels and seven $^4I_{13/2}$ levels when full splitting is induced. The eight $^4I_{15/2}$ levels are colloquially referred to as the Z levels, while the seven $^4I_{15/2}$ levels are referred to as the Y levels. The levels are indexed from lowest energy to highest, from Z_1 to Z_8 and from Y_1 to Y_7. When only five crystal field levels are identified due to cubic symmetry, the crystal field levels instead run from Z_1 to Z_5 and Y_1 to Y_5.

We then collectively apply the electron spin and hyperfine terms H_4 and H_5 as the effective H_{4-5} shown in Equation 2.18. Spin resonance experiments generally occur in Z_1,

where the system is effectively spin-1/2. Optical measurements of the spin dynamics also use the Zeeman-split Y_1 level, which is also effectively spin-1/2, albeit with a different effective g-factor than in Z_1.

This is then the extent of the level structure discussed while performing experimental work when needing to index the available Er^{3+} levels. A diagram of this may be seen in Figure 6.5. The additional Hamiltonian terms H_6 to H_8 are neglected when discussing level structure, and are only used in analysis where necessary to describe additional effects such as ensemble broadening.

CHAPTER 3

EXPERIMENTAL METHODS FOR ER-DOPED OXIDE THIN FILM GROWTH

3.1 Selecting a growth method

In the pursuit of developing thin film oxide hosts, an initial concern is the concentration of impurities that may be present in a grown thin film sample. Our rare-earth dopants must be well-isolated from any other dopants (referred to as the "dilute doping" limit), but also from any impurities that may interact with the electron spin or orbital states and consequently induce dephasing the spin or optical transitions.[14] Our second concern in growing pristine thin films is that a fine degree of control over the morphology of the thin film microstructure is preferred. Per Section 2.1.2, variations in the crystal field surrounding our rare-earth dopants have non-trivial impacts on the resulting energy structure.

Thin film growth methods are usually split into two categories: chemical deposition techniques, and physical deposition techniques.[42†] Chemical deposition generally consists of the flowing of chemical precursors over a sample surface, either together or in sequence, to react and produce the desired composition of thin film. Examples of chemical deposition include atomic layer deposition (ALD), chemical vapor deposition (CVD), and metalorganic growth methods. Physical deposition instead generally consists of delivering the exact chemical composition to the sample surface directly, with no reaction byproducts. Examples of physical deposition include sputtering, e-beam evaporation, and molecular beam epitaxy (MBE).

The preeminent technique for developing new thin film oxide hosts for rare-earth defects for quantum communication purposes is MBE. As will be discussed in the upcoming Section 3.2, the mechanics and environment of MBE readily satisfy the conditions of impurity

†. It is worth noting that there are methods that blur this binary, such as reactive sputtering and metal-organic MBE, but the distinction remains useful as a point of discussion.

control, microstructural control, and dopant control.

Before that though, to briefly clarify the downsides of other methods: ALD is a mature technique but can be difficult for use in developing new materials. The main drawback of the technique is that ALD generally produces amorphous, disordered films that require post-processing to use as rare-earth hosts as a consequence of low process temperatures, usually below 300 ℃. These low temperatures are required for the "ALD temperature window," above which the ALD technique inadvertently becomes CVD-like.[43] CVD in turn is limited by the complexity of the required precursors, the chemistry of which requires careful selection and testing when developing new materials.[44] Additionally, CVD methods run the risk of incorporating reaction byproducts into the host, which could have unwanted effects on behavior of the rare-earth dopants. ALD and standard CVD processes traditionally take place at elevated pressures between 0.1 and 1 torr, which may also lead to impurity incorporation into the thin film. Sputtering bypasses the issue of reaction byproducts, but the high-energy particles required for sputtering may lead to defect formation within the thin film, or unintentional sputtering of growth chamber elements leading to impurities within the thin film.[45] MBE bypasses the majority of these issues, and so is an optimal technique for developing new, high-quality thin film materials.

In the following sections, we discuss the growth conditions made available by the MBE technique, the *in-situ* characterization methods used to track growth, and the straightforward methods used for developing growths of new materials.

3.2 Overview of the molecular beam epitaxy (MBE) growth environment

The core tenant of MBE as a deposition method is that the only species present in the growth environment are those being flowed towards the substrate upon which growth is occurring. In an ideal setting, a perfect ratio of fluxes would impinge upon an atomically clean substrate

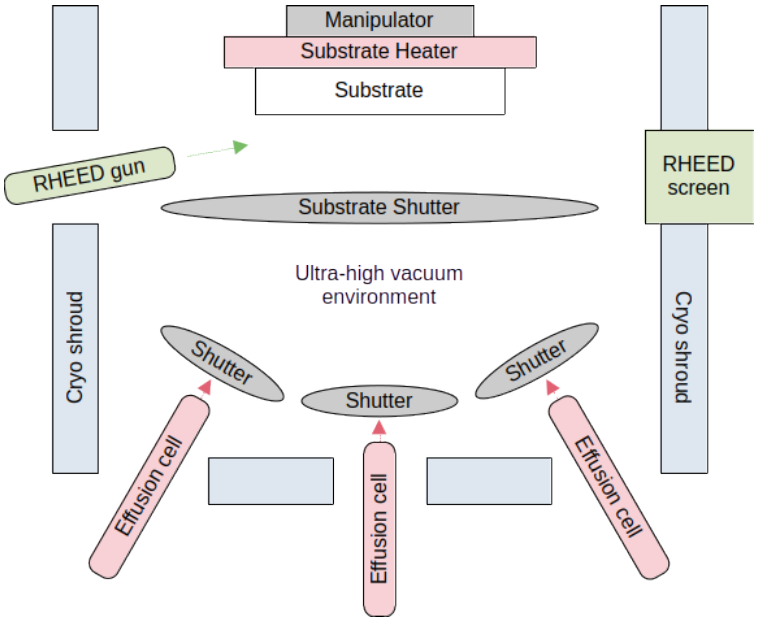

(a) Schematic of standard components in an MBE growth chamber

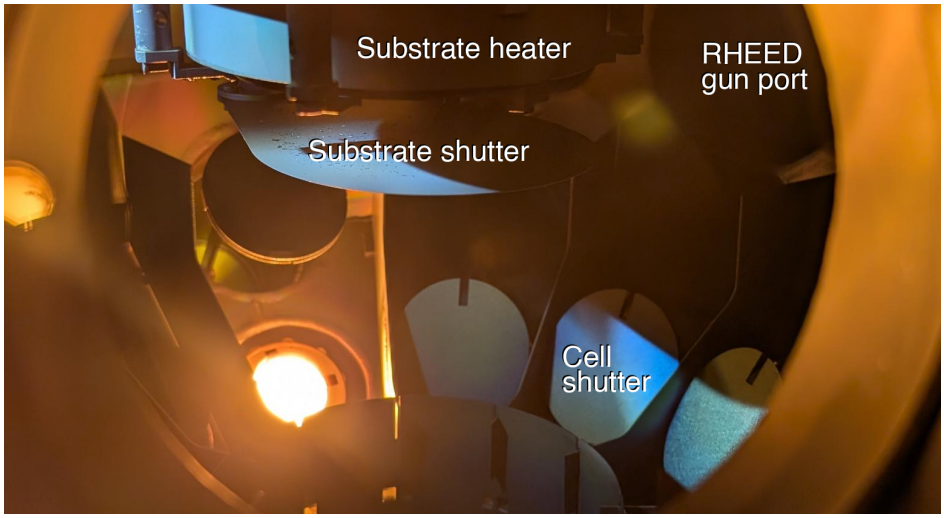

(b) Interior of an MBE growth chamber. One effusion cell is hot with its shutter open; the rest are closed. The substrate rests below the substrate heater, and is shielded from the open cell by its own shutter.

Figure 3.1: Within an MBE growth chamber, an array of molecular beam sources – including effusion cells and gaseous mass flow sources – are pointed towards a heated substrate. The sources and substrate each have a shutter for growth control. A RHEED gun and screen provide *in-situ* characterization of the growth surface. A cryo shroud assists in keeping the pressure of the chamber low.

to form the desired material, with no impurities present within the chamber or upon the substrate. We additionally would like the substrate to have the ideal conditions to permit crystalline growth, e.g., substrate surface conditions and growth temperature.

While obtaining a perfectly clean environment is near impossible, we can get quite close by bringing our growth chamber to ultra-high vacuum (UHV) conditions before starting growth, and then by introducing only pure sources of material during growth. UHV is defined as pressures at or lower than 10^{-8} torr – this is the criteria that the growth chamber base pressure (base pressure here defined as the pressure immediately prior to introducing material to the chamber for growth) must meet at minimum. MBE is traditionally performed with base chamber pressures of 10^{-10} to 10^{-11} torr for semiconductor applications, though in the context of an oxide growth chamber we are less concerned about oxygen and water contaminants within the growth chamber, and so base pressures for oxide MBEs like ours may be as high as 10^{-9} torr.

At such low pressures at 10^{-9} torr, the mean free path of a particle within the chamber is on the order of 100 kilometers.[46] Rather, a particle that has left a source of material will very likely only collide with either the growth surface or with the growth chamber wall. Additionally, at 10^{-9} torr, the rate of gaseous impingement from the environment upon the growth surface is on the order of 10^{-3} monolayers per second, which is small compared to nominal MBE growth rates of up to 1 monolayer per second and leads to low impurity accumulation due to the growth environment.[46] Compare this to ALD and CVD, where the pressure is 0.1 to 1 torr: there the gaseous impingement rate is as high as 10^{5} monolayers per second, which has the potential to lead to significant sample contamination if the chamber is improperly managed. Rather, the UHV environment enforced by MBE guarantees growths that are low in impurities caused by the chamber environment.

To obtain this UHV environment for our oxide MBE chamber, a set of four pumps are used. First is a turbomolecular pump, or 'turbopump,' which brings the chamber down

to 10^{-6} to 10^{-8} torr via a set of high-speed rotors. The turbopump is backed by a rotary roughing pump, which provides pressures of 10^{-1} to 10^{-3} torr to the turbopump exhaust, and allows the turbopump to run continuously without excess wear. To achieve sufficiently low base pressures within the growth chamber, the turbopump is supplemented by a cryogenic pump, or 'cryopump,' which contains 15 K cold plates that capture species such as nitrogen, oxygen, water, and some organics. Finally, the chamber contains a titanium sublimation pump, or 'TSP,' which sublimates titanium upon the growth chamber walls. The sublimated titanium then getters residual oxygen, water, and organics from the chamber environment. The resulting base pressure in our chamber is then approximately 5×10^{-9} torr.

To achieve 1×10^{-9} torr base pressures, the growth chamber is lined with a set of cryopanels (see Figure 3.1(a)) through which liquid nitrogen flows. The liquid nitrogen flow cools the cryopanels, which then capture gaseous species (and errant source material) from the growth chamber in the same manner as the cryopump. Upon turning on the liquid nitrogen flow before growth, base pressures drop to the desired 1×10^{-9} torr. After growth is complete, the liquid nitrogen flow is turned off to desorb collected material from the chamber walls and allow for more efficient pumping for subsequent growths. The cryopanels have the added benefit of increasing the overall pumping rate of the chamber, allowing for greater fidelity in managing oxygen partial pressure when flowing high pressures of oxygen for growth.

Once at low pressure, we supply metallic source materials from effusion cells (also called Knudsen cells) for thermal evaporation or sublimation – see Figure 3.1 for how cells are mounted in the chamber. To do so, we load high-purity metal (ideally at least 5N purity, corresponding to 10 parts per million impurities) charges into crucibles made from low vapor pressure materials (often tungsten, tantalum, or pyrolytic boron nitride). The crucibles are then heated using resistive filaments near the crucible, and the heat drives sublimation or

evaporation of the source material charge.† To provide gaseous elements such as oxygen, a mass flow controller is connected to a small aperture in the growth chamber, and high-purity gas is added to the chamber at a fixed flow to obtain a fixed partial pressure.

Each material source, whether an effusion cell or gas source aperture, is gated by a shutter that controls whether that source's material flows towards the substrate. A closed shutter blocks material, and an open shutter permits material. To provide atomically sharp control over the growth as a whole, an additional shutter is placed between the substrate and the entire collection of sources.

The last step in setting up the MBE environment is control of the substrate. The substrate upon which growth occurs is mounted in proximity to a heater, called the substrate heater, that can bring the substrate to temperatures as high as 900 ℃ during growth – with higher temperatures often being required for films to grow epitaxially (that is to say, single-crystalline and with well-defined orientation with respect to the underlying substrates). The substrate mount also allows for rotation of the sample, to increase uniformity over the span of the substrate during growth.[46]

With the growth environment suitably defined, we now turn our attention to the characterization of our thin films during growth.

3.3 *In-situ* characterization during MBE growth

Given that MBE growth is a fairly complex process, it is incredibly helpful to monitor any growth as it progresses. There are two main tools that can be used in the growth of oxide thin films – the traditional RHEED apparatus, and fixed-angle interferometry.

Reflection high-energy electron diffraction (RHEED) is performed by firing a beam of high-energy electrons at the growth surface at a shallow angle, usually no more than 5°, and

†. Alternate metallic evaporation methods exist if thermal effusion is insufficient – for example, materials with low vapor pressures would require techniques such as e-beam evaporation or use of metalorganic precursors.[47]

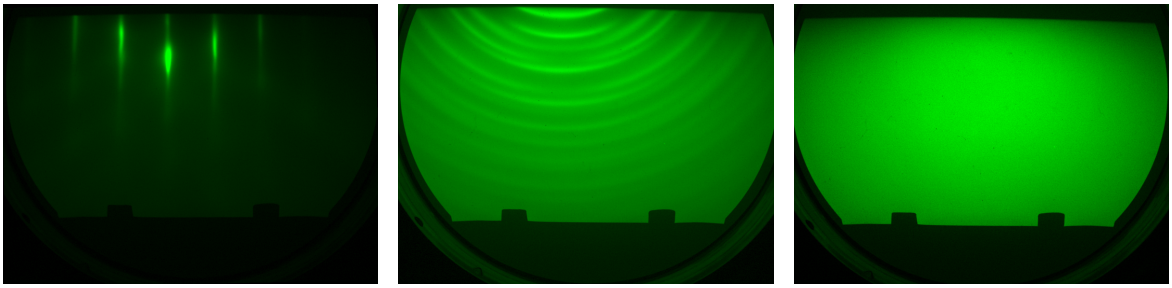

(a) Streaky pattern, indicating a single-crystal surface

(b) Ring pattern, indicating a polycrystalline surface

(c) No clear pattern, indicating an amorphous surface

Figure 3.2: RHEED patterns of different degrees of crystallinity

observing the diffraction pattern produced upon a phosphorescent screen oppose the electron gun. The diffraction pattern, which corresponds to the intersection of the Ewald sphere with the reciprocal space representation of the sample surface, allows for real-time evaluation of the sample surface during growth.[48] A schematic how the RHEED system is integrated into the growth chamber may be seen in Figure 3.1.

In Figure 3.2, one can see the distinguishing features of single-crystalline, poly-crystalline, and amorphous surfaces. Other patterns that may arise include chevrons around streaks indicating faceting, and arrays of transmission spots indicating 3D growth.[49] In addition to the broad characteristics of the surface, one can also use knowledge of the electron energy and chamber geometry to obtain additional crystallographic information, e.g., the spacing of the streaks in a streaky pattern corresponds to the lattice constant, the rings of a polycrystalline pattern will match the powder diffraction pattern for that material, or the reconstruction of a single-crystalline surface can tell us about the oxidation status of a thermally-cleaned silicon wafer.[46] Having this feedback during growth becomes a vital part of establishing growth quality, as discussed in Section 3.5.

In the case of streaky patterns indicating single-crystal growth, we can use the spacing of the streaks to obtain an estimate of the lattice parameter of the crystal via the Bragg scattering condition[46]

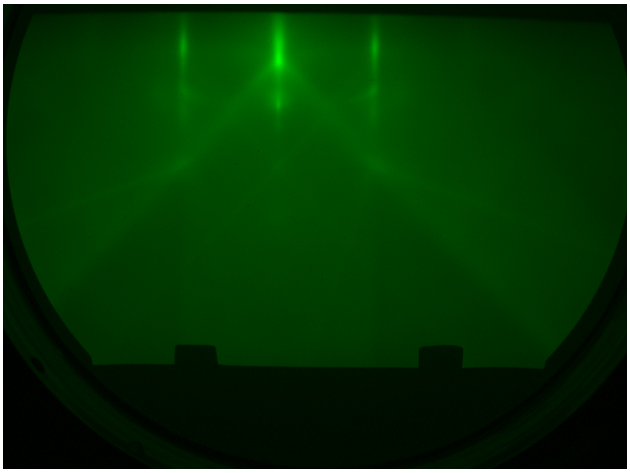

Figure 3.3: 1×1 reconstruction of the Si(001) surface in the Guha Lab MBE, with RHEED taken along the Si $\langle 100 \rangle$ azimuth. The distance between the center streak and the side streaks is 120 pixels, as relevant to Equation 3.1.

$$D = \lambda L / d \tag{3.1}$$

where D is the spacing between streaks, λ is the de Broglie wavelength of the scattered electrons, L is the distance between the scattering site on the sample and the RHEED screen, and d is the distance between atomic planes on the sample. A 15 kV electron (as is standard for our MBE tool) has a de Broglie wavelength of 0.099 Å. Knowing the lattice spacing of silicon, we can back out L for our system. Performing image analysis on a silicon substrate in the (001) orientation (see Figure 3.3), we can find D to be 120 pixels, and we know Si(001) has an atomic plane spacing of $d = 5.431/2$ Å $= 2.7155$ Å: thus $L = 3292$ pixels.† Taking into account the scale of the RHEED screen in pixels, this would be about 36 cm – an appropriate substrate-to-screen distance for our growth chamber. This information can be used to give us approximate crystal lattice plane spacings for our thin film samples.

Whereas RHEED tells us about the microstructure of the surface our substrate or film, interferometry on the other hand can tell us about the thickness of the film as growth

†. The RHEED screen camera on this MBE is kept at a fixed position for all measurements, and so pixels may be used as a consistent distance unit.

occurs. Since we are interested in oxide growths with wide bandgaps, we can safely assume that most of our thin films are transparent to visible light. We can shine a visible laser through our sample at a fixed angle, and look at the interference pattern produced by the distance between the film/substrate interface and the vacuum/film interface. The intensity of the laser over time may be fit to a sinusoid, where the period of the sinusoid is determined by the change in reflectivity of the material stack – vacuum above a transparent thin film upon a substrate of different refractive index – over time as growth occurs and increases the thickness of the thin film. The resulting interference fringes are a useful diagnostic for identifying successful growth of a transparent film as opposed to, e.g., unexpectedly slow growth due to a depleted metal charge.†

3.4 Erbium doping control in MBE

MBE allows for fine control of erbium dopant placement and concentration. Placement within MBE-grown thin film samples is governed by the Er cell shutter. For example, one could grow a layer of oxide thin film with the shutter closed, then open the shutter while growing another layer of thin film, then close the shutter and grow a third layer. This would produce a doped layer of the oxide removed from the oxide/substrate and oxide/air interfaces, reducing broadening effects caused by the interface.[23,20]

More prescient to this project is the control over doping levels. Heating the erbium charge within its effusion cell increases its vapor pressure, and when the cell shutter is open this greater vapor pressure results in a greater flux of erbium flowing towards the sample being grown. The greater the flux towards the sample, the greater the doping level of erbium.

One might consider this behavior to be like growing a very small amount of Er oxide within the oxide thin film being grown. While the stoichiometry may not correspond to a

†. Failed growth due to depleted metal charges has, unfortunately, happened a few times over the course of these projects. Thankfully, MBE usage time was rarely lost due to noticing the longer interference fringe period due to slower growth rates in the interferometer early in the sample growth.

CeO_2 Growth Rate (nm/hr)	T_{Er} = 800 ℃	T_{Er} = 900 ℃	T_{Er} = 1000 ℃
25	2.5 ppm	45 ppm	503 ppm
50	1.3 ppm	22 ppm	251 ppm
100	0.6 ppm	11 ppm	126 ppm
200	0.3 ppm	6 ppm	63 ppm

Table 3.1: Estimated Er doping levels in CeO_2 thin films grown at different growth rates and different Er cell temperatures T_{Er}, calibrated for the Guha Lab MBE.

proper Er oxide, this is a useful mental model in understanding doping concentration as a function of growth rate. If we imagine our sample oxide growth rate in proportion of the "Er oxide" growth rate, we can see that if we increase our sample growth rate by, say, a factor of two, the relative concentration of Er will go down by two.

We can see this in practice in Table 3.1. Based on measuring the thickness of a separately grown Er_2O_3 thin film calibration sample, we can determine the Er flux towards the sample surface depending on the cell temperature and back out the relative "growth rate" of the Er oxide versus the sample oxide. This gives us our doping concentration, if we also know the growth rate of our desired material. In the case of CeO_2, we have identified that, for example, we can achieve doping levels from less than 1 part per million (ppm) Er to over 100 ppm Er in CeO_2 films grown at 100 nm/hr (a fairly standard growth rate for CeO_2 in our MBE) simply by raising the erbium cell temperature from 800 ℃ to 1000 ℃. In this manner, we can access a broad range of doping levels – multiple decades, in fact – with only minor changes to our growth recipes. This degree of control is used to study a range of Er doping levels in Chapter 6.

3.5 Identification of binary oxide growth windows

In order to grow crystalline materials in MBE, source material must be introduced to the sample surface with appropriate stoichiometry. In the case of CeO_2 for example, sufficient

Ce and O_2 must be supplied that there is not an excess or deficit of either element. As an example, if insufficient O_2 were supplied, then an oxide of different stoichiometry might form, such as Ce_2O_3. In this section we will go through the process of obtaining the correct stoichiometry of CeO_2. In the context of MBE, this is referred to as finding the "growth window" for the desired material.

Fortunately, we do not look for the growth window blindly. For CeO_2, the resulting crystal will grow epitaxially if the stoichiometry is correct, identifiable as a streaky pattern in the RHEED. If the crystal is oxygen or cerium deficient, a polycrystalline crystal is formed, and rings will be seen in the RHEED.[50] (See Figure 3.2 for examples of these two patterns). With this in mind, the first step towards identifying the growth window is to measure the pressure of both the Ce and O_2 flux. Per Section 3.2, Ce is provided by a resistively-heated effusion cell, and O_2 is provided through a mass flow controller. By heating or cooling the effusion cell, we may increase or decrease the Ce flux. By increasing or decreasing the flow rate in the mass flow controller, we may correspondingly increase or decrease the O_2 flux.

Fluxes are generally measured using an ion gauge placed near the substrate position, and is referred to as the "flux gauge." Flux here is taken to be the "beam equivalent pressure," which is the pressure measured by the flux gauge when exposed to the beam of source material. In the case of CeO_2, we use the flux gauge and beam equivalent pressure quantity for measuring Ce fluxes, but due to the high oxygen pressures involved in CeO_2 MBE, we generally use the growth chamber's overall pressure ion gauge – which is out of line of sight from the oxygen source – to determine oxygen partial pressure. This is additionally viable since the mass flow controller flow rates are very stable, and less prone to drift than the thermally-controlled Ce flux.

To ensure we are taking accurate measurements with the flux gauge, we generally take Ce fluxes at three or four Ce cell temperatures. We then fit the measured beam equivalent pressures P versus cell temperatures T with a generic Clausius-Clapeyron equation, where

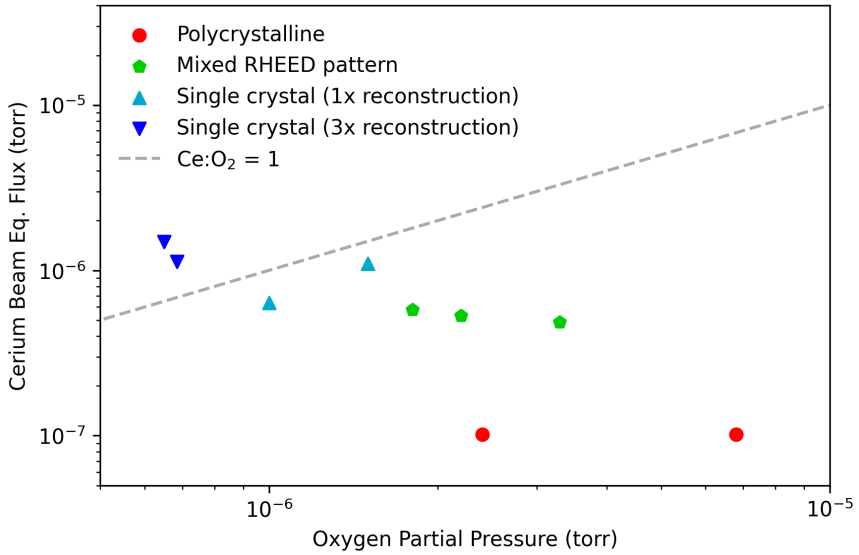

Figure 3.4: By varying the relative amounts of Ce and O_2 impinging upon the sample during growth, we can tune the stoichiometry of the CeO_2 thin film and by extension the nature of its crystallinity. We found that if the growth was cerium deficient, a polycrystalline material would form (marked in the figure by red circles). On the opposite side of the growth window, an oxygen deficient growth would start to form a streaky 3× reconstruction (blue inverted triangles), deviating from the expected streaky 1× RHEED pattern (teal triangles). At intermediate cerium deficient ratios, we identified a mixed RHEED pattern including both streaks and rings (green pentagons). An ideal pressure ratio of $Ce:O_2 = 1$ was identified, and is marked here by gray dashed line.

---

we additionally have the enthalpy of vaporization ΔH, the ideal gas constant R, and a compensating fit parameter b that accounts for an arbitrary reference temperature and the sensitivity of the ion gauge:

$$\ln P = -\frac{\Delta H}{RT} + b \tag{3.2}$$

For more information on this compensating fit parameter and our overall understanding of the Clausius-Clapeyron in the context of MBE, see Appendix A.

Having this equation allows us to reliably shift our Ce flux compared to our O_2 flux. If we identify that our Ce flux is too low by a factor of two, for example, we may use a properly fitted Equation 3.2 to increase our Ce flux pressure by that specific amount.

In the case of Ce:O_2 ratio for growing CeO_2, we are able to survey a range of ratios to identify our growth window. A summary of our survey is shown in Figure 3.4, where, by tracking the RHEED pattern across a series of ratios, we were able to identify that an equal pressure in the Ce beam equivalent flux and oxygen partial pressure via the growth chamber ion gauge would lead to optimal single crystal growth. At the two extremes, a cerium deficient growth led to polycrystalline rings in the RHEED pattern and an oxygen-deficient growth (within the ratios we were able to investigate) led to single crystal streaks albeit with a $3\times$ reconstruction, as opposed to the $1\times$ reconstruction we associate with stoichiometric CeO_2 growth.

Thus, we have identified the flux ratio growth window for CeO_2. Other growth parameters are discussed in Chapter 6, but identifying the growth window is an important part of the MBE method and so has been addressed here.

As a final note, this growth window may change depending on chamber geometry, the effusion cell being used for metal flux, the interface between the mass flow controller and the growth chamber, and a variety of other factors. As such, the growth window must be re-identified if any major changes are made to the MBE growth chamber. As an example of this, the growth window identified in Figure 3.4 is for a newer Ce effusion cell than the one used in Chapter 6 – the newer Ce cell has optimal growth conditions around Ce:$O_2 = 1$, but the old cell used previously had optimal epitaxial growth conditions around Ce:$O_2 = 20$. This is addressed with appropriate detail where necessary in that chapter.

3.6 Sample processing

Sample processing occurs prior and subsequent to growth via MBE. Before growth, substrates must be cleaned and brought to particular pre-growth conditions within the MBE. After growth, samples must be apportioned for various characterization methods. We review both of these steps here.

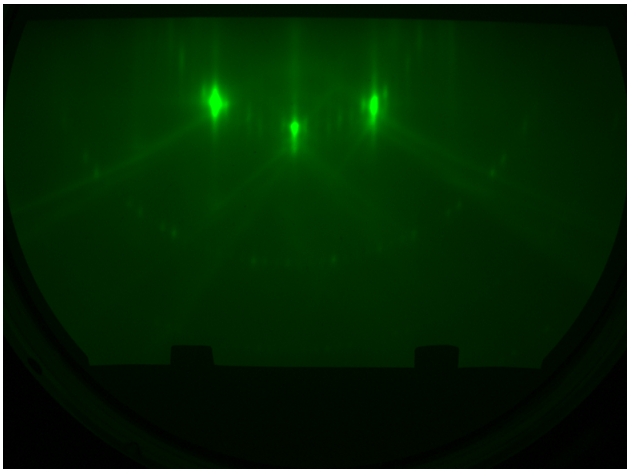

Figure 3.5: 7×7 reconstruction of the Si(111) surface in the Guha Lab MBE, taken along the Si $\langle 110 \rangle$ azimuth.

3.6.1 Substrate preparation

We typically grow on either silicon or oxide substrates. The two types of substrates have slightly different cleaning processes, both of which are detailed here.

Silicon (Si) substrates are cleaned prior to growth using a modified HF-last Radio Corporation of America (RCA) cleaning process consisting of a 10 minute soak in Standard Clean 1 (SC1)[†] at 80 ℃, followed by 5 minutes of sonication in deionized water (DI), and then a 30 second dip in hydrofluoric acid (HF) with a subsequent DI rinse.[51] This process results in a hydrogen-terminated silicon surface free from organic impurities or native oxide. Cleaned Si substrates are then outgassed in a dedicated vacuum chamber attached to the MBE at 300 ℃ for 30 minutes, which removes residual moisture and the hydrogen termination. The substrate is then loaded into the growth chamber. For (111)-oriented Si wafers, as used for CeO_2 growths, substrates are heated until the Si(111) surface achieves a 7×7 reconstruction (between 785-835 ℃)[‡] as observed via RHEED (Figure 3.5).

†. SC1 is a mixture of 1 part hydrogen peroxide, 1 part ammonium hydroxide, and 5 parts deionized water by volume.

‡. The substrate temperature is measured using an optical pyrometer that is calibrated against the Al-Si eutectic point at 577 ℃.[52]

Oxide substrates (such as $SrTiO_3$, also referred to as STO) are cleaned prior to growth by sonciation first in acetone for 5 minutes, then isopropanol (IPA) for 5 minutes. Cleaned oxide substrates are then outgassed in a dedicated vacuum chamber attached to the MBE at 300 ℃ for 30 minutes, which removes residual moisture. The substrate is then loeaded into the growth chamber and exposed to oxygen plasma for 20 minutes, with an O_2 flow of 2 sccm and a forward power of 350 to 375 W. This removes any organic residue from the oxide surface. The oxide substrate is monitored via RHEED to ensure the quality of the surface is suitable for growth, with the primary quality criterion being the streak sharpness after plasma cleaning.

3.6.2 Post-growth sample processing

After samples are removed from the MBE, they must be sized down for characterization – for example, a Si wafer starts as a 3" circle, but for optical measurements sample pieces must be no more than a few square millimeters in size.

The simplest method for cutting samples down to size is by cleaving. To cleave a sample grown on silicon or an oxide substrate, a diamond scribe is used to make a scratch in the sample surface parallel to a crystal plane. For silicon wafers, a scratch perpendicular to the primary flat is appropriate (such a scratch is along the (100) direction for Si(001) wafers, and along the (110) direction for Si(111) wafers). For oxide substrates, which typically come as square for our purposes, a scratch parallel to any edge will match a usable cleavage plane. Once a scratch is made, the sample is placed upon a wire, with the wire aligned with the scratch, and pressure is applied to either side of the scratch. The resulting force propagates the scratch into a full crack, and the substrate cleaves in two.† By cleaving multiple times, arbitrarily small pieces may be extracted from the original wafer.

A more consistent method for cutting samples down to size is by dicing. In this case,

†. Rather, the substrate is intended to cleave in two. In some unlucky scenarios, a brittle silicon wafer might shatter into three or more pieces. On the upside, such shatter events usually result in sharp cleaves.

a diamond saw is used to cut through the sample across an arbitrary path (though we often choose to align dicing saw cuts with cleavage planes, for experimental consistency). Water jets are used while cutting to wash away sample debris and keep the cut clean. To prepare for dicing, samples must be coated with a protective layer of resist (for example, 1805 photoresist) – a simple spin-on process (1 minute at 1000 rpm) plus a 5 minute resist bake is sufficient for these purposes, as the resist will not be used for patterning and so does not need to be perfectly uniform. After dicing, the protective resist must be removed from the samples before measurement. A dip in N-methylpyrrolidone (NMP) is sufficient for a fast clean, but to be thorough, samples are soaked overnight in NMP at 50 ℃, then sonicated for 5 minutes first in acetone and then in isopropanol (IPA), before being blow-dried with dry nitrogen. Once cleaned, the samples may be measured without additional processing, as needed. A common dicing format for our lab is 2 mm $\times$ 25 mm slices, which is the appropriate size for mounting in the supercell tubes used for electron paramagnetic resonance (EPR) measurements.

The final sample processing method is focused ion-beam (FIB) milling, which is used to prepare samples for cross-sectional transmission electron microscopy (TEM).[53] To prepare for FIB, a cleaved or diced piece of sample is coated with a protective 100 nm layer of gold. Micron-scale trenches are then milled into the gold-coated sample using a FIB tool, and then the sample is rotated such that the exposed substrate is milled through to release a thin strip of sample, referred to as a lamella. The lamella is attached to a manipulator probe and transferred to a TEM grid, where it is mounted and then thinned down to no more than 50-100 nm thick. Once prepared like this, the lamella may be characterized via TEM.

CHAPTER 4

EXPERIMENTAL METHODS FOR CHARACTERIZING OXIDE THIN FILMS

In tandem with characterizing the directly quantum-relevant properties of our Er-doped oxide thin films, we must understand the environment in which we are putting our qubits-to-be. To that end, we perform a variety of microstructural characterization techniques to obtain information about the crystal structure of our samples.

The bulk of our characterization happens via either X-ray characterization, or some form of electron microscopy. X-ray characterization generally tells us aggregate information about the microstructure of our sample (e.g., typical cation valency or distribution of lattice constant across the film) whereas electron microscopy yields specific microstructural information over smaller representative regions of our samples (e.g., structure at the interface or surface morphology).

4.1 X-ray characterization

4.1.1 X-ray diffraction measurements

X-ray diffraction (XRD) is an efficient method of determining the lattice parameters of a crystalline sample. X-rays of wavelength λ, usually the Cu K-α line of $\lambda = 1.5406$ Å, are impinged upon a crystalline sample at some angle θ, with a detector set up at an equivalent angle such that X-rays leave the sample and are collected with the subtended angle 2θ. The peaks in XRD are due to solutions of the Bragg condition for a lattice plane spacing d and the peak order $n \in \mathbb{Z}_{>0}$, which is as follows:

$$n\lambda = 2d \sin\theta \tag{4.1}$$

In the simple case of a cubic system, the plane spacing d is determined from the lattice parameter a and the Miller indices (h, k, l) of the plane being probed. Those quantities are related by:

$$d = \frac{a}{\sqrt{h^2 + k^2 + l^2}} \tag{4.2}$$

We can then invert this relationship to find the lattice parameter a from a peak position 2θ, assuming we know the expected Miller indices for the plane being measured.

$$a = \frac{n\lambda}{2\sin\theta}\sqrt{h^2 + k^2 + l^2} \tag{4.3}$$

This is precisely the analysis we use in Section 6.3 to identify the Si(111) peak and CeO_2(111) peak in XRD.

4.1.2 X-ray absorption spectroscopy

X-ray absorption spectroscopy (XAS), performed in this study at Beamline 29 ID-D of the Advanced Photon Source at Argonne National Laboratory, enables the study of the local electronic structure of our samples.[54] In particular, XAS allows us to probe the valency of our samples by looking at absorption peaks when exciting core electrons with high energy photons into the continuum band – via X-ray photons with energies in the keV range. The particular feature used in these studies is that the XAS spectrum changes based on the valency of the element being studied – in our case, we look at the variation in peak positions between Ce^{3+} XAS spectra and Ce^{4+} XAS spectra, as described in Chapter 6.

4.2 Electron microscopy techniques

4.2.1 Scanning electron microscopy

Scanning electron microscopy (SEM) involves the emission of an electron beam at a sample, and then detecting electrons that have backscattered from the sample.[55,56] To image across a large area of a sample, the electron beam is rastered across the viewing area, and an image is constructed by counting the number of backscattered electrons at each point in the raster. SEM allows for viewing features significantly smaller than viable in optical microscopy, with observation of feature sizes as small as 10 nm reasonable even on mid-tier SEM tools.

In the context of these studies, SEM has been used to observe the crystallite shape, size, and orientation of non-single-crystal samples. SEM is additionally used as the imaging method when extracting lamellae of samples via the FIB process.

Fortunately for our purposes, the silicon upon which most of our samples are grown is conductive, and so is easily imaged by a scanning electron microscope. In those situations where we use oxide substrates however, the oxide substrates accumulate charge when the SEM attempts to scan them, and this charging effect prevents quality SEM images from being obtained

4.2.2 Transmission electron microscopy (TEM)

Transmission electron microscopy (TEM) involves the emission of an electron beam at a sample, and then detecting electrons that have successfully been transmitted through the sample.[57] As in SEM, to image across an area of a sample, the electron beam is rastered across that area, and an image is constructed based on the intensity of the transmitted beam at each point. This refined technique is referred to as scanning transmission electron microscopy (STEM).

In order for our samples to be thin enough for transmission to consistently occur, lamellae

must be extracted via the FIB milling process. As a reward for such effort however, TEM allows for atom-scale resolution, with direct viewing of the crystal lattice being a straightforward task once the sample is prepared and the TEM correctly calibrated. When lamella are prepared such that the cross-section of the sample is viewed, the technique is alternatively referred to as cross-sectional TEM (XTEM).

For our studies, XTEM is used to view interfaces between substrates and thin films, image strain fields propagating through our thin films such as those caused by threading dislocations, and by happenstance as a high-precision method of measuring the thickness of our samples.

Beyond just imaging, TEM tools are also often equipped with energy-dispersive X-ray spectroscopy (EDX) functionality, which uses the incident electron beam to promote an inner shell electron outwards – when the resulting hole is filled in, X-ray wavelength radiation is released, with characteristic wavelengths depending on the excited element. By scanning an electron beam over a sample, TEM tools not only can image the sample, but also provide basic elemental analysis across small regions. This kind of analysis is used to determine the composition across the CeO_2/silicon interface for the samples observed in Chapter 6.

4.3 *Ex-situ* thickness measurements

Measuring our thin film thicknesses after growth is a vital part of the feedback loop of MBE growth control. Part of this is to characterize quantities such as distances from interfaces, which we know to have an impact on rare-earth optical properties.[20] More importantly in the context of this work however, measuring our thickness after the fact confirms our growth rate, which in turn confirms the Er doping level in each thin film. (Recall that, in Section 3.4, Er doping levels are dependent both on Er cell temperature and thin film growth rate.)

There are several ways to measure thin film thicknesses, but for this study we primarily used two techniques: Optical interferometry, and cross-sectional TEM.

Cross-sectional TEM is a laborious undertaking due to the difficulty of extracting lamella from our thin films, but it provides the highest accuracy measurement. Optical interferometry (via a Filmetrics F40 thin film thickness analyzer) on the other hand is simple and fast, but suffers in terms of accuracy due to co-variation between thickness and refractive index. In the context of this work, we established a ground truth thickness via TEM for a limited set of samples, verified the optical interferometry measurements against that ground truth, and then performed optical interferometry with that calibration in place.

This process provides us with reliable thickness, and subsequently reliable growth rates and doping levels. Table 6.1 gives an example of how this process may be used in the experimental setting.

CHAPTER 5

EXPERIMENTAL METHODS FOR MEASURING ER ENERGY STRUCTURE IN OXIDE THIN FILMS

5.1 Characterization of optical spectra

In this section we will discuss characterization of the ${}^4I_{13/2} \leftrightarrow {}^4I_{15/2}$ transitions and the optical spectrum built up from the crystal field splitting in the two levels. We use multiple techniques to examine different aspects of Er:oxide optical transitions, which are examined here. The configuration of our optical setup is described in Section 5.1.1, and the measurements performed using that optical setup are described in Sections 5.1.2 to 5.1.4.

A major aspect of characterizing energy spectra, including optical spectra as in this case, is identifying both the inhomogeneous linewidth and the homogeneous linewidth: In the case of an ensemble of optically active defects, in our case Er, each defect will have some linewidth inherent to its own optical transitions; each defect will additionally have some resonance shift from the expected center resonance, leading to a distribution of resonances across the ensemble.

The single-defect linewidth, referred to as the "homogeneous linewidth," may be interpreted as the uncertainty in the energy emitted when the defect's transition occurs. The homogeneous linewidth, represented by Γ_{hom}, is inversely related to the coherence time, or rather, the duration for which a state may successfully maintain a coherent superposition: $\Gamma_{\text{hom}} = 1/\pi T_2$, for a coherence time T_2. In the case where there are no additional decoherence-causing processes, Γ_{hom} will be limited only by the radiative lifetime, such that $T_2 \sim T_1$.[14] Broadening of the homogeneous linewidth may additionally be caused by dynamic processes that act as perturbations on the individual defect's transition frequency or phase,[18] with corresponding decrease in the coherence time.

The ensemble linewidth due to shifts in resonance in each defect, referred to as the

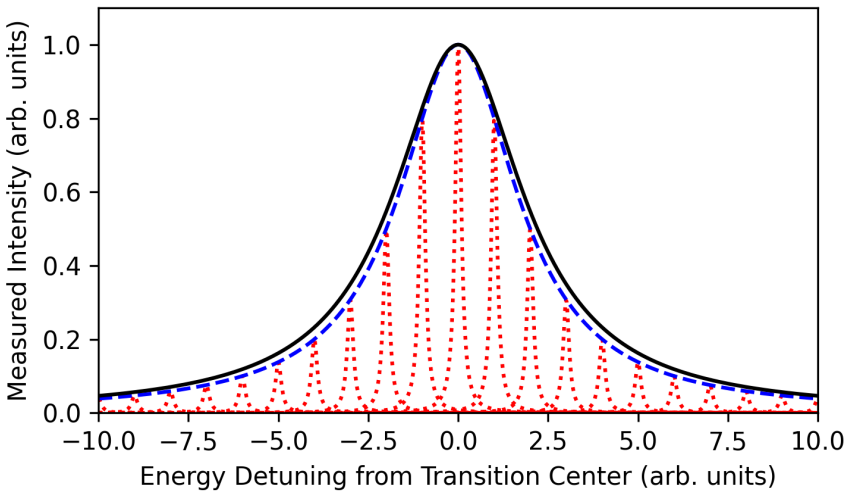

Figure 5.1: Schematic of the relationship between the homogeneous linewidth of individual defects (represented by red dotted lines), the inhomogeneous linewidth of the ensemble of defects spread around the transition frequency (blue dashed line), and the convolution of the two that is measured via photoluminesence and photoluminesence excitation spectroscopy (black solid line).

"inhomogeneous linewidth," may be interpreted as the spread of the defect resonances due to inconsistencies in the defect environments. For example, the crystal field may be strained near interfaces, or the presence of other randomly-placed dopant defects may lead to slight variations in the environment of a given defect compared to its neighbor. The aggregate of this shifting produces the inhomogeneous linewidth Γ_{inh}.

The profile of an Er optical transition as measured by photoluminesence or photoluminesence excitation spectroscopy (as described in the coming sections) is the convolution of the homogeneous and inhomogeneous profiles.[58] The two profiles will be Lorentzians for the doping densities at which we are working, resulting in measured profile linewidths that are simply the sum of Γ_{inh} and Γ_{hom}.[18] (A schematic of this relationship is shown in Figure 5.1.) However, homogeneous linewidths for low-doped Er in oxides are usually in the MHz to single GHz range, whereas the inhomogeneous linewidths are in the 10s of GHz range at minimum.[14] As such, $\Gamma_{\text{hom}} \ll \Gamma_{\text{inh}}$ and we may directly take the measured profile linewidths as the inhomogeneous linewidths. The homogeneous linewidth must then be

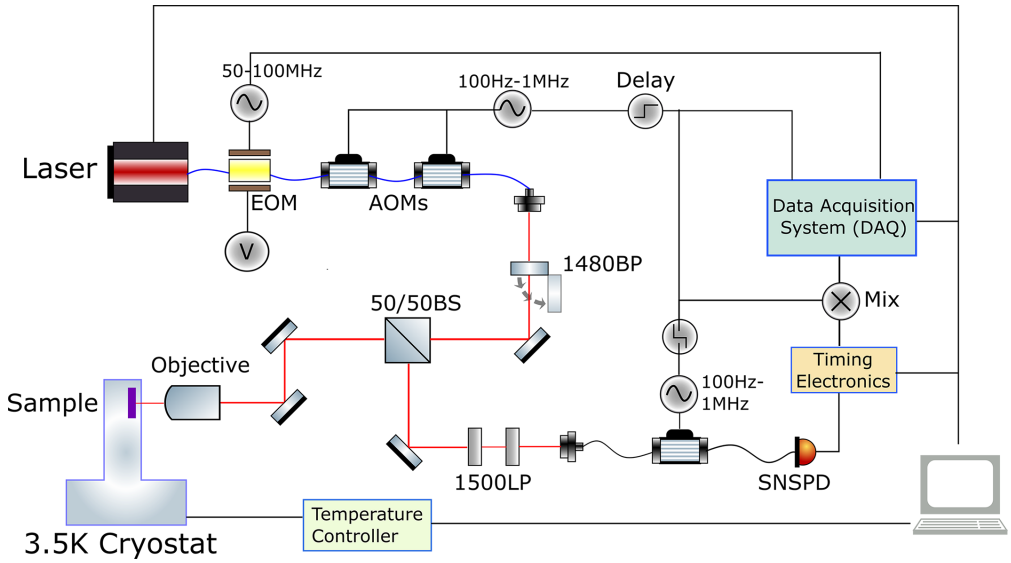

Figure 5.2: Schematic of the optical setup used for near-IR photoluminesence excitation spectroscopy measurements. 1.5 μm light is routed from the laser through the fiber-coupled EOM and AOMs to produce appropriate excitation pulses, then passed into free space and through the beam splitter to the objective, where the laser is focused onto the sample. Light is then collected through the other path of the beam splitter back into the fiber network, gated by an additional AOM, and then detected via the SNSPD. Diagram reproduced with permission from Zhang *et al* 2023. DOI: 10.48550/arXiv.2309.16785

---

measured via other methods such as transient spectral holeburning (Section 5.1.3) or optical echo (Section 5.1.4).

5.1.1 Description of the optical setup

Measurement of the ${}^4I_{13/2} \leftrightarrow {}^4 I_{15/2}$ transitions available to Er^{3+} is performed by laser excitation of the samples at or near resonance to one of the Er transitions Z_i-Y_j, followed by filtering out of the laser excitation, and finally analysis of collected erbium emission. We use multiple experimental configurations to examine different aspects of erbium spectra, which we review here. The base configuration of our optical characterization setup is as shown in Figure 5.2, and is described in the following paragraphs.

For this research, we have performed optical characterization using a custom confocal microscopy setup designed for telecom C-band spectroscopy, with samples mounted in a cryostat

at 3.5 K (s50 Cryostation, Montana Instruments). Custom Python scripts are used to control the experimental configuration, such as sample temperature, excitation wavelength, and pulse timings. The measurements employ a Toptia CTL 1500 continuously-tunable diode laser with a wavelength range of 1460 nm to 1570 nm, an absolute accuracy better than 0.15 nm, and a relative accuracy of better than 0.01 nm. The laser head delivers greater than 50 mW of power, which results in up to 1 mW of power incident upon the samples after passing through the setup.

The laser is first passed through an electro-optic modulator (EOM) module. The EOM module may employ either an intensity EOM or a phase EOM, depending on the measurement being performed. Details of the respective EOMs are discussed in the respective measurement sections. The tunable laser signal is then passed through a pair of fiber-coupled acousto-optic modulators (AOMs) with a rise time of 30 ns (MT80-IIR30-Fio-PM0.5-J1-A-Ic2, AA Opto Electronic) for pulse shaping, and then passed into free space. If wavelengths in the 1470 nm to 1490 nm range are used, a 1480 nm bandpass filter is brought into the laser path to prevent leakage of excess amplified spontaneous emission from the laser, which emits at >1500 nm. (The bandpass filter state is toggled frequently since 1473 nm light is used for laser path focusing and alignment, and so the filter is mounted on a motorized flip mount.) Laser light is then routed through a 50:50 beam splitter, through a three-axis periscope stage (Newport), and into a 0.65 NA objective lens focused on the thin film sample mounted within the cryostat.

Photons emitted from the sample are collected by the objective lens, then routed back to the 50:50 beam splitter, where the photons are directed through a pair of 1500 nm longpass filters (ThorLabs FELH1500) to filter out any 1470 nm to 1500 nm laser light, and then collected back into the fiber network by a dedicated collimator. The collected light is gated by an additional AOM (AMM-55-4-50-1550-2FP, Brimrose) to prevent overloading of the detector during laser excitation. The collected and gated light is detected with a

superconducting nanowire single-photon detector (SNSPD) housed within a second cryostat and optimized for near 1.5 μm detection at near 80% quantum efficiency (Quantum Opus).

Event timing for the AOMs is governed by a Pulse Streamer 8/2 (Swabian Instruments), and additional static parameters (such as laser wavelength, periscope position, and AOM attenuation) are set by network and USB connections plus a DAQ for delivering fixed voltage signals. Single photon counting is handled by a Time Tagger Ultra (Swabian Instruments), which is synchronized to the Pulse Streamer by a dedicated clock signal.

A variant of this setup is used for performing continuous measurements with a spectrometer. Strictly using laser light shorter than 1500 nm, all AOMs are simultaneously opened for continuous laser excitation and light emitted from the samples at longer than 1500 nm is routed to a low-noise InGaAs camera (PyLoN IR, Princeton Instruments) instead of the SNSPD.

An additional variant of this setup is used for performing pulsed measurements under a vector magnetic field. Instead of the s50 cryostat, samples are placed in a BlueFors dilution refrigerator equipped with fiber-coupled optical access and a 3-axis electromagnet, with field strengths up to 250 mT. To route light to the dilution fridge, the excitation and collection path AOMs are connected to ports 1 and 3 of a fiber-coupled circulator (ThorLabs 6015-3-APC), with port 2 connected to the dilution fridge optical access port to illuminate the sample with laser light and route emitted light back towards the SNSPD. The sample temperature in the dilution fridge is held at 3.5 K to match measurements performed in the cryostat.

5.1.2 Photoluminescence and photoluminescence excitation measurements

Photoluminescence (PL) and photoluminescence excitation (PLE) spectroscopy are two methods for observing the positions and inhomogeneous linewidths of optical transitions, in our case between the Er^{3+} Z levels and Y levels.

In PL, the excitation laser is tuned to at or above the energy required to excite Er ions from the Z_1 state to the highest Y state, either Y_5 for a cubic site of Y_7 for a non-cubic site. The excitation laser is operated continuously, with excitation and collection AOMs fully open without any pulsing. For Er:CeO_2, we may use a laser wavelength of 1473 nm for this purpose. The 1473 nm light excites the Er ions, which then non-radiatively into the Y levels. Radiative decay then occurs from the Y levels into the Z levels, and emission occurs at wavelengths corresponding to Y_i-Z_j transitions. Most of these transitions have wavelengths longer than 1500 nm, so we use long pass filters to filter out the laser light before routing the emission from the samples to the spectrometer. We may then observe the peak locations, intensities, and linewidths for transitions corresponding to the decay from Y_i levels to Z_j levels (given their emission wavelengths are longer than 1500 nm).

By contrast, in PLE, the excitation laser wavelength is swept resonantly across a particular Z_i to Y_j transition. AOMs are used to shape the laser signal into a 1.5 ms excitation pulse, after which the laser is gated to no longer illuminate the sample. This begins the collection period, which may be anywhere from 3 to 10 milliseconds long, depending on the needs of the measurement and the sample being measured. During the collection period, the Er ions slowly decay from the Y_j level into which they were excited during the excitation interval back down into the Z levels. As the Y_j level depletes, the intensity of the emission decreases over time – this produces a characteristic decaying exponential over the time t, with intensity $I(t) \propto e^{-t/T_1}$ yielding the excited state lifetime T_1. By summing all of the photon counts recorded for a single wavelength, the total amount of Er ion absorption from Z_i to Y_j is established. By counting the total number of counts at wavelengths stepped across a given transition, an inhomogeneous lineshape is established. An example of a PLE measurement is shown in Figure 5.3, where the excitation wavelength was swept from 1529.5 nm to 1532 nm in 0.02 nm steps, and the excitation/collection process was repeated 12,000 times at each wavelength – the integrated counts from the lifetime measurements at each

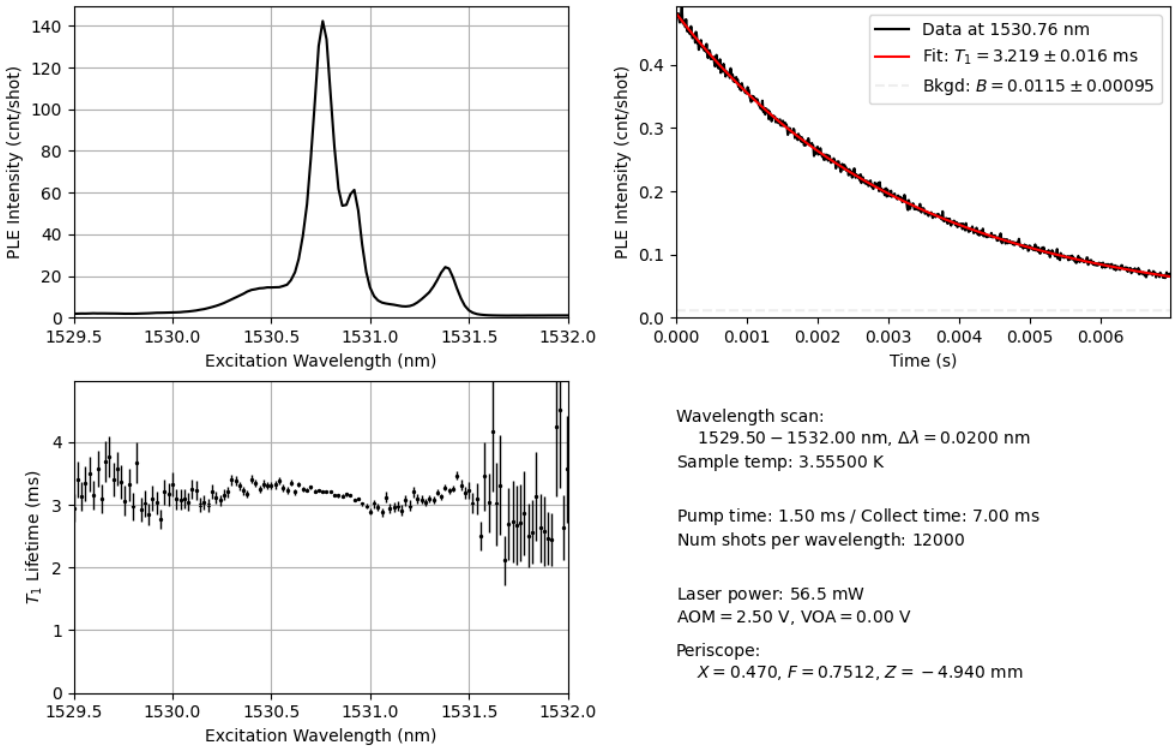

Figure 5.3: A standard example of data produced by a photoluminescence excitation (PLE) spectroscopy scan, in this case upon a 750 nm thick, 15 ppm Er CeO_2 thin film grown on silicon. The upper left panel shows the resulting PLE spectrum obtained by integrating time-resolved counts at each wavelength, the upper right panel shows the time-resoled decreasing counts over time corresponding to the excited state lifetime T_1 at the maximum of the spectrum, and the lower left panel shows T_1 as a function of the excitation wavelength. The lower right section of the figure shows the experimental conditions used for this scan, such as a collection duration of 7 ms and a sample temperature reading of 3.56 K.

---

wavelength, shown in the top right panel, generated the PLE spectrum in the top left panel.

Excited state lifetime T_1 measurements require no further analysis – they are effectively a byproduct of the PLE measurement procedure, and can be fit automatically as measurements are taken. To obtain inhomogeneous linewidths however, the Lorentzians must be fit against each peak, taking careful note to perform the fitting in energy or frequency space (to obtain a linewidth in GHz, meV, etc.) instead of in wavelength space.

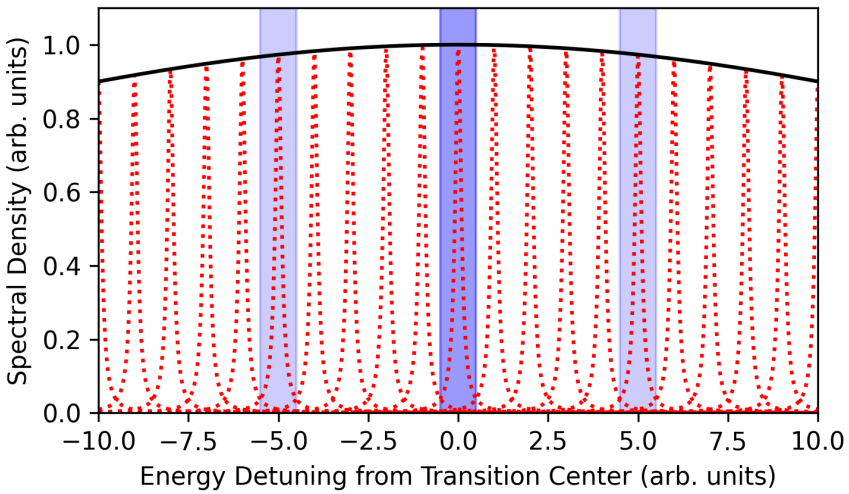

Figure 5.4: A schematic of the interaction of an ensemble of emitters and the three laser peaks used for transient spectral holeburning (TSHB). In this image, a population of defects with homogeneous linewidths (indicated by the red dotted lines) are spread across a broad inhomogeneous distribution (indicated by the black line). Incident laser peaks are indicated by blue bands – including the sidebands detuned by ±5 units allows the excitation of an additional two defects for a total of three, compared to just one defect if all the laser peaks are tuned to zero detuning energy units. The transition from one defect being excited to three defects being excited is governed by the homogeneous linewidth of the emitters, as described in Section 5.1.3.

5.1.3 Transient spectral holeburning measurements

Transient spectral holeburning measurements (TSHB) are an ensemble measurement performed to measure the spectral-diffusion limited homogeneous linewidth, usually referred to as the spectral diffusion linewidth or the holeburning linewidth. TSHB is performed with a similar process to PLE, where we run excitation/collection processes while stepping an independent variable, and integrate the result at each step. In the case of TSHB however, the excitation laser is fixed to be on-resonant with a crystal field transition identified by PL or PLE, and the independent variable is the detuning of a set of sidebands from the center laser frequency.

To explain further: a phase electro-optic modulator (EOM, iXblue) is placed into the optical path as shown by the EOM block in Figure 5.2, where it modifies the laser excitation

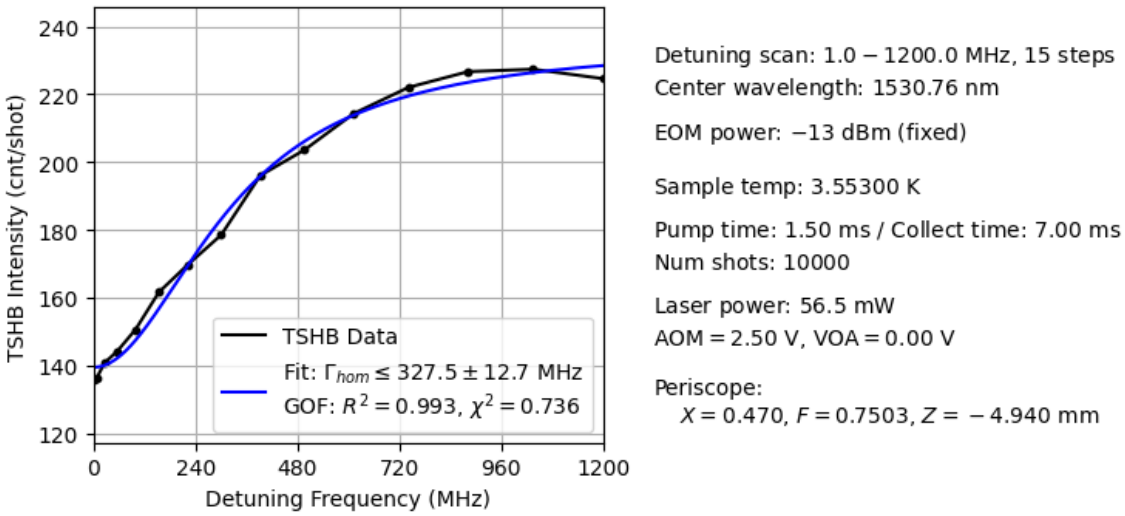

Figure 5.5: A standard example of data produced by a transient spectral holeburning (TSHB) scan, in this case upon a 750 nm thick, 15 ppm Er CeO_2 thin film grown on silicon. The left panel shows the resulting holeburning curve obtained by integrating counts at each detuning frequency. A Lorentzian fit is automatically applied to the holeburning curve. The right section of the figure shows the experimental conditions used for this scan, such as a detuning range maximum of 1200 MHz and a sample temperature reading of 3.55 K.

---

by an oscillating phase modulation. This phase modulation generates additional distinct laser peaks, offset from the center laser frequency – these additional peaks are referred to as "sidebands," and are spaced equally from the center laser frequency. These sidebands may be detuned from the center laser peak between 1 MHz and 6 GHz, with the detuning range restricted by the laser jitter (for our system, $\sim$ 1 kHz to $\sim$ 1 MHz uncertainty in the laser emission frequency) on the low-frequency end and by the maximum frequency of the signal generator (SRS 396) used to control the phase modulation on the high-frequency end.

The central idea of the TSHB measurement is as follows: At zero sideband detuning, the three laser peaks all interact with the same sub-ensemble of erbium within the inhomogeneous distribution. In Figure 5.4, the three laser peaks are all within the dark blue band at zero detuning, and only one homogeneous profile would be under resonance and being saturated – when laser excitation is lifted, one unit of intensity is counted as emitted from the sample. At large detuning, the three laser peaks are all fully separated from each other, as the

lighter blue bands are distinct from the dark blue band in Figure 5.4. In this case, three homogeneous profiles are under resonance and being saturated – so when laser excitation is lifted, three units of intensity are counted as emitted from the sample. In intermediate regions between zero detuning and large detuning, the increase in intensity corresponds to the homogeneous profile of the Er ions within the ensemble.[22,29]

The resulting lineshape when detuning is swept is a Lorentzian with full-width at half-max (FWHM) Γ_{TSHB}, and the actual homogeneous linewidth is upper bounded by half the value of Γ_{TSHB} – rather, $\Gamma_{\mathrm{hom}} \leq \Gamma_{\mathrm{TSHB}}/2$. When discussing the results of TSHB measurements, this upper bound linewidth is sometimes referred to as the spectral diffusion linewidth $\Gamma_{\mathrm{SD}} = \Gamma_{\mathrm{TSHB}}/2$. A practical example of this measurement is shown in Figure 5.5, with the Lorentzian fit applied and Γ_{SD} shown.

5.1.4 Optical echo measurements

Optical echo measurements, also referred to as photon echo measurements, is an alternative method – complementary to TSHB – for finding the homogeneous linewidth Γ_{hom} of the optical transition. Whereas TSHB can probe a minimum Γ_{SD} of 1 to 5 MHz, optical echo can probe a maximum Γ_{hom} linewidth of ~ 1 MHz.

In photon echo, two laser pulses, both on-resonant with a particular transition, illuminate the sample in quick succession. The first pulse produces a superposition between the ground state and the excited state – a $\pi/2$ pulse, in Bloch sphere parlance. After a delay time τ during which the illuminated defects dephase with each other, another pulse is supplied, reversing the populations of the ground and excited state – a π pulse – and as such reversing the dephasing process that occurred during the delay time. When the defects re-phase a duration τ after the π pulse, a coherent optical pulse is generated by the ensemble.[14,59]

AOMs are relatively slow (with opening and closing times in the 10s of nanoseconds), and so an intensity electro-optic modulator (EOM, iXblue) is added to the optical setup

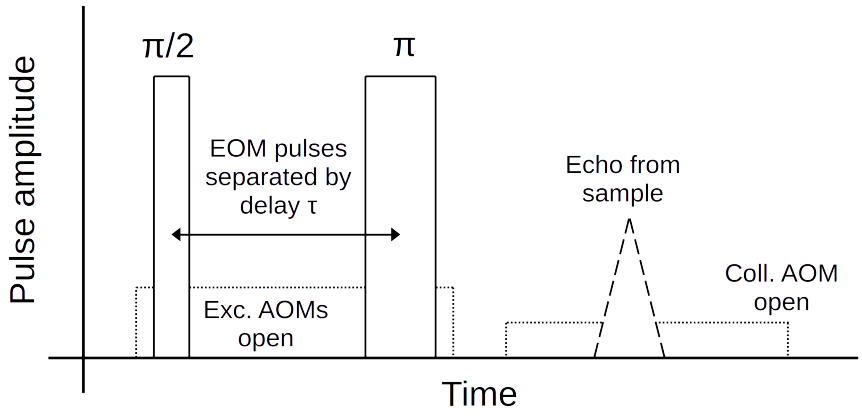

Figure 5.6: Schematic of the photon echo pulse sequence as described in Section 5.1.4 Note times and amplitudes are not to scale. Subsequent $\pi/2$ and π pulses separated by a delay time τ cause an coherent optical pulse to be released at a time 2τ after the $\pi/2$ pulse, due to the induced rephasing caused by the π pulse.

---

as the EOM block in Figure 5.2 to supplement pulse generation for these measurements. The intensity electro-optic modulator is operated in much the same way as the AOMs, with electrical logic pulses causing the EOM to open and close. However, the EOM opening and closing speed is much faster (on the order of 1s of nanoseconds).

A practical schematic of this process is shown in Figure 5.6. To reduce laser-bleedthrough, we start with both the intensity EOM and the excitation AOMs closed. First the excitation AOMs are opened (this is a relatively slow process, taking up to 30 ns), after which the $\pi/2$ pulse is produced by briefly opening the EOM. After the delay time τ, for our experiments ranging from 180 ns to 700 ns, the π pulse is supplied by opening the EOM again, and then both the EOM and the excitation AOMs are closed. The collection AOM is then opened, and the photon echo from the sample is observed on the detector. The collection AOM is then closed, and the process repeats.

In our setup, the excitation laser is set to be resonant with the Y_1-Z_1 transition of our samples (discussed in Chapter 6), with laser power tuned to produce $\pi/2$ and π pulse areas.[60] We have selected a 10 ns $\pi/2$-pulse followed by a 20 ns π-pulse after a delay τ between 180 ns and 700 ns. The length of the $\pi/2$ pulse is limited to at least 10 ns, as that is the

shortest possible pulse enabled by our instrumentation. This shorted possible pulse is used to minimize dephasing during the excitation process.

Now that we understand the measurement process, we note that TSHB and optical echo additionally probe different sets of ions within the ensemble. TSHB accumulates all decoherence processes over the course of a long ($\sim$ 1 ms) excitation period – and so, both fast and slow processes will contribute to the measured linewidth. On the other hand, optical echo measurements occur over very short times ($\sim$ 1 μm), and the dynamics involved cause the slow decoherence processes to be compensated for – so only the fast decoherence processes are included in the optical echo-measured homogeneous linewidth.

5.2 Characterization of spin spectra

In this section we will discuss characterization of the Zeeman-split $^4I_{15/2}$ spin transitions, and the spin resonance spectra built up from that energy structure. We primarily use electron paramagnetic resonance (EPR) for this investigation, which is described in Section 5.2.1. The measurements performed using the EPR technique are described in Section 5.2.2 and 5.2.3. Another method is that of optically-probed spin lifetime measurements, which is discussed in Section 5.2.4.

5.2.1 Description of electron paramagnetic resonance

Electron paramagnetic resonance (EPR) is an experimental method where in the Zeeman resonance condition – $h\nu = g\mu_B B$ for an electron spin-1/2 system – is set up for magnetically active samples, and the behavior of the sample at and around resonance is investigated. The resonance condition requires two parameters be established by the experimental conditions – the magnetic field B, and the frequency ν. The g-factor g dictates where the resonance occurs and is the parameter under test, and the Planck constant h and the Bohr magneton μ_B are constants.

The apparatus used for EPR measurements is described in detail in a number of excellent texts,[61,62] so we will not discuss the apparatus in this section. However, we will make note of a few considerations that arise in our experiments. Namely, the magnetic field B is provided with a specific orientation. We are mainly concerned with the direction of the static magnetic field with respect to the sample, particularly if the g-factor is anisotropic. We can align the samples with respect to the magnetic field within a precision of a few degrees - this alignment is noted where needed. Additional experimental considerations are discussed for the two types of EPR performed in these studies.

5.2.2 CW measurements

Continuous wave (CW) X-band ($\nu \sim 9.5$ GHz) EPR experiments were carried out with a Bruker ELEXSYS II E500 EPR spectrometer (Bruker BioSpin), equipped with a TE_{102} rectangular EPR resonator (Bruker ER 4102ST). Field modulation at 100 kHz in combination with lock-in detection leads to first derivative-type CW EPR spectra. Measurements were performed at cryogenic temperatures between 4.0 and 4.2 K, with temperature governed by a helium gas-flow cryostat (ICE Oxford) and an ITC (Oxford Instruments). Er:CeO_2 samples, as discussed in Chapter 6, were mounted with the static magnetic field parallel to the Si$\langle 110 \rangle$ axis after being diced to the appropriate size to fit within EPR supercell tubes. Measurements use a field modulation of 1 mT, a microwave power attenuation of 35 dB (from 200 mW), and a field step size of 0.2 mT.

5.2.3 Pulsed measurements

Pulsed X-Band ($\nu \sim 9.7$ GHz) EPR experiments are taken using an ELEXSYS E580 spectrometer (Bruker Biospin) equipped with a dielectric ring resonator (Bruker ER 4118X-MD5). Er:CeO_2 samples, as discussed in Chapter 6, were mounted with the static magnetic field parallel to the Si$\langle 110 \rangle$ axis after being diced to the appropriate size to fit within EPR

supercell tubes. The supercell tubes were suspended in the center of the dielectric ring resonator contained in a flow cryostat (Oxford Instruments CF935) with pumped liquid helium. The data shown in the manuscript are obtained at 3.6K with temperature controlled by an ITX temperature controller (Oxford Instruments).

For spin echo field sweep measurements, a two-pulse Hahn echo sequence[61] is applied with a 12 ns $\pi/2$-pulse followed by a 24 ns π-pulse with a fixed delay τ of 100 ns. The pulse length is chosen for the shortest achievable length to cover a large bandwidth of spin ensemble. For spin coherence measurements, the same Hahn echo sequence is used with a varying delay τ ranging from 100 ns to 1300 ns. For spin relaxation measurements, a three-pulse population inversion sequence is used where a 24 ns π-pulse is followed by a two-pulse Hahn echo sequence with varying time delay τ. The two-pulse Hahn echo sequence used here is composed of a 12 ns $\pi/2$-pulse followed by a 24 ns π-pulse with a fixed delay τ of 100 ns.

5.2.4 Optical spin lifetime measurements

Optical probing of spin relaxation dynamics was carried out using the dilution refrigerator configuration of the optical setup described in Section 5.1.1. The specifics of the magnetic field and pulse sequence used are closely related with the samples being measured, and so the reader is invited to review this section again after reading the first parts of Chapter 6.

To begin the optical spin lifetime measurement, the spin levels in the Z_1 and Y_1 states are split by applying a magnetic field using the dilution fridge's vector magnet. The excitation laser wavelength is then identified based on the g-factor of the Er ions, and tuned to excite from the Z_1 spin-down level to the Y_1 spin-up level.

A 100 μs pulse at this resonance depletes the population of electrons in the Z_1 spin-down level. The pulse length is chosen to be longer than optical π pulse for improved optical contrast but short enough that emission from Y_1-Z_1 transition does not alter the electron populations between the Z_1 spin-up and spin-down states too dramatically. The relaxation

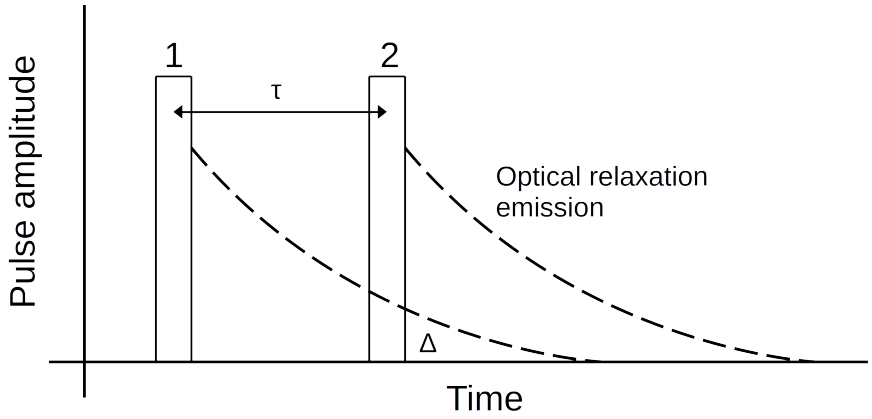

Figure 5.7: Two pulse sequence for optically measuring spin T_1. The first pulse, labelled 1, slightly depletes the Z_1 spin-down state. The second pulse, labelled 2, measures the population of the Z_1 state after a delay τ by integrating the optical relaxation emission. The combined emission from the two pulses is collected after the 2 pulse. To compensate for the small contribution Δ to the integrated signal, a reference measurement is performed without the 2 pulse and then detected counts are subtracted from the two-pulse measurement counts.

---

of spin-up to spin-down is then probed by a second 100 μs pulse after time τ by exciting the electrons in the Z_1 spin-down level and tracking the subsequent emission. This sequence is shown in Figure 5.7.

Given the spin relaxation time T_1 is on the same order of magnitude as the optical lifetime of the Y_1-Z_1 transition, we sample and subtract the emission triggered from the first optical pulse but collected in the collection window. To accomplish this, a reference measurement with only the first pulse is carried out for background subtraction, with a number of counts Δ removed (per Figure 5.7). The population recovery of spin-up to spin-down state is then identified as the difference in counts between the measurements with and without the first pulse as a function of the time delay τ between the first and second pulses.

CHAPTER 6

DEVELOPING ER-DOPED CERIUM DIOXIDE AS A QUANTUM MEMORY PLATFORM

This chapter is adapted with permission from Grant *et al.*[63] and Zhang *et al.*,[60] including text and figures from both works.

6.1 Selecting cerium dioxide as a host

While the selection of Er^{3+} as our qubit defect is secure, the particular choice of host for our Er^{3+} again depends on our use case. Different oxides may present longer T_1 times (e.g. Y_2O_3,[23]), guaranteed long coherence times under specific conditions (e.g. Y_2SiO_5[64]), maximal electron spin coherence (e.g. CeO_2), or straightforward nanofabrication on silicon(e.g. TiO_2). For this project we set out with the target of optimizing electron spin coherence.

Optimizing the electron spin coherence of Er^{3+} for quantum memory applications necessitates selection of an environment with minimal decoherence sources, and for high-quality wide-bandgap crystals at cryogenic temperatures the leading factor of decoherence is nearby nuclear spins within the host material.[31] A recent computational study identified that cerium dioxide (CeO_2) is an optimal host for maximizing electron spin coherence,[31] due to the near-zero natural abundance of nuclear spins in its constituent elements.[32] CeO_2 is additionally attractive as a host since its lattice constant (5.41 Å) is close to the lattice constant of Si (5.43 Å).[35] This leads to a low lattice mismatch of -0.4% when CeO_2 is epitaxially grown on Si substrates (irrespective of its orientation). Heteroepitaxy on silicon then provides an avenue for scalability and future integration with photonic and electronic quantum devices.

To study the viability of Er:CeO_2 for use as a telecom-wavelength interfaced spin qubit platform, we benchmark the spin and optical properties of Er-doped CeO_2 thin films grown on Si(111) by molecular beam epitaxy (MBE). Previous work on CeO_2/Si epitaxy has focused

mostly on microstructural studies.[65,66,67,68] Inaba *et al.*[50] have examined Er:CeO_2/Si down to 10,000 parts per million (ppm) Er and reported preliminary Er^{3+} optical characterization results at 4 K, including an optical excited state lifetime (T_1) of 1.5 ms at 1512 nm. We have focused on significantly lower Er concentrations (2-130 ppm) than have been studied previously in CeO_2. This regime is of interest for quantum applications since typically below 10 ppm the effects of inter-dopant dipolar interactions are reduced such that, taking into account only the Er dopants themselves, dephasing times – which are important for quantum applications – should primarily be limited by the radiative lifetime.[14]

Over the course of this chapter, we first conduct a detailed study of the MBE-grown Er:CeO_2(111) thin film on Si(111) system, starting with a microstructural study of the thin film where we confirm that CeO_2 grows epitaxially on the Si(111) substrate with appropriate Ce^{4+} valency. We then examine the spin properties of the Er doped into the CeO_2 system by electron paramagnetic resonance (EPR), where we identify results consistent with Er^{3+} substituting into the cubic Ce^{4+} site and observe a narrow EPR linewidth of 245(1) MHz at concentrations of 2-3 ppm.

Once Er incorporation is confirmed, we examine the optical properties of the trivalent Er^{3+} dopants at 3.5 K, and we identify an optical inhomogeneous linewidth of 9.5(2) GHz, a spectral diffusion linewidth as narrow as 4.8(3) MHz, and an optical lifetime as long as 3.5(1) ms at 2-3 ppm doping levels. Of particular note is that the spectral diffusion linewidths found here via transient spectral hole burning – though broader than in bulk or with nanostructures built upon bulk samples as measured by spectral hole burning[69] or photon echo[25,18,70] – are narrower by an order of magnitude than other reports of spectral diffusion in thin film or nanostructured Er-doped oxides on silicon.[20,21,22]

We make use of the narrow spectral diffusion linewidths at low doping levels (3 ppm) to explore explore the intrinsic optical coherence and electron spin coherence of Er^{3+} in CeO_2. Using two pulse photon-echo measurements, we demonstrate that the Er^{3+} ions have long-

lived optical states with a narrow homogeneous linewidth of $\sim$ 440 kHz and optical coherence of $\sim$ 0.72 μs at 3.6 K. Temperature-dependent data suggests that the homogeneous linewidth could be less than 200 kHz at milliKelvin temperatures with optical coherence times of $>$ 1.6 μs, indicating the potential of Er:CeO_2 as a usefully long optical quantum memory. Ideally, the reduced magnetic field noise from a low nuclear spin environment in the CeO_2 film also yields electron spin polarization with a slow spin-lattice relaxation, thereby enabling access to the electron spin dynamics even at 3.6 K, which is not observable in other well-studied host materials including Y_2SiO_5, YVO_4, and $CaWO_4$.[71,72,73]. We demonstrate here that Er^{3+} in CeO_2 show a spin coherence time $T_2 \sim 0.66\ \mu s$ at the isolated ion limit with a spin relaxation time of $T_1 \sim 1$ ms, indicating the potential for millisecond scale spin coherence.

To explore the impact of post-processing the Er:CeO_2 thin films, we also identify the trends by which the EPR, optical inhomogeneous, and spectral diffusion linewidths narrow and the excited state lifetime increases as a function of decreasing Er concentration. Examining Er:CeO_2 films annealed at up to 900 ℃, we find yields narrowing of the inhomogeneous linewidth by 20% and lengthening of the excited state lifetime by 40%.

6.2 Growing samples for Er:CeO_2/Si(111) studies

For these studies, we grew a selection of seven Er:CeO_2 thin film samples with Er concentration between 2 ppm and 130 ppm, each with a thickness much greater than necessary in similar systems to obtain diminishing returns in improving the optical linewidths.[20] The thicknesses of these films ranges from 740 nm to 940 nm, and are shown in Table 6.1. An additional sample was used for the annealing studies discussed in Section 6.7. This sample has an Er doping level of 3 ppm and a CeO_2 film thickness of 200 nm.

To produce these samples, we follow the MBE growth procedures laid out in Chapter 3 to grow Er:CeO_2 thin films on Si(111). For this growth campaign, Er and Ce were evaporated using resistively heated effusion cells (Riber HT-12), and ultra-high purity molecular oxygen

Er Doping Level (ppm)	2	3	14.5	15	50	90	130
CeO_2 Film Thickness (nm)	760	940	740	800	775	860	835

Table 6.1: Details on samples used in the Er:CeO_2 doping series

(O_2) was provided via an MKS mass flow controller. Beam equivalent fluxes of the Ce and O_2 were determined using a beam flux monitor to set a ratio of O_2 to Ce of $\sim$ 20 during growth, with growth rates of 250-360 nm/hr.†

6.3 Characterization of Er:CeO_2 microstructure

Microstructural characterization of the CeO_2 begins immediately subsequent to growth. Figure 6.1(a) shows the RHEED pattern of the surface of a 3 ppm Er, 940 nm thick CeO_2 film on Si(111) immediately following growth, with the electron beam incident along the Si$\langle 110 \rangle$ azimuth. No significant changes in RHEED patterns are noted during growth or for different Er doping concentrations. The streaky pattern indicates a smooth, single-crystalline surface and is consistent with an epitaxial CeO_2(111)/Si(111) alignment between the epilayer and substrate.

This is further confirmed by cross-sectional TEM (XTEM) studies. XTEM studies are carried using a Thermo Fisher Spectra 200 operated at 200 keV in scanning transmission electron microscopy (STEM) mode. The same beam conditions are used for energy-dispersive x-ray (EDX) spectroscopy. Figure 6.1(b) shows a representative high-resolution bright field XTEM image, with diffraction patterns shown in the inset. A 4 nm thick amorphous layer is observed at the CeO_2/Si interface. We identified a mixed CeO_x-SiO_y composition across this layer via EDX (Figure 6.1(c)). Similar interfacial oxide layers have been observed in CeO_2/Si previously[50] and are a well-known phenomenon in ionic oxides grown on Si,[23,74]

†. The O_2/Ce ratio is different here than what was discussed in Section 3.5 because the effusion cell for Ce was changed between the two growth campaigns, resulting in altered Er:CeO_2 growth window conditions. The ratio of $\sim$20 describes the identified growth window for the configuration used in this study.

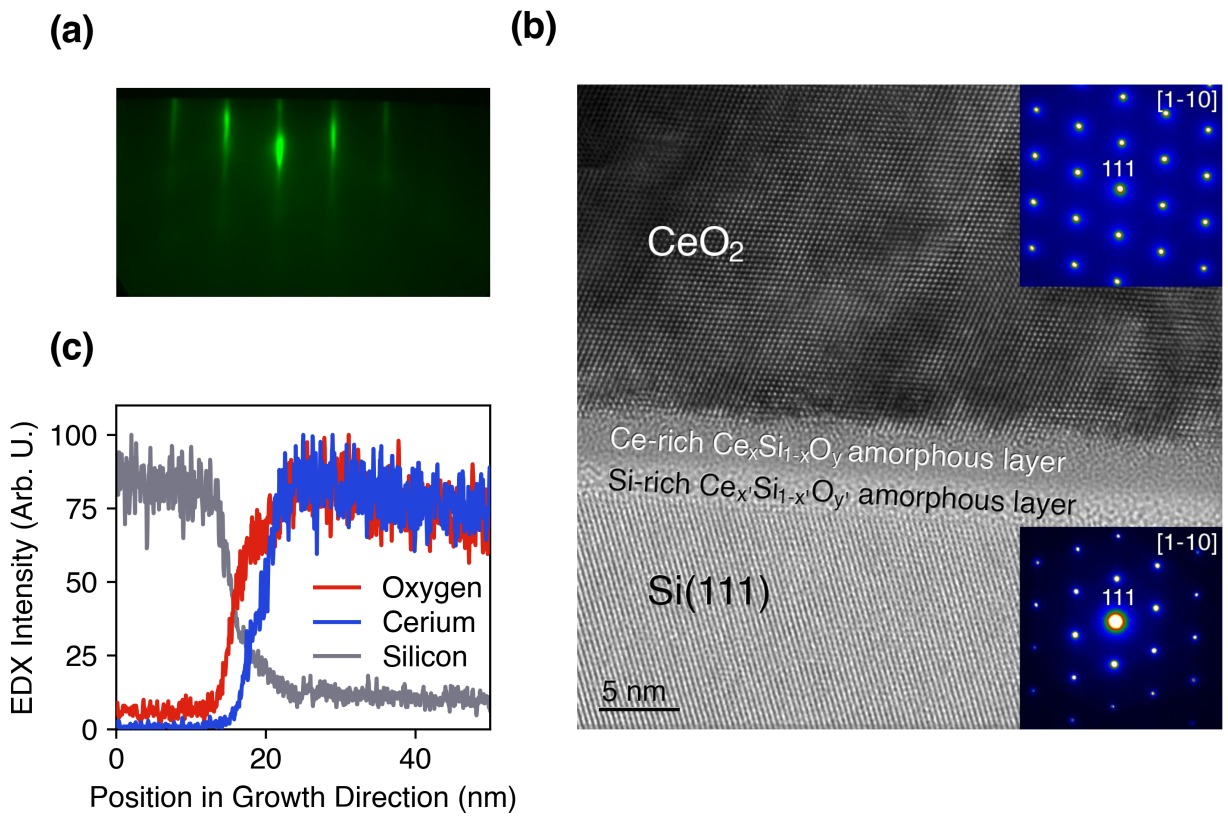

Figure 6.1: Epitaxy of a 3 ppm Er, 940 nm thick CeO_2 thin film on Si. (a) RHEED pattern of the as-grown epitaxial CeO_2 surface with the electron beam along the Si⟨110⟩ azimuthal direction. (b) High resolution XTEM of the Er:CeO_2/Si structure showing epitaxial registry of the CeO_2 with the Si substrate, as well as a 4 nm thick amorphous bilayer between the film and substrate. Diffraction patterns from the epilayer and substrate are shown in the insets. (c) EDX scan across the CeO_2/Si interface, showing that the amorphous bilayer is composed of a mixed Ce and Si oxide that is Ce and Si rich for the top and bottom layers respectively. Each intensity trace is normalized to the maximum counts for that element.

resulting from oxygen diffusion followed by catalytic oxidation of the buried silicon interface.

In addition to the amorphous bi-layer, low-magnification bright field XTEM (Figure 6.2) shows an epilayer threading dislocation density on the order of 10^9 cm^{-2}. Similar threading defects can be seen in the XTEM studies of CeO_2/Si by Inaba *et al.*[50] Threading segments do not relieve lattice mismatch strain, and we ascribe the formation of these threading defects to the initial stages of epitaxial growth of CeO_2, possibly due to the formation of localized patches of oxidized silicon due to catalytic effects of the deposited CeO_2.

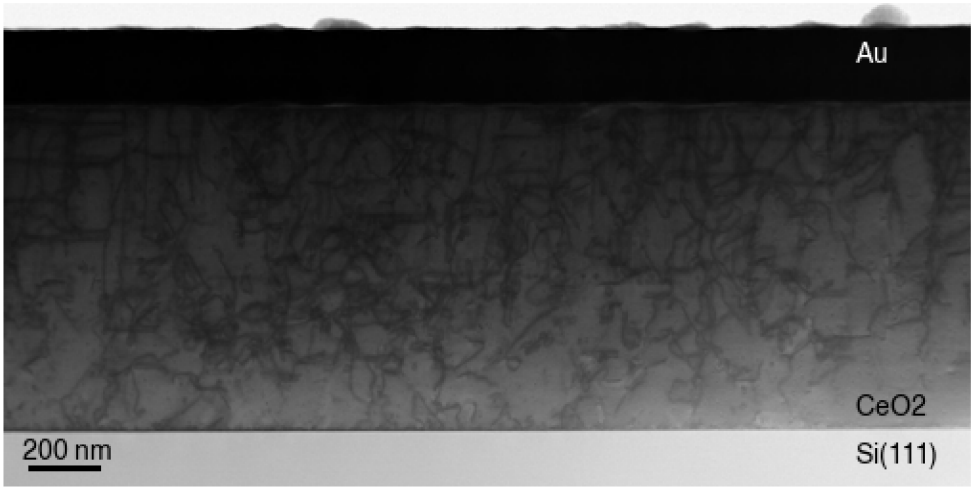

Figure 6.2: Low magnification bright field cross-sectional TEM of the full thickness of an as-grown Er:CeO_2 film (940 nm thick, 3 ppm erbium) on silicon, showing the presence of numerous threading dislocations, with an areal density of approximately 3.3×10^9 dislocations per cm^2.

An ω-2θ XRD scan of a 3 ppm Er, 940 nm thick CeO_2 sample, as shown in Figure 6.3(a), is carried out to further observe the as-grown crystal structure. The scan yields a CeO_2(111) peak with a full-width at half maximum (FWHM) of 630 arcsec, qualitatively consistent with the threading dislocation density observed. The peak separation between the Si(111) and CeO_2(111) peaks is ~700 arcsec indicating that most of the misfit strain remains elastically stored in the film.

To corroborate the crystal structure identified by XRD, XAS of the Ce M-edge on a 35 ppm Er, 240 nm thick CeO_2 on Si sample shows two sets of peaks related to the M5 and M4 transitions of electrons from 3d core orbitals to unoccupied p- and f-like symmetry orbitals, as seen in Figure 6.3(b). The positions of the main peaks at 883 eV (M5) and 901 eV (M4) relate to the electric-dipole allowed transitions to 4f states[75,76,77] and are consistent with the Ce^{4+} valence state and the formation of CeO_2 (as opposed to Ce^{3+} and Ce_2O_3). The satellite peaks at 889 eV (Y) and 906.5 (Y') result from transition to 4f states in the condition band and are additional indicators of predominately Ce^{4+} valency.[78,79] Overall,

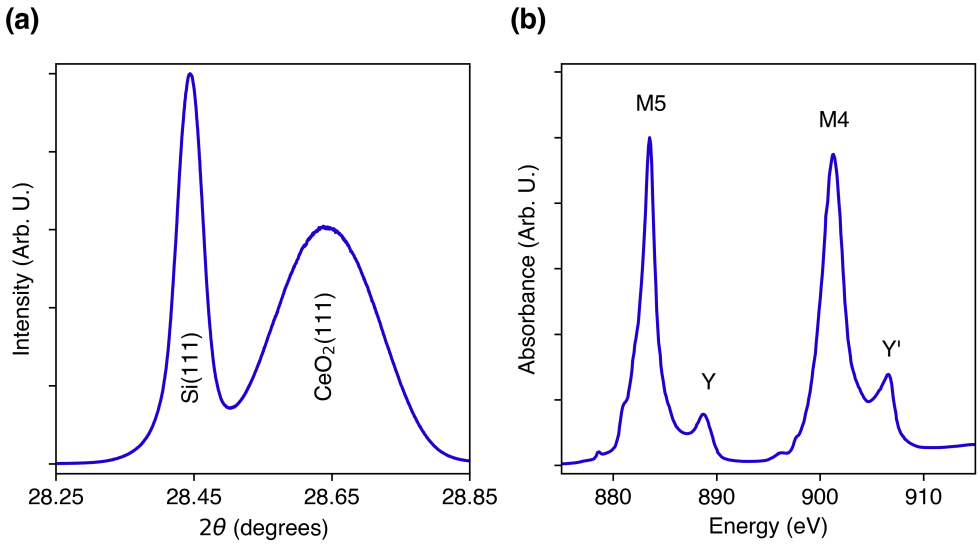

Figure 6.3: X-ray microstructural study of as-grown Er:CeO_2 samples. (a) ω-2θ XRD scan of a 3 ppm Er, 940 nm thick CeO_2 thin film on Si. The CeO_2 peak is located at 28.65°, with a FWHM of 630 arcsec. (b) X-ray absorption spectroscopy of a 35 ppm Er, 240 nm thick CeO_2 thin film on Si. The cerium M4 and M5 edges are shown, as detected by total electron yield (TEY) mode and normalized to the maximum measured intensity. Consistent with Ce^{4+}, the M5 and M4 peaks are at 883 eV and 901 eV respectively. The satellite peaks Y and Y' are observed at 889 eV and 906.5 eV respectively.

spectral shape and peak separation are consistent with the Ce^{4+} oxidation state, and peaks corresponding to Ce^{3+} are not identifiable within the spectrum. This data together with the XRD and XTEM studies suggests that we have a CeO_2 film where the Ce^{3+} concentration is likely less than 1%, beyond the detection limit of the experimental setup.

6.4 Characterization of the Er:CeO_2 spin system

We begin our analysis of the aggregate Er:CeO_2 system by looking at the embedded Er^{3+} electron spin spectrum. This gives us two vital pieces of information: first, the effective g-factor of the electron spin can confirm the placement of Er within the CeO_2 host matrix; second, the spin linewidth gives us a frame of reference regarding the degree to which defects, such as the threading dislocations identified in Section 6.3, may impact overall spin and

optical behavior within our thin films.

6.4.1 Extraction of g-factor, hyperfine coupling factor, and spin linewidth

As stated, the incorporation of Er^{3+} into the CeO_2 films is confirmed by identifying erbium-specific spin state splitting under EPR. We perform our spin characterization via low-temperature EPR, as described in Section 5.2. Low-temperature EPR probes the lowest-lying level of the $^4I_{15/2}$ manifold, where an effective spin-1/2 system is valid for identifying the features of the resultant spectra, per 2.1.3:†

$$H = \mu_B BgS + SAI \tag{6.1}$$

In the effective spin-1/2 Hamiltonian H (Eq. 6.1), the first term covers the Zeeman splitting of the electron spin states S proportional to the Bohr magneton μ_B, the applied magnetic field B, and the effective g-factor produced by local structure. The second term accounts for the hyperfine interaction between the electron spin S and the nuclear spin I for Er isotopes with a non-zero nuclear spin, governed by the hyperfine splitting tensor A.

Figure 6.4(a) shows a representative example of an EPR spectrum (blue dots) obtained from the 3 ppm Er, 940 nm thick CeO_2 sample. We identify a primary resonance peak near 100 mT surrounded by a set of lower-intensity resonance peaks. The primary peak arises from the absorption of the Er^{3+} electron spin transition for the 77% of naturally abundant nuclear spin $I = 0$ Er isotopes (primarily ^{166}Er, ^{168}Er, and ^{170}Er). The lower-intensity peaks arise from the hyperfine interaction between the electron spins and the remaining naturally abundant nuclear spin $I = 7/2$ isotope (^{167}Er), which yields eight hyperfine peaks. Seven hyperfine peaks are easily identifiable adjacent to the primary peak; the eighth hyperfine

†. Recall that this effective Hamiltonian includes a dramatic simplification of the hyperfine term in full rare-earth Hamiltonian in Section 2.1.3, to the formulation stated in Equation 2.18. This simplification is, however, allowed due to the fact that all spin states observed simultaneously with this technique are within the same J manifold of Er^{3+}.[37]

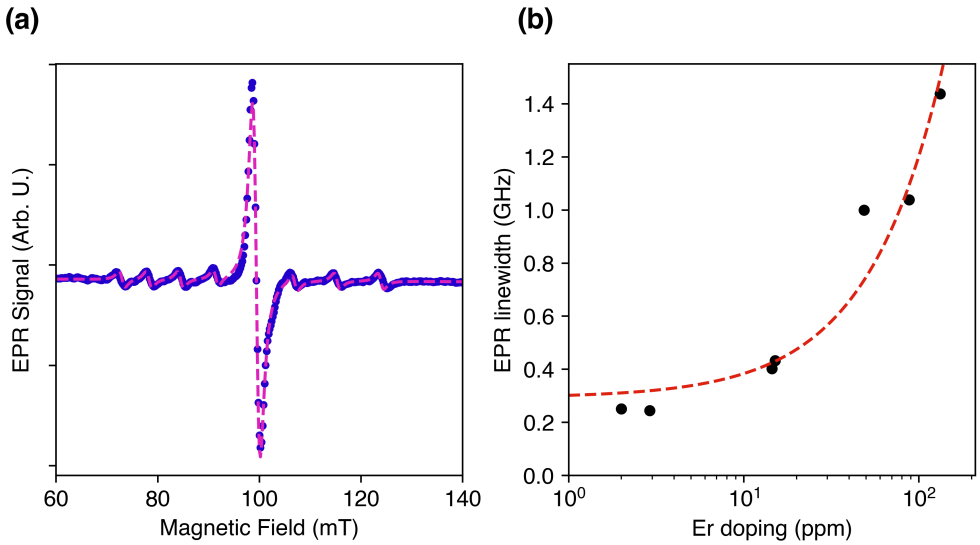

Figure 6.4: EPR study of Er:CeO_2 thin films on Si, with measurements are performed at 4.0-4.2 K. (a) CW EPR resonance spectrum of Er:CeO_2, obtained from a 3 ppm Er, 940 nm thick sample. A primary peak at $\sim$ 100 mT is produced by nuclear spin zero Er isotopes, and secondary peaks due to the less abundant ^{167}Er are visible around the main peak. Peak locations are fitted using Eq. 6.1 (magenta dashed line), and we obtain the g-factor $g = 6.812(5)$ and hyperfine splitting parameter $A = 687(1)$ MHz. (b) The Er spin resonance linewidth as a function of Er concentration, extracted from the primary peak of the CW EPR spectrum at each Er concentration (black dots). Uncertainties in the extracted linewidths are within the data marker size. A linear fit to the Er concentration (red dashed line) matches the trend of the data, and is discussed further in the main text.

peak is obscured by the primary peak.[80]

The measured EPR spectrum is fitted (Figure 6.4(a), magenta dashed line) to the energy structure defined by Eq. 6.1 to extract effective g-values, hyperfine parameters A, and EPR linewidths. Resonance peaks are described with first derivatives of Lorentzians, and the hyperfine peak locations are identified accounting for second-order perturbation in nuclear spin.[81] We extract an effective value $g = 6.812(5)$ and a hyperfine splitting of $A = 687(1)$ MHz for the displayed sample.

6.4.2 Placement of Er in the CeO_2 host matrix

The location of Er in the CeO_2 host matrix is an vital consideration – we want to make sure the Er is being placed consistently, but also we want to ensure that we have proper knowledge of the site symmetry in which the Er rests, so that when we look at the optical transition we know how many crystal field levels to expect, per Section 2.1.2.

Some studies in other trivalent metals doped into CeO_2 crystals indicate that above a certain critical doping level, the dopant can occupy interstitial sites in the CeO_2 matrix.[82] Fortunately for our purposes, this critical doping level is in the regime of several percent, and we are far below this – with at most ~ 100 ppm Er.

The g-factor of 6.812(5) for our Er:CeO_2 thin films is consistent with theoretical study of Er^{3+} residing in a cubic crystal field symmetry,[83] and is additionally consistent with experimental study of Er:CeO_2 in bulk and nanocrystal form.[83,84] Additionally, while CeO_2 has three Wyckoff sites with cubic symmetry, the comparable size of the Ce^{4+} and Er^{3+} ions (for coordination number 8, ionic radii of 0.97 Å and 1.004 Å respectively[85]) indicates that the Er ion is almost certainly substituting solely into the Ce site[86,87] under this growth method.

6.4.3 Comparison of spin linewidth to bulk values and spin-spin broadening

The broadening of resonance peaks in EPR may result from a variety of factors, including magnetic dipole-dipole interactions (e.g. Er-Er) and strain due to defects (e.g. threading dislocations, vacancies, unintentional dopants). Focusing on the nuclear spin zero peak, we find that the EPR linewidth increases linearly with Er^{3+} doping, as shown in Figure 6.4(b) for a series of Er:CeO_2/Si samples. A linear increase in linewidth with doping concentration may be associated with broadening due to magnetic dipole-dipole interactions between spins, but we find that broadening due solely to the concentration of Er^{3+} ions, $\Gamma_{\text{d-d}}$, calculated based on the Er concentration and measured g-factor,[61] would have the values $\Gamma_{\text{d-d}}(2 \text{ ppm Er}) =$

0.2 MHz and $\Gamma_{\text{d-d}}$(130 ppm Er) = 15.2 MHz. (The details of this calculation are discussed in Appendix B.)

Both of these $\Gamma_{\text{d-d}}$ values are significantly less than the observed linewidths from EPR measurement of those doping levels, of 245(1) MHz and 1450(25) MHz respectively. The reason for this discrepancy remains unclear, but suggests that there are other potential dopant-driven broadening mechanisms at play, plus a population of grown-in defects unrelated to the Er dopants. Fortunately, characterization of the optical transition will complement this study and yield additional insights as to these mechanisms.

6.5 Characterization of the Er:CeO_2 optical system

We continue our analysis of the Er:CeO_2 system by looking at the optical characteristics of the Er^{3+} $^4I_{15/2}$ to $^4I_{13/2}$ optical transition near wavelengths of $\lambda = 1.5$ μm.

6.5.1 Indexing of the crystal field levels

In the particular case of Er:CeO_2, we expect five crystal field levels each in the $^4I_{15/2}$ and $^4I_{13/2}$, per Table 2.1. Per the table, the cubic symmetry of the CeO_2 crystal field around the Ce site should result in $^4I_{15/2}$ and $^4I_{13/2}$ each splitting into five levels, which we label respectively as Z_1 to Z_5 and Y_1 to Y_5, in the order from the lowest to highest energy, as shown in Figure 6.5(a). Z_1 and Z_2 are two-fold degenerate states with effective spin $S = \frac{1}{2}$ – the manner of effective spin-1/2 system used to describe the EPR measurements – which transform into irreducible representations Γ_6 and Γ_7. The higher three Z levels (Z_3 to Z_5) are four-fold degenerate with effective spin $S = \frac{3}{2}$ and transform into irreducible representation Γ_8.

The crystal field split levels of Er^{3+} are probed through temperature and power dependent photoluminescence (PL) measurements with Er^{3+} ions excited by a 1473 nm laser, with photon energy higher than the $^4I_{13/2} \rightarrow ^4 I_{15/2}$ transition. Our spectrometer resolution of

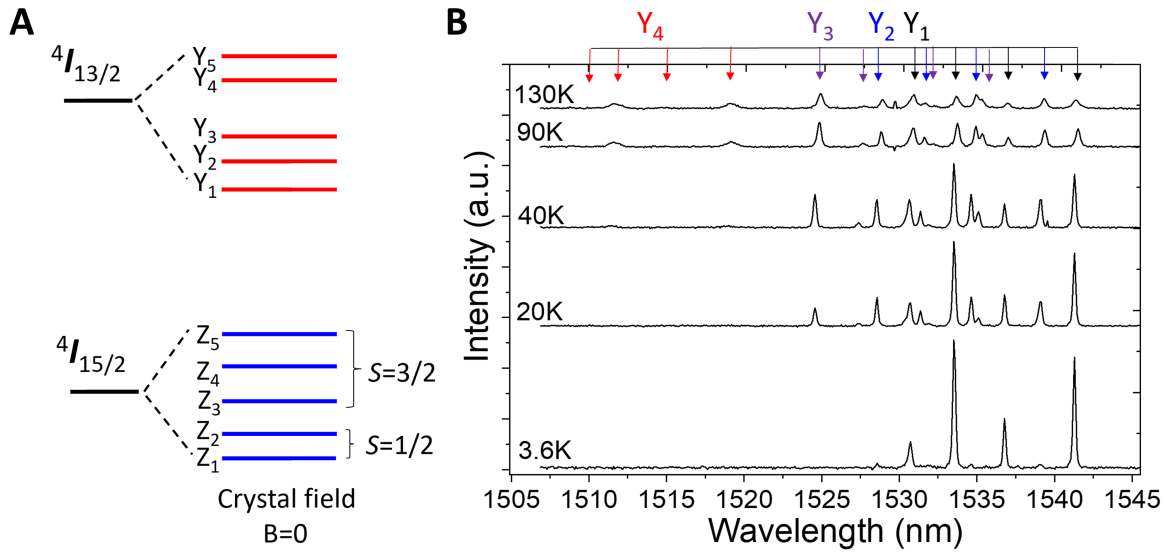

Figure 6.5: Crystal field split energy levels of the $^4I_{15/2}$ and $^4I_{13/2}$ multiplets of Er^{3+} ions in CeO_2. (a) Schematic of the crystal field splitting of the $^4I_{15/2}$ and $^4I_{13/2}$ multiplets, with 5 levels each, labeled as Z_1 to Z_5 and Y_1 to Y_5. (b) Temperature dependent PL spectra of Er^{3+} ion emission with Er^{3+} ion excited by a 1473 nm laser with excitation power of 1000 μW on the sample surface, 5 times the power needed to saturate $Y_1 - Z_j$ level transition.

---

20 GHz† is sufficient to resolve crystal field split transitions that are typically split by the hundreds of GHz to THz[14]. At 3.6 K, PL occurs primarily from Y_1 to all the Z levels due to the rapid non-radiative relaxation of electrons from higher Y levels to the Y_1 level.[88] Four emission peaks are observed in Figure 6.5(b) – These are identified to be Y_1 to $Z_1 - Z_4$ transitions as marked with black arrows. The lack of emission from the Z_5 level may be due to its small transition dipole moment. The higher Y levels are probed by altering the Boltzmann distribution of the electrons in the ensemble – increasing the sample temperature from 3.6 K to 150 K populates the higher Y levels once electrons are excited to $^4I_{13/2}$, as shown in Figure 6.5(b). Higher Y level transitions are thus identified based on their temperature dependent behavior and identified energy separation. With continued increase of temperature and as higher Y levels are populated, we clearly observe the Y_1 to Y_4 levels.

†. Alternatively, 0.16 nm or 84 μeV resolution.

Er^{3+} Level	Crystal Field Level	Level Energy (meV)	Transition Wavelength to Z_1 (nm)	Transition Wavelength to Y_1 (nm)
$^4I_{13/2}$	Y_5	Not observed	–	
	Y_4	821.741	1508.8	–
	Y_3	813.171	1524.7	–
	Y_2	811.097	1528.6	–
	Y_1	809.931	1530.7	–
$^4I_{15/2}$	Z_5	Not observed		–
	Z_4	5.517	–	1541.3
	Z_3	3.188	–	1536.8
	Z_2	1.479	–	1533.6
	Z_1	0	–	1530.7

Table 6.2: Crystal field levels of Er:CeO_2 identified by power and temperature-dependent PL measurements.

The intensity of emission from these identified Y_1 to Y_4 levels matches the expected behavior from a Boltzmann distribution of electrons at these temperatures.[60] Table 6.2 summarizes the energy structure of the Z_1 to Z_5 and Y_1 to Y_5.

The $Y_1 \rightarrow Z_1$ transition is found to be at 1530.74 nm (195.84 THz). For the remainder of this study, we focus on this transition as it allows for optical control of the effective $S = 1/2$ spin ground state, the Z_1 level. From here on, all studies on optical and spin properties are carried out at 3.6 K on the Z_1 and Y_1 levels, and – given the energy separation between the Z_1 and Z_2 implying only $\approx 0.8\%$ electron population of the Z_2 level due to Boltzmann statistics – we may treat the optical system as an effective two-level system involving only Z_1 level, ignoring the population of electrons at higher Z levels. (That said, for spin measurements, the population of the Z_2 level becomes more significant in the study of spin relaxation dynamics of the Z_1 level, as will be discussed later.)

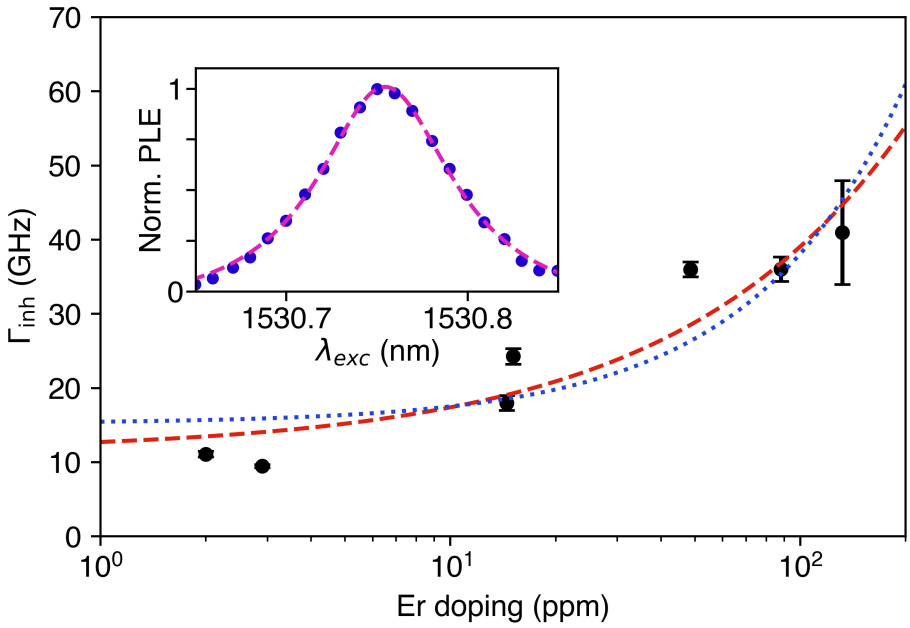

Figure 6.6: The inhomogeneous linewidth Γ_{inh} of the Er:CeO_2 Z_1-Y_1 transition as a function of Er doping concentration. Γ_{inh} varies with n_{Er} (black dots), where each point is the FWHM extracted from a PLE scan of the Z_1-Y_1 peak (inset, blue dots) via a Lorentzian fit (inset, magenta line). Fits with $\Gamma_{\text{inh}} \sim n_{\text{Er}}^{2/3}$ (red dashed line) and $\Gamma_{\text{inh}} \sim n_{\text{Er}}$ (blue dotted line) capture the general trend.

6.5.2 Analysis of trends against doping in optical characteristics

We then proceed to characterizing the optical interface presented by the Er:CeO_2 system. The Er^{3+} ground state $^4I_{15/2}$ (referred to as Z) and first excited state $^4I_{13/2}$ (referred to as Y) each split into five levels due to the cubic symmetry of the host CeO_2 structure,[36] which was confirmed by EPR.

For optical characterization, we focus on the Z_1-Y_1 transition due to its technological relevance at low temperature, with the readily accessible spin interface in Z_1 as discussed in the EPR section and the absence of the non-radiative processes found in $Y_{>1}$. We probe the Z_1-Y_1 transition with higher spectral resolution using PLE as a function of Er doping density, using the series of samples indicated in Table 6.1.

The inhomogeneous linewidth Γ_{inh} of the absorption line as shown in Figure 6.6 ranges

from 11.1(4) GHz at 2 ppm Er and 9.5(2) GHz at 3 ppm Er to 41(7) GHz at 130 ppm Er. This linewidth is influenced by the presence of electric fields caused by charged defects or strain in the vicinity of the optically active Er^{3+} sites. Such defects can include (1) other Er^{3+} ions since the aliovalent Er^{3+} on a Ce^{4+} site will result in a negatively charged point defect Er'_{Ce} (per Kröger-Vink notation[89]), (2) charge compensating defects such as positively charged oxygen vacancies,[86] and (3) "grown-in" imperfections during crystal growth. For a defect density n, one expects $\Gamma_{inh} \propto n^{2/3}$ for dipoles interacting with nearby charge defects and $\Gamma_{inh} \propto n$ for broadening due to strain, dipoles interacting with random electric field gradients, or dipole-dipole interactions.[90]

Taking $n \sim n_{Er}$, where n_{Er} is the concentration of Er'_{Ce} defects, we fit the two described cases to the Er-concentration dependent inhomogeneous linewidth. Both scenarios follow the generic trend of the data, with the $n^{2/3}$ dependence (Figure 6.6, dashed red line) yielding a slightly better fit than the linear case (Figure 6.6, dotted blue line). While the overall behavior is captured, we make no definite inference of the broadening defect's nature at this stage. In either case, we find ~ 10 GHz of residual inhomogeneous broadening even at low Er concentrations of 2-3 ppm, likely due to grown-in crystalline imperfections (see Appendix C for an extended discussion).

Continuing our optical study, we find that increasing the Er^{3+} concentration leads to a decrease of the optical excited state lifetime T_1, as shown in Figure 6.7 (black dots), from 3.5(1) ms at 2-3 ppm to ~ 2.7 ms at 130 ppm. These results are consistent with the presence of defects adding non-radiative or quenching pathways according to the Inokuti-Hirayama theory,[91] though the exact nature of these defects cannot be inferred at this time. (Additional details on this analysis are presented in Appendix C.) Concordantly, the longer millisecond-scale lifetimes of the Er optical transition (compared to other defect qubits such as vanadium in silicon carbide[92] or NV centers in diamond[93]) are a consequence of the forbidden ${}^4I_{15/2} - {}^4I_{13/2}$ transition.[14] However, our longest lifetimes at low doping are

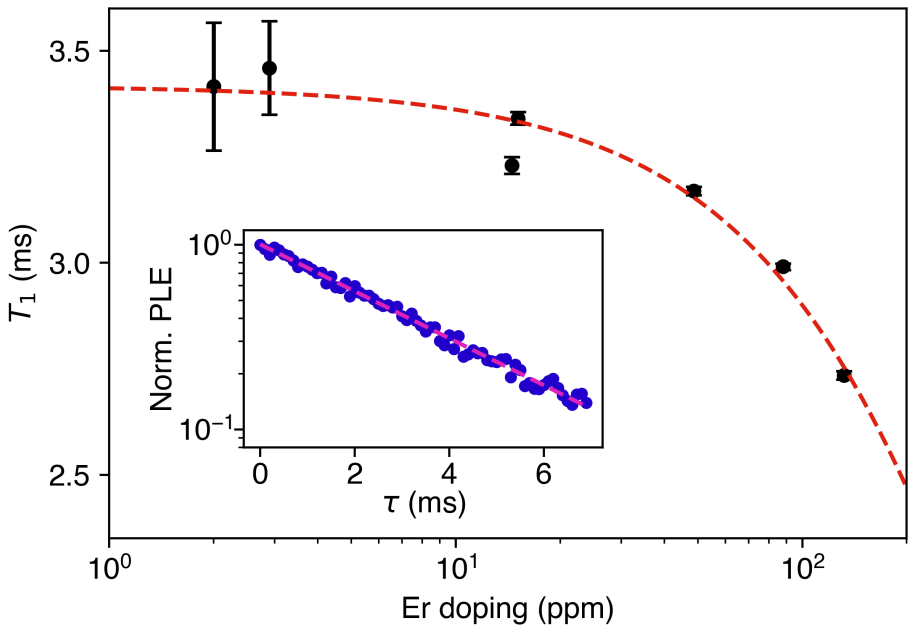

Figure 6.7: The optical excited state lifetime T_1 of the Er:CeO_2 Z_1-Y_1 transition as a function of Er doping concentration. The lifetime T_1 of the Z_1-Y_1 transition varies with the erbium concentration n_{Er} (black dots), where each point is the time constant taken from an optical decay signal (inset, blue dots) by an exponential fit (inset, magenta line). The dependence of T_1 on Er doping is fitted to the Inokuti-Hirayama model (red dashed line).

lower by a factor of $\sim$ 3 compared to the longest Er lifetimes reported in literature for doping in bulk host crystals grown from the melt under near-equilibrium conditions, such as in yttrium orthosilicate.[94,69] This is likely due to the higher defect densities and presence of proximal interfaces in our thin film materials grown under non-equilibrium conditions.

Finally, Figure 6.8 shows the dependence of the spectral diffusion-limited homogeneous linewidth Γ_{SD} as measured by transient spectral hole burning (TSHB), and henceforth referred to as the spectral diffusion linewidth Γ_{SD}, as a function of Er doping (black dots). The spectral diffusion linewidth scales linearly with Er concentration, from 4.8(3) MHz at 2 ppm to 1465(66) MHz at 130 ppm. (Details on the linear fit may be found in Appendix C.) This is consistent with instantaneous spectral diffusion from dipole-dipole interactions with nearby excited Er ions, which causes linear broadening in response to an increase in excited

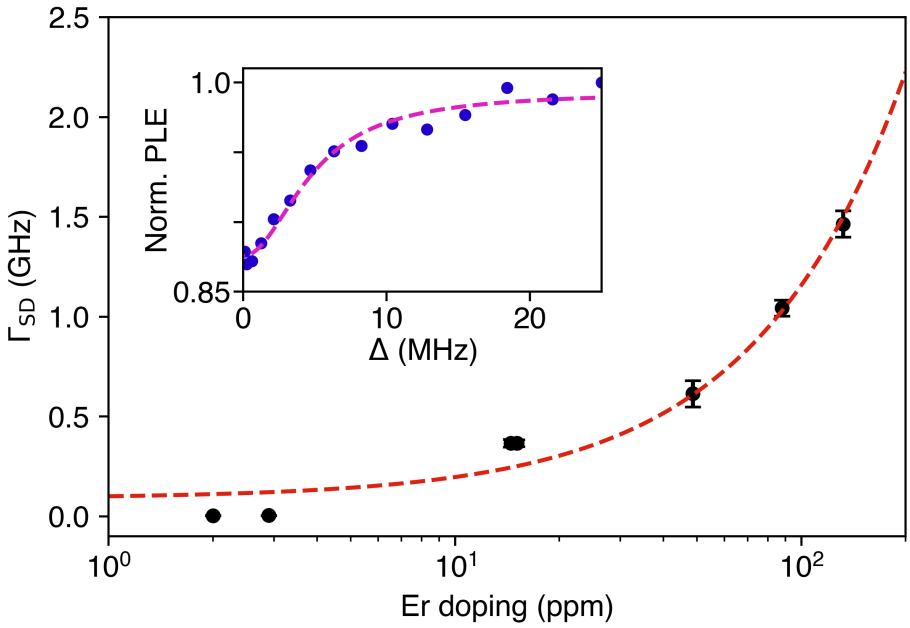

Figure 6.8: Spectral diffusion linewidth Γ_{SD} of the Z_1-Y_1 transition varies with the Er doping concentration n_{Er} (black dots), where each point is the half-width half-max extracted from a TSHB measurement (inset, blue dots) via a Lorentzian fit (inset, magenta curve). A linear fit (red line) follows the doping dependence trend.

---

ion density.[95] We emphasize this strong relationship between the doping density and spectral diffusion linewidth, with the data potentially suggesting lower linewidths at sub-ppm Er concentrations, particularly since at our examined lowest doping levels of 2-3 ppm we see spectral diffusion linewidths of ∼5 MHz for a millisecond-timescale TSHB measurement conducted at 3.5 K.

6.5.3 Measuring trivalent erbium optical coherence

As described in Section 5.1.4, photon echo provides a more sensitive method (compared to transient spectral holeburning) for finding the homogeneous linewidth Γ_{hom} of the optical transition, measured via the coherence time related by $\Gamma_{\mathrm{hom}} = 1/\pi T_2$.[96] Having measured the inhomogeneous profile of the Z_1 - Y_1 transition and finding the transition wavelength to be centered on 1530.74 nm, we may bring our laser on-resonant with the transition and

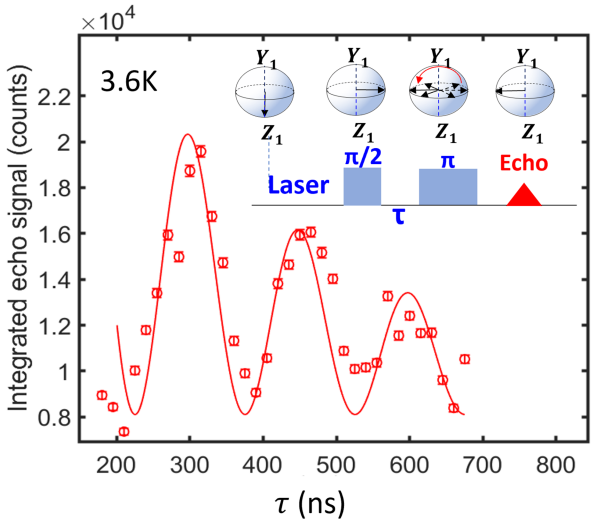

Figure 6.9: Optical coherence measurement of the Er:CeO_2 Y_1-Z_1 transition, showing two-pulse photon echo decay for the transition with the pulse sequence shown in the inset. Data is shown as open circles. The solid line is the fit to the data, indicating optical coherence of $T_2 = 720.0 \pm 33.1$ ns, or a homogeneous linewidth of $\Gamma_{\text{hom}} = 442.1 \pm 20.3$ kHz. The observed beating pattern is of the period $T_{\text{osc}} = 300.2 \pm 11.8$ ns ($f_{\text{osc}} = 3.33 \pm 0.23$ MHz).

perform photon echo on the Z_1-Y_1 transition to obtain its homogeneous linewidth.

Figure 6.9 shows the measured integrated echo intensity as a function of τ at 3.6 K using the pulse sequence schematically shown in the inset. The data show a single exponential decay envelope of the photon echo amplitude modulated by an oscillating beat pattern. The beating pattern indicates that we are coherently addressing of a superposition of two transitions in a three-level system where the energy separation of two of the levels is within the bandwidth of the optical pulse. The red line is a fit to the data considering a single exponential decay with an added frequency of oscillation $f = 1/T_{\text{osc}}$. The fit yields an optical coherence $T_2 = 720.0 \pm 33.1$ ns, or rather a homogeneous linewidth $\Gamma_{\text{hom}} = 442.1 \pm 20.3$ kHz; the beating period is $T_{\text{osc}} = 300.2 \pm 11.8$ ns (or rather, has a frequency of $f_{\text{osc}} = 3.33 \pm 0.23$ MHz). The observed beating frequency is indeed within the bandwidth of the optical pulse, and is also found to be consistent with the Zeeman splitting of the Z_1 level due to Earth's magnetic field at around 0.35 G. This suggests that the beating could be due to the Earth's

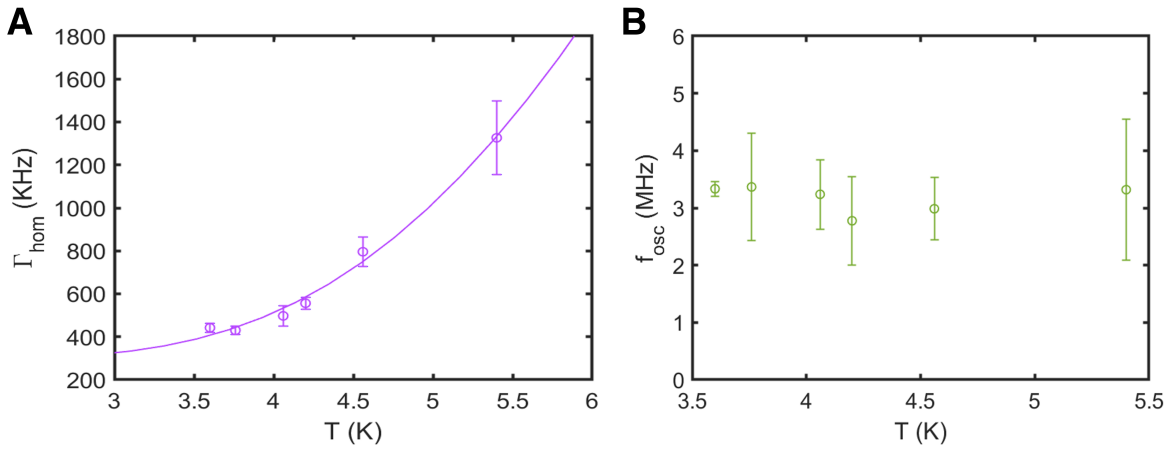

Figure 6.10: Optical coherence measurement of the Er:CeO_2 Y_1-Z_1 transition as a function of temperature, with (a) showing Γ_{hom} as measured by two-pulse photon echo (with data shown as open circles). The solid line is the fit to the data using Equation 6.2. (b) The extracted beating frequencies f_{osc} (open circles) from two-pulse photon echo measurement as a function of temperature, with no consistent variation with temperature.

---

magnetic field very slightly lifting the degeneracy of the Z_1 level.

The observed homogeneous linewidth of $\Gamma_{\text{hom}} = 442.1 \pm 20.3$ kHz at 3.6 K is orders of magnitude higher than the lifetime-limited $\Gamma_{\text{hom}} \sim 94$ Hz that ought to result from the the ~3.4 ms radiative lifetime of the Y_1-Z_1 transition. To probe dephasing processes that might be contributing to this broadening, we perform temperature-dependent measurements of Γ_{hom} via photon echo using two pulse PE to gain insights into the dephasing mechanisms occurring in the material, with temperatures ranging from 3.6 K to 5.5 K. Figure 6.10(a) shows the extracted Γ_{hom} as a function of temperature. The beat frequency extracted from all temperatures is shown in Figure 6.10(b) – the beat frequency is independent of temperature, which is consistent with its origin being from the Zeeman splitting of the Z_1 level induced by the earth's magnetic field.

At these measured temperatures, two phonon processes contribute to dephasing: (a) coupling to two-level systems (TLS)[97,98,99] (b) Orbach process phonon effects.[100,101] A homogeneous linewidth $\Gamma_{\text{hom}}(T)$ of the following form is then developed, invoking the linewidth at zero temperature Γ_0, the TLS coupling coefficient α_{TLS}, the phonon coupling coefficient

α_{phonon}, and the Boltzmann constant k_B:

$$\Gamma_{\text{hom}}(T) = \Gamma_0 + \alpha_{\text{TLS}} T + \alpha_{\text{phonon}} \exp\{-\Delta E / k_B T\} \tag{6.2}$$

In the examined temperature range, the increase in Γ_{hom} is dominated by Orbach relaxation. The solid line is the fit to the data using Equation 6.2, finding $\Delta E = 2.05$ meV. The extracted ΔE is consistent with the energy separation between the Z_1 to Z_2 level obtained from PL measurements. Of the total linewidth broadening, $\sim$ 150 kHz is due an Orbach process at 3.6 K with the remaining 300 kHz of broadening coming from the combined contribution of Γ_0 and direct phonon coupling, $\alpha_{\text{phonon}} \cdot T$. The α_{phonon} constant is typically in the range of a few to tens of kHz/K [102,103,100] for rare-earth ions in oxides. One can thus deduce that Γ_0 is most likely $\leq$ 200 kHz. This suggests that the dominant dephasing process might be from spectral diffusion due to ion-ion dipolar interactions given the short ensemble average Er-Er separation in the sample ($\sim$14 nm, estimated from the Er concentration) or a fluctuating field induced by background charge, defects, or strain in the film.

It is worth noting that the sample studied here is grown without any optimization. One could further improve the homogeneous linewidth by optimizing growth to reduce strain and minimize defects. There is also the path of reducing the concentration of Er^{3+} to minimize ion-ion dipolar interaction-induced spectral diffusion. Besides this, one could also improve the homogeneous linewidth by applying moderate magnetic fields to reduce the coupling of TLS to the dipole moment of Er^{3+}. [104,100] The field can also freeze Er spin flip processes, reducing fluctuating magnetic field-induced spectral diffusion and thus extending optical coherence.

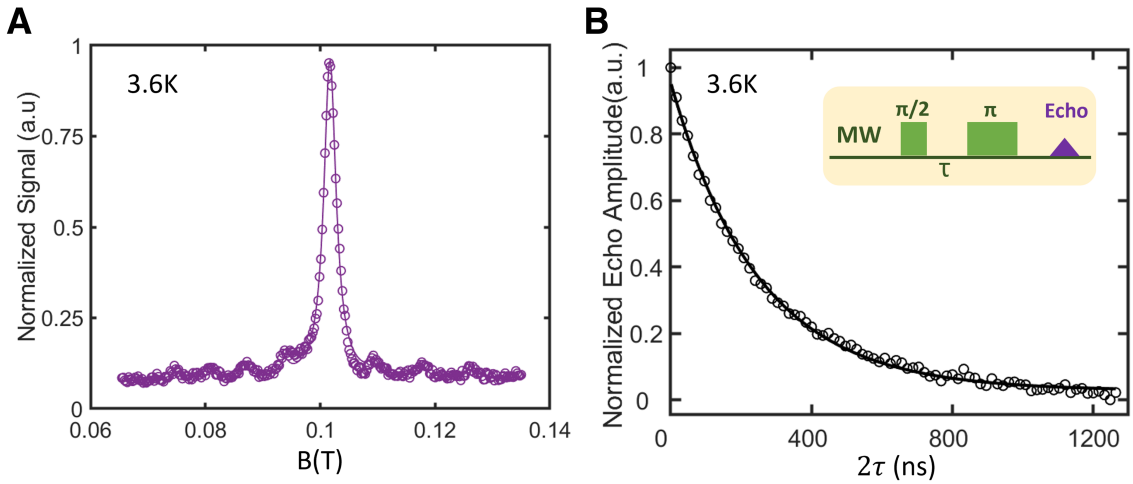

Figure 6.11: Electron spin coherence at 3.6 K probed by pulsed EPR with microwave drive at 9.7 GHz. (a) Resulting EPR spectrum from two-pulse echo as the magnetic field B is swept. Data (open circles) is taken using the Hahn echo sequence schematically shown in panel (b) with a fixed delay time of $\tau = 100$ ns. (b) Spin echo measurement using two-pulse Hahn echo sequence schematically shown in the inset. Data (open circles) are taken as a function of time delay τ between the 12ns $\pi/2$ pulse and 24ns π pulse. The solid black line is a single exponential fit revealing the spin coherence time $T_2 = 0.249 \pm 0.035$ μs.

6.6 Characterization of Er:CeO_2 spin system

Having evaluated the optical structure and coherence, we now continue our study of the Er:CeO_2 system by looking at the properties of the Zeeman-split spin levels within the Z_1 level.

6.6.1 Measuring trivalent erbium electron spin coherence

In order to use Er^{3+} as a spin-photon interface for quantum memory applications, the Er^{3+} electron spin coherence is a vital figure of merit. Here we study the electron spin behavior using an X-band (9.7 GHz) pulsed electron paramagnetic resonance (EPR) spectrometer to study spin coherence and relaxation. Figure 6.11(a) shows the measured spin echo response as a function of the static magnetic field applied during measurement. The data is obtained with the τ delay between the $\pi/2$ (12 ns) and π (24 ns) pulses set to 100 ns. The resulting spectrum

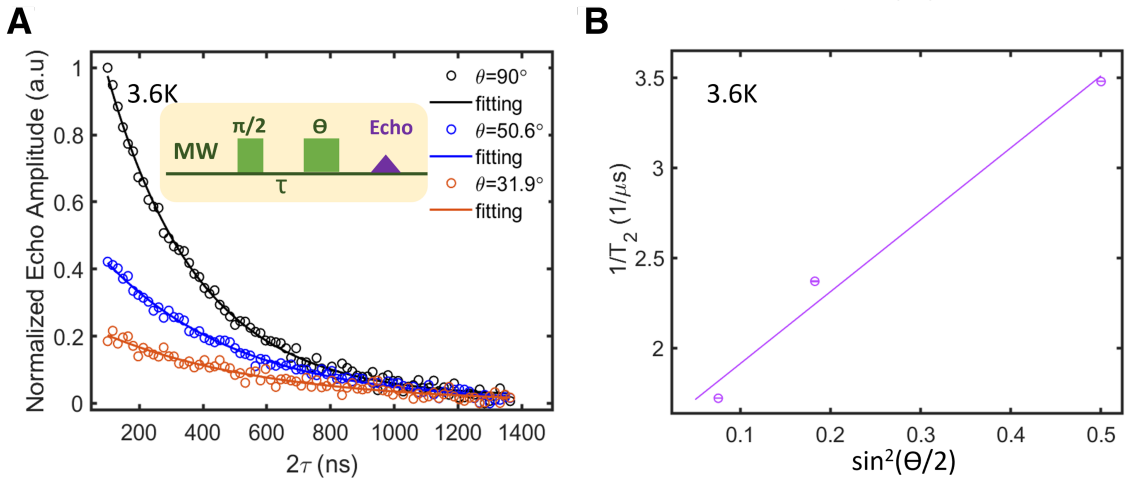

Figure 6.12: Electron spin coherence at 3.6 K probed by pulsed EPR with microwave drive at 9.7 GHz. (a) Generalized Hahn echo measurements on Er^{3+} electron spins taken with three different flip angles θ of the second rotation pulse. Solid lines are the single exponential fits to the data. (b) Plot of the inverse of spin coherence time T_2, extracted from the fits to the data in panel (a) as a function of averaged inversion pulse fidelity $< \sin^2(\theta/2) >$. A linear fit to the data (solid line) yields the spin coherence at single isolated ion limits to be $T_2 = 0.660$ μs and a spin concentration of 5.66 ± 0.25 ppm in the sample.

shows the expected resonance from nuclear-spin-zero even isotopes $^{166}Er^{3+}$ (primary peak) along with the hyperfine resonances containing the $^{167}Er^{3+}$ with nuclear spin $I = \frac{7}{2}$ (smaller secondary peaks). As in CW EPR, seven of the eight hyperfine peaks are clearly resolved, and one of the hyperfine resonance is obscured by the primary resonance peak at $B_0 = 0.102$ T. The measured spectrum is fit using the effective Hamiltonian shown in Equation 2.18, accounting for the second-order perturbation effects from the large nuclear spin of $^{167}Er^{3+}$. The extracted g-factor is value is $g = 6.828(5)$, consistent with the CW EPR spectrum shown in Figure 6.4(a).

The Er^{3+} spin coherence time, T_2, is then probed via Hahn echo measurement. The magnetic field is tuned to $B = 0.102$ T, where resonance with the primary Er^{3+} peak is identified per Figure 6.11(a) with the applied 9.7 GHz microwave frequency.† Figure 6.11(b)

†. Regarding the shrouded hyperfine resonance peak, we note that the echo signal is predominantly from the ^{166}Er electrons with only 3.6% of the signal from the ^{167}Er electrons.

shows the measured spin echo signal collected as a function of the delay (τ) between the $\pi/2$- and the π-pulse at 3.6 K. By fitting the echo amplitude decay to as $I(\tau) \propto \exp\{-2\tau/T_2\}$ (black curve in Figure 6.11 (b)), we obtains $T_2 = 0.249 \pm 0.035$ μs.

Spin coherence times are typically limited by the phonon-induced dephasing caused by elevated temperatures, and by Er-Er spin dipolar interactions. Er-Er dipolar interactions cause shifts in the spin resonance, and spectral diffusion occurs because of the random spin orientation resulting from spin-lattice interactions or spin diffusion. The dipolar interaction between spins magnifies itself in the spin echo decay through so-called instantaneous diffusion[105,106]. The spin coherence can be written as $1/T_2 = 1/T_{2,\mathrm{INST}} + 1/T_{2,\mathrm{bath}}$ where $T_{2,\mathrm{INST}}$ represents the contribution from instantaneous diffusion. To understand the dominant dephasing mechanics, we carry out instantaneous diffusion measurements[105] to probe and decouple the Er-Er spin dipolar interactions. A generalized echo sequence $(\pi/2 - \tau - \theta)$ is performed on Er spins where the angle of the second pulse θ – and hence the fidelity – of the second inversion pulse is varied.[105,106] The second pulse inhibits the decoupling of the probed spins' mutual dipolar interactions, resulting in decoherence through instantaneous diffusion. The echo signal (SE) is thus proportional to the exponential of the averaged inversion pulse fidelity $\langle \sin^2(\theta/2) \rangle$ and is given by Salikhov *et al.*[105] as follows, for an ensemble of spins with density ρ, a g-factor of g, the Bohr magneton β:†

$$\mathrm{SE}(\tau) \propto \exp\left\{ \frac{8\pi^2}{9\sqrt{3}} \frac{g^2\beta^2}{\hbar} \rho \sin^2(\theta/2)\tau \right\} \tag{6.3}$$

Thus, $T_{2,\mathrm{INST}}$ is proportional to $\langle \sin^2(\theta/2) \rangle$ and we obtain the following equation for T_2:

$$\frac{1}{T_2} = \frac{1}{T_{2,\mathrm{INST}}} + \frac{1}{T_{2,\mathrm{bath}}} = \frac{8\pi^2}{9\sqrt{3}} \frac{g^2\beta^2}{\hbar} \rho \sin^2(\theta/2) + \frac{1}{T_{2,\mathrm{bath}}} \tag{6.4}$$

†. As a point of note, this equation includes in its exponential same form of the spin-spin dipolar interaction term that arose when discussing EPR resonance broadening. See Appendix B for additional discussion of this interaction.

For the instantaneous diffusion measurements, the angle of the second rotation pulse θ is varied by tuning the power of the microwave pulse,[60] while keeping the pulse length unchanged, such that the same ensemble of spins within the second pulse. Figure 6.12(a) shows the measured echo intensity as a function of τ with three different rotation angles θ. A reduction of rotation angle θ reduces spin flips induced by the microwave pulse, and hence reduces instantaneous diffusion. Reducing instantaneous diffusion in this manner increases Er spin T_2 from 0.25 μs to 0.58 μs. The inverse of the extracted T_2 obtained through the single exponential fit is shown in Figure 6.12(b). Following Equation 6.4, the slope of the linear fit to the data in Figure 6.12(b) yields the density of probed Er spins to be $(1.66 \pm 0.08) \times 10^{22}$ $\#/\mathrm{m}^3$, or 0.68 ± 0.03 ppm in the context of the CeO_2 host matrix.

We may use this technique to confirm the overall concentration of Er by taking into account the fraction of the entire Er ensemble probed by the measurement. The linewidth of the Er spin resonance for this sample is 244.9 ± 2.9 MHz per Figure 6.4, $\sim$8.3 times larger than the bandwidth of the θ rotation pulse. This indicates that only 12% of the spins within the inhomogeneous distribution are probed. Therefore, the estimated total concentration of the Er spin is 5.66 ± 0.25 ppm, within a factor of 2 of the Er concentration estimated from Er flux used during MBE growth.

The intercept of the linear fit additionally provides an estimate on the spin coherence at the single isolated ion limit: $T_2 = T_{2,\mathrm{bath}} = 0.660 \pm 0.004$ μs in the single-ion limit. From this, we can conclude the measured T_2 in Figure 6.11(b) is largely limited by the Er-Er spin dipolar interaction-induced instantaneous diffusion, and could thus be improved by a reduction of Er concentration. With the generalized echo sequence reducing instantaneous diffusion, the spin homogeneity $\Gamma_\mathrm{h} = 1/\pi T_2$ contributed by the bath is 484.8 ± 20.6 kHz. This deduced spin coherence $T_{2,\mathrm{bath}}$ at the single isolated ion limit is then probably limited by the phonon-induced dephasing and spectral diffusion induced by interaction with other defects in the film.

6.6.2 Measuring trivalent erbium electron spin relaxation

The limit on spin coherence is set by the spin relaxation. We can probe the spin relaxation mechanism in two ways to obtain an upper limit on the spin T_2.

The spin relaxation time is probed in the context of pulsed EPR by first applying a π-pulse to invert the population of spin states, and then reading out the relaxation via a two-pulse Hahn echo sequence after a delay time τ. This pulse sequence is shown in Figure 6.13(a), and by varying the delay time τ between the initial inversion pulse and the Hahn echo sequence, the echo intensity resulting from the Hahn echo sequence will change. The measured spin echo signal is shown as a function of τ at 3.6 K, and we identify two spin relaxation processes: one with a short spin relaxation of $T_1 = 0.11 \pm 0.01$ ms, and another with a long spin relaxation of $T_1 = 0.83 \pm 0.04$ ms. The two observed decay processes may arise from the electron depopulation of the Z_1 spin level to its nearby Z_2 level, resulting in a sampling of electron population between three active states – a situation to which EPR is quite sensitive. At 3.6 K, there is thermal population of both Z_1 and Z_2 levels given the small energy separation of 1.51 meV (357.5 GHz). The added Zeeman splitting further aids in reducing the energy barrier between Z_1 spin-up and Z_2 spin-down levels. Possible depopulation of Z_1 spin-up level to the Z_2 spin levels, mediated by phonon processes, can thus be detected by pulsed EPR.

To further probe the origin of the observed double exponential decay dynamics, we carry out optical measurements of the spin relaxation T_1 of the Z_1 level at 3.6 K. We apply a 100 mT magnetic field parallel to the $\langle 1\bar{1}0 \rangle$ crystal direction, with orientation chosen to be the same as that used in the pulsed EPR measurements. A Zeeman splitting of 9.46 GHz between the spin-up and spin-down state of the Z_1 level is induced, per the effective g-factor from the CW EPR measurements. Given that the spin T_1 is shorter than the optical lifetime of the Y_1-Z_1 transition, the optical measurement of spin T_1 cannot be done using typical spectral hole-burning methods,[107,108] where one fully polarizes the spins through

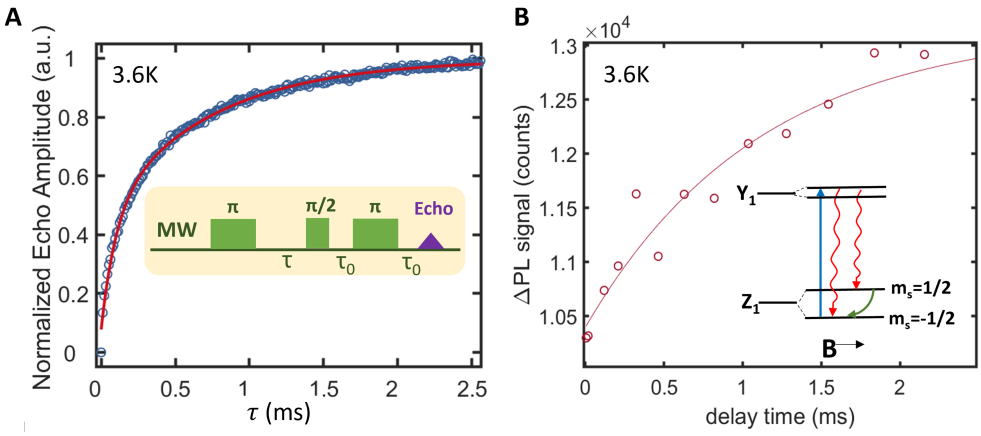

Figure 6.13: Electron spin relaxation dynamics at 3.6 K (a) Pulsed EPR Hahn echo measurement with a three-pulse population inversion sequence shown in the inset. Data are shown as open circles and the solid line is a double exponential fit revealing two spin relaxation paths with a short spin relaxation $T_1 = 0.11 \pm 0.01$ ms and a long spin relaxation $T_1 = 0.83 \pm 0.04$ ms. (b) Optical measurement of Z_1 level spin relaxation using two optical pulses using 'pump and probe' scheme. For this process, a 100 μs pulse is applied first, followed with a second 100 μs pulse separated by the delay time. PL signal is collected with a 4 ms collection window across 15,000 iterations of measurements. The measured PL signal difference with and without the second probe optical pulse is shown as a function of the delay between pulses (ΔPL, open circles). Data are taken with laser resonant to the spin-down Z_1 to spin-up Y_1 level transition (inset).

---

the cumulative optical excitation processes. Here we use a two pulse optical 'pump-probe' scheme to probe the spin relaxation from spin-up to spin-down state. We first apply a short 100 μs optical pulse resonant to the transition between Z_1 spin-down state and the Y_1 spin-up state (inset of Figure 6.13(b)) to drive the electrons occupying spin-down states to the excited state, creating an initial state occupation where the population of the Z_1 spin-up state is higher than that of spin-down. A second pulse of 100 μs is applied after a delay time τ to probe the recovery of the spin-down state occupation due to spin relaxation. A reference measurement without the second excitation pulse is taken to sample the photon emission during the collection window due to optical decay of the Y_1 level to both spin states after the first optical pulse – this is treated as background signal and subtracted.

The spin recovery from spin-up to spin-down through spin relaxation is evidenced by

the increasing ΔPL with increasing delay time in Figure 6.13(b). The data shows a single exponential decay (fitting, solid line) indicating a spin relaxation time for the Zeeman split Z_1 spin-up to spin-down state of $T_1 = 1.106 \pm 0.256$ ms. The measured T_1 value is consistent with the long T_1 resolved in the pulsed EPR shown in Figure 6.13(a). The single exponential decay identified in the optical measurement of the Z_1 spin relaxation also suggests that the short 0.11 ms relaxation process observed in pulsed EPR measurement is likely coming from the phonon mediated depopulation of electrons from Z_1 spin-up level to Z_2 level.

6.7 Effect of annealing on Er:CeO_2 optical parameters

Though we largely are careful not to assume the nature of the defects (other than Er) leading to broadening and decoherence processes over the course of our Er:CeO_2 study, we have speculated that these defects may be partially mitigated by post-growth annealing. For example, oxygen vacancy-related defects can result from non-equilibrium growth processes such as in MBE, and may be removed by annealing.

To study the effect of annealing, we anneal a 200 nm thick, 3 ppm Er:CeO_2 film on Si for 12 hours in 1 atmosphere of 20% O_2/Ar at different temperatures from 300 ℃ to 1000 ℃ using an MTI OTF-1200X tube furnace. The film roughened substantially at 1000 ℃, so we constrain our discussion to a maximum annealing temperature of 900 ℃ where the physical integrity of the samples remains intact. Figure 6.14 shows the dependencies of the measured inhomogeneous linewidth, excited state lifetime, and spectral diffusion linewidth of the Z_1-Y_1 transition as a function of the annealing temperature between 300 ℃ and 900 ℃. Annealing in this range leads to improvements in Γ_{inh} and T_1 of 20% and 40% respectively from their as-grown values. We ascribe these improvements to the annealing out of “grown-in" crystal defects in the thin films. However, the spectral diffusion linewidth worsens at moderate temperatures and returns to the as-grown linewidth at the maximum temperature studied, and the process driving this behavior is unclear.

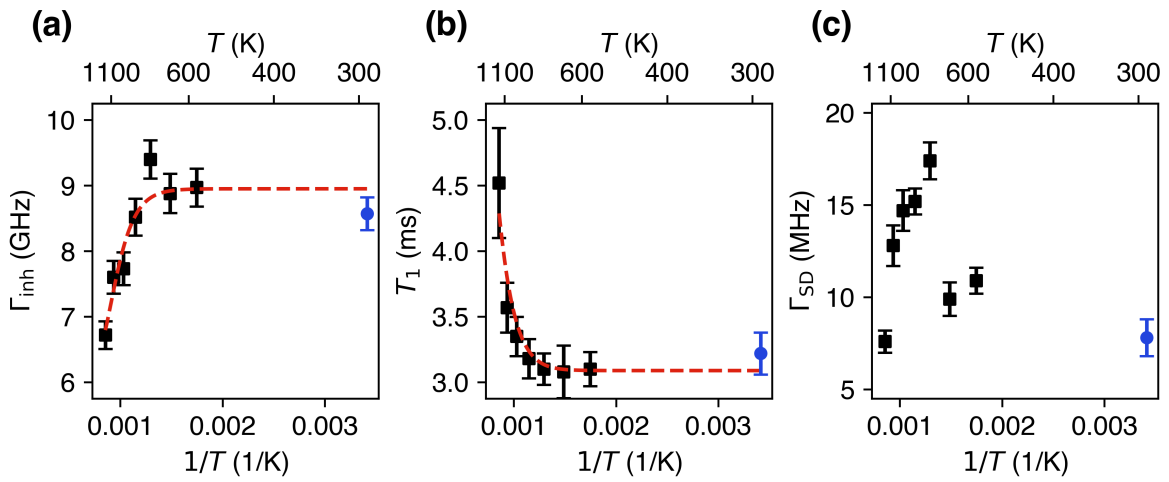

Figure 6.14: Annealing study of a 3 ppm Er, 200 nm thick CeO_2 thin film on Si via 12-hour anneals in O_2/Ar at 1 atmosphere as a function of annealing temperature T. Optical measurements are performed at 3.5 K for all samples. Black squares indicate annealed samples, blue dots indicate the un-annealed as-grown sample as the built-in reference. Kinetic model extensions to the inhomogeneous linewidth and optical lifetime models (red dashed curves) are described in the text. (a) Inhomogeneous linewidths before and after annealing. (b) Optical lifetime of the Z_1-Y_1 transition before and after annealing. (c) Spectral diffusion linewidth of the Z_1-Y_1 transition before and after annealing.

The trends in inhomogeneous linewidth Γ_{inh} and the excited state lifetime (T_1) as a function of annealing temperature (T) can be captured by assuming (i) a first-order reaction rate-limited process of thermally activated annihilation of the grown-in defects that affect the optical properties, and (ii) the suitability of the previously described power law relation and the Inokuti-Hirayama approach respectively for the defect concentration dependence upon Γ_{inh} and T_1. Details extending these models for annealing are given in the Appendix C. We find that an Arrhenius-like activation energy E_A in the range of $0.65 - 0.75$ eV for the temperature-dependent first-order reaction rate constant leads to good fits for both Γ_{inh} (Figure 6.14(a), red dashed line) and T_1 (Figure 6.14(b), red dashed line). This points to a density of grown-in, optically relevant defects that are being annihilated via thermally activated processes.

The question then is the nature of the defect being manipulated during annealing and

thus leading to the improvement of the inhomogeneous linewidth and excited state lifetime. Positively charged oxygen vacancies ($V_O^{\bullet\bullet}$) are a well-known defect in CeO_2, whose concentration can be increased by substituting aliovalent dopants (such as Er^{3+}) into Ce^{4+} sites[109,110] (Er'_{Ce}). Charge neutrality in the film is maintained by $2[Er'_{Ce}] = [V_O^{\bullet\bullet}]$, where brackets indicate concentration. The oxygen vacancies may affect the Er luminescence via strain or electric field interactions, whose strength would depend upon the distance between the Er and vacancy positions. Since we do not expect the Er concentration to change as a function of annealing temperature up to 900 ℃, we would not expect the net $V_O^{\bullet\bullet}$ concentration to change for reasons of film charge neutrality. It is however possible that annealing can lead to diffusion-induced redistribution of oxygen vacancies, leading to their clustering (to form complexes) or gettering by grain boundaries, altering the Er-V_O interactions. This may lead to improvements in the optical properties as observed.

6.8 Conclusions and remarks regarding the status Er:CeO_2 system

The Er:CeO_2/Si system presents an attractive combination of benefits, as it is an ideal host oxide for a spin defect with its very low nuclear noise environment, and has low lattice mismatch for epitaxial growth on silicon. In these studies, we have carried out a detailed microstructural and optical study of MBE-grown epitaxial Er:CeO_2/Si in the 2-130 ppm Er doping range, yielding results relevant for development in quantum coherent device applications. We establish a baseline for this material in the context of key metrics for rare-earth doped oxide systems: as-grown films at 2-3 ppm Er doping show EPR linewidths as narrow as 245(1) MHz, optical inhomogeneous linewidths down to 9.5(2) GHz, an optical excited state lifetime as long as 3.5(1) ms, and a spectral diffusion-limited homogeneous linewidth as narrow as 4.8(3) MHz. Post-growth annealing up to 900 ℃ yields improvement of the optical inhomogeneous linewidth and excited state lifetime by 20% and 40% respectively.

In studying the doping dependence of the spin and optical parameters as a function of

Er doping, we show that the functional dependence is consistent with a charge dipole-based interaction model. We find that the linewidths for our thin films are broader than the corresponding linewidths in high-quality Er-doped bulk samples, likely due to the thin film nature – and therefore proximity to interfaces – and non-equilibrium growth process of our material system, the latter leading to a larger number of grown-in defects. That said, the ~ 5 MHz spectral diffusion linewidth in the as-grown films is sufficiently narrow to indicate the potential for long optical coherence in the hundreds of nanoseconds, enabling the exploration of measurement techniques such as photon echo[60] to directly probe the optical coherence of Er^{3+} in CeO_2.

We are then indeed able to probe that long optical coherence via photon echo, in our effort to highlight this material system as a potential robust optical quantum memory platform, finding. The observed homogeneous linewidth of 440 kHz for the Y_1-Z_1 transition and electron spin relaxation time on the order of a millisecond at liquid helium temperatures indicate the feasibility of using collective electron spin relaxation as a local quantum memory for quantum repeaters. The narrow homogeneous linewidth of 440 kHz also demonstrates the potential for integrating Er^{3+} with nanophotonic cavities to achieve Purcell enhancement and near Fourier transformation-limited single-photon emission. This would allow for coherently driven optical transitions at a desired rate to address individual ions[111,112] and examine the time-dependent spectral diffusion of individual Er^{3+} ions in the host,[25] a critical step towards entanglement distribution needed for quantum repeaters. The significant reduction in the concentration of nuclear magnetic moments in CeO_2 compared to that of other hosts, such as Y_2SiO_5 and YAG, could open a path towards not only long-lived coherent Er^{3+} electron spin states, but also long-lived nuclear spins in isotopically enriched ^{167}Er to enable long storage times on the scale of seconds, using both collective relaxation modes of nuclear spin ensembles[15] and individual nuclear spin states[113,114].

Regarding the spin aspect of this system, the Er^{3+} spin ensemble coherence value reported

is largely limited by the ion-ion dipolar interaction. As indicated by the instantaneous diffusion measurements, in the single-ion limit the Er^{3+} spin coherence T_2 is around 0.66 μs. One could further improve spin coherence by lowering the temperature below the explored 3.6 K in this work to milliKelvin temperatures. One can also further improve coherence by using higher magnetic fields to freeze spin-flip induced dephasing.

Additionally, the MBE growth of Er-doped oxides also enables the control of Er doping levels and optimization of material quality in minimizing defects and dislocations in the film to reach high quality single crystal CeO_2, thereby reducing spectral diffusion and improving on both optical and spin properties. It can also enable growth of CeO_2 thin films with controlled delta doping of Er to create structures compatible with nanophotonic cavity integration, either within the oxide or within hybrid structures integrated with other dielectric materials. The sample studied here is grown without growth optimization, yet already demonstrates appreciable spin relaxation and narrow optical homogeneous linewidths (440 kHz). Continued growth optimization employing slower growth rates – perhaps with lower oxygen pressure[67] to suppress formation of dislocations and further reduce unintended defect concentrations in the film – has the potential to generate samples reaching narrower homogeneous linewidths along with longer spin coherence and relaxation. Thus, Er^{3+} in CeO_2, an oxide host with a very low nuclear spin environment, could emerge as a versatile platform for highly coherent light–matter quantum interfaces for developing quantum communication applications.

CHAPTER 7

EXTENDING ER:CEO_2 TO SI(001) FOR IMPROVED DEVICE FABRICATION CAPABILITIES

7.1 Motivation for Er:CeO_2 on Si(001)

The work on Er:CeO_2 in Chapter 6 has shown the potential for the system as a quantum communication platform. As a next step, we are interested in transferring this thin film system from being grown on Si(111) to being grown on Si(001).

Silicon-on-insulator (SOI) is a required component of nanophotonics engineering and device integration, as the buried oxide layer and Er-doped oxide thin film act as cladding for the nanophotonic cavity built into the silicon layer.[21,22] However, SOI is typically only available in the Si(001) orientation, and so we are interested in adapting our CeO_2(111) on Si(111) system accordingly.

In pursuing the growth of Er:CeO_2 on Si(001), there are two questions we ask: First, are we able to grow CeO_2 epitaxially on Si(001)? Second, failing epitaxial growth, is non-single crystal sufficient for our applications? Literature on CeO_2 on Si(001) indicates that this is a difficult prospect, typically resulting in multi-domain growth in other orientations[115,116] unless strict conditions are met, such as room-temperature growth[117] or the insertion of complex buffer layers.[116] That said, Er optical properties in TiO_2 have been shown in other systems to behave similarly in single- and poly-crystalline environments.[20] Given this context, it is worth investigating both of these questions.

7.2 Examining optical characteristics of Er:CeO_2 on Si(001)

For examining the effects of growing Er:CeO_2 on Si(001), we grew a selection of Er:CeO_2 thin film samples with 10 ppm Er doping on Si(001), Si(111), and STO(001) – with the growths

Substrate	**Growth Info**	**RHEED Pattern**	Γ_{inh} (GHz)	T_1 (ms)	Γ_{SD} (MHz)
Si(001)	Room-temp	Poly rings	No signal	–	–
Si(111)	Standard	Single streaks	16.8 ± 1.1	3.6 ± 0.1	328 ± 13
Si(001)	Standard	Multi streaks	28.9 ± 3.5	3.8 ± 0.1	450 ± 8
Si(001)	2-stage	Multi streaks	27.6 ± 3.5	3.7 ± 0.1	438 ± 8
STO(001)	Standard	Single streaks	28.2 ± 0.3	5.3 ± 0.2	397 ± 7

Table 7.1: Details on samples used in the Er:CeO_2/Si(001) studies. The choice of substrate and information on the growth conditions yield varied RHEED patterns, Z_1-Y_1 inhomogeneous linewidths Γ_{inh}, Z_1-Y_1 excited state lifetimes T_1, and Z_1-Y_1 spectral diffusion linewidths Γ_{SD}.

on Si(111) and STO(001) expected to act as two epitaxial references: since Si(111) is lattice matched and known to grow epitaxially, and STO is lattice matched with CeO_2 with a 45 degree in-plane rotation.[118] Samples grown on Si(001) were 70 nm thick; samples on Si(111) and STO(001) were 50 nm thick. We then performed optical characterization on Er:CeO_2 Z_1-Y_1 transition, as identified in Chapter 6. We obtained the inhomogeneous linewidth Γ_{inh}, spectral diffusion linewidth Γ_{SD}, and the excited state lifetime T_1 for this transition.

To produce these samples, we follow the MBE growth procedures laid out in Chapter 3 to grow Er:CeO_2 thin films on Si(111). For this growth campaign, Er and Ce were evaporated using resistively heated effusion cells (Riber HT-12 and Veeco HT 24cc, respectively), and ultra-high purity molecular oxygen (O_2) was provided via an MKS mass flow controller. Beam equivalent fluxes of the Ce and O_2 were determined using a beam flux monitor to set a ratio of O_2 to Ce of ~ 1 during growth, with growth rates of 50-70 nm/hr.

Information on the samples and their resulting optical properties is shown in Table 7.1. We note in the table the growth recipe variation used for each growth. The "standard" growth is the same as the one used for Er:CeO_2(111) in Chapter 6. "Room-temp" indicates growth performed with the substrate heater turned off and the substrate heater thermocouple reading less than 100 ℃, to match the conditions of Ami *et al.*[117] "2-stage" indicates a growth started at lower temperature ($\sim$ 500 ℃) and gradually increased to the "standard" temperature ($\sim$ 700 ℃) over the course of the first few minutes of growth.

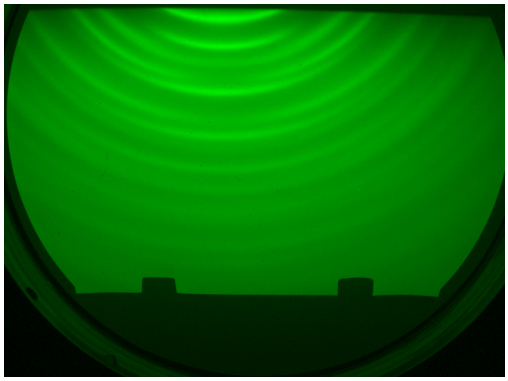

(a) Polycrystalline RHEED pattern of Er:CeO_2 grown at room temp on Si(001).

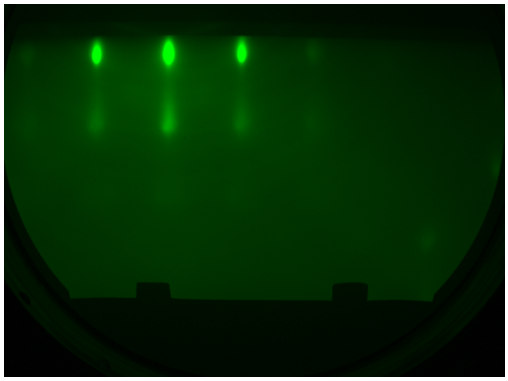

(b) Streaky RHEED pattern of Er:CeO_2(001) grown epitaxially on STO(001).

Figure 7.1: RHEED patterns for Er:CeO_2 grown on (001)-oriented substrates. Polycrystalline rings can be seen in (a) after room-temperature growth of CeO_2 on Si(001). The image is taken along the Si⟨100⟩ azimuth. Epitaxial streaks can be seen in (b) after growth of CeO_2 on STO(001). STO⟨110⟩ azimuth. The faint polycrystalline rings overlaying the streaks are from the molybdenum sample holder upon which the STO substrate is rested.

During growth, we observed *in situ* via RHEED that the samples on Si(111) and STO(001) grew epitaxially, with streaky patterns indicating single-crystal growth; we observed that the room temperature growth yielded polycrystalline ring patterns. The RHEED patterns for these CeO_2 films on (001)-oriented substrates are shown in Figure 7.1. The RHEED pattern for the CeO_2 thin film on Si(111) was the same as shown in Figure 6.1. The growths on Si(001) at standard growth temperature yielded a complex streaky RHEED pattern. We discuss these RHEED results in combination with investigation via SEM in the next section.

We begin analysis by noting that the sample grown at room temperature did not yield Er^{3+} photoluminescence signal when probed with PLE – we speculate this is due to the doped-in Er^{3+} not obtaining the appropriate oxidation state within the CeO_2 lattice. We additionally note that the two samples grown on Si(001) are very nearly optically equivalent, with measured inhomogeneous linewidths, excited state lifetimes, and spectral diffusion linewidths within experimental error of each other despite the modification of growth conditions for the 2-stage growth. The two samples also had nearly identical RHEED patterns,

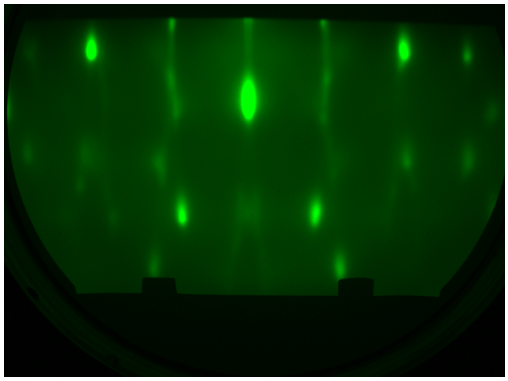

(a) RHEED pattern of Er:CeO_2/Si(001) along the Si⟨100⟩ azimuth.

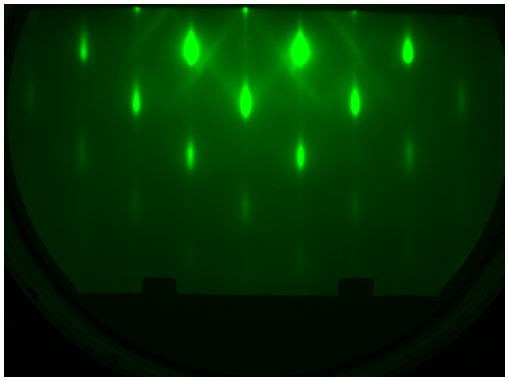

(b) RHEED pattern of Er:CeO_2/Si(001) along the Si⟨110⟩ azimuth.

Figure 7.2: RHEED pattern of Er:CeO_2 grown on Si(001) at ~ 700 ℃ along two different Si azimuths, using a 15 kV electron beam. A multi-domain pattern is observed, with two sets of overlapping streaks observed in panel (a). The angle between the streaks of the chevrons in (b) is between 73 and 75 degrees.

---

and so we conclude that the slight modification of growth conditions did not impact the growth dynamics of CeO_2 on Si(001).

Given these notes, we constrain our discussion of optical results to the "standard" growth recipe for the samples grown on Si(001), STO(001), and Si(111).

Performing optical characterization via PLE and TSHB, we identify that the Er:CeO_2 films grown on (001)-oriented substrates result in $\sim 70\%$ broader inhomogeneous linewidths than when grown on a (111)-oriented substrate. The excited state lifetimes for Er:CeO_2 on Si substrates are within experimental error of each other, but both have $\sim 30\%$ shorter excited state lifetimes compared to the sample grown on STO. Finally, we find that the spectral diffusion linewidths varies with each sample: 328 ± 13 MHz for Er:CeO_2/Si(111), 397 ± 7 MHz for Er:CeO_2/STO(001), and 450 ± 8 MHz for Er:CeO_2/Si(001).

7.3 Examination of Er:CeO_2 on Si(001) microstructure

While the RHEED patterns of CeO_2 growth at low temperature and on a lattice-matched oxide substrate are fairly straightforward, the RHEED patterns for CeO_2 on Si(001) grown

at standard temperature, shown in Figure 7.2, are more complex. We identify two domains of crystalline material based on the two overlaid streak patterns along the Si⟨100⟩ azimuth in panel (a), though in panel (b) both patterns overlap perfectly along the ⟨110⟩ azimuth and additionally reveal chevron patterns that may indicate faceting or similar surface features.

We expect, at these temperatures and flux ratios, that CeO_2 will successfully form. However, we know from the literature that the CeO_2 lattice may form non-epitaxially with respect to the Si(001) surface. When viewing the RHEED during growth, we identified via rotation that the patterns had four-fold symmetry with respect to the azimuthal angle – indicating that the four-fold symmetry of the Si(001) surface carried through into the film. Post growth, we also analyze the streak spacing for the multi-domain RHEED images, in an attempt to identify an orientation relationship. Measuring the images, we find that pairs of streaks with the same angle in Figure 7.2(a) are separated by 121 ± 3 pixels, while streaks in Figure 7.2(b) are separated from the center streak by either 85 ± 1 pixels or 170 ± 1 pixels. Knowing the electron de Broglie wavelength of 0.099 Å, and the substrate-to-screen distance of 3292 pixels, we can compute the plane spacing for each of these using Equation 3.1. We find that the streaks in panel (a) correspond to a plane spacing of $d_a = 2.69 \pm 0.07$ Å and the streaks in panel (b) correspond to a plane spacing of $d_{b,1} = 3.83 \pm 0.05$ Å and $d_{b,2} = 1.91 \pm 0.01$ Å.

We find that these plane spacings may either match CeO_2(001) or CeO_2(011) growth. The observed plane spacing of $d_a = 2.69 \pm 0.07$ Å strictly matches the spacing between $CeO_2\{100\}$ planes (2.73 Å along the $CeO_2\langle 100\rangle$ azimuth). However, the observed spacing of $d_{b,1} = 3.83 \pm$ 0.05 Å may match either the spacing between $CeO_2\{110\}$ planes (3.86 Å along the $CeO_2\langle 110\rangle$ azimuth) or the spacing between $CeO_2\{7,\bar{7},10\}$ planes (3.88 Å spacing when viewed at a 45 degree rotation from the $CeO_2\langle 110\rangle$ azimuth, as though rotating from the Si⟨100⟩ azimuth to the Si⟨110⟩ azimuth per our growth conditions). We might expect to instead view the $CeO_2\{111\}$ planes, but those are 10 degrees removed from the Si⟨110⟩ azimuth in this context,

Figure 7.3: SEM image of the surface of a CeO_2 thin film grown on Si(001). We observe a distinctive cross-hatching pattern formed by two domains of CeO_2 crystallites, with the two domains aligned with the Si$\langle 100 \rangle$ and Si$\langle 010 \rangle$ directions.

---

and the four-fold symmetry in the RHEED during rotation may strictly be described by the C_4 2D point group, with 90 degree rotations between occurrence of the reconstruction seen in Figure 7.2(a) and strict 45 degree rotations between the reconstructions in Figure 7.2(a) and Figure 7.2(b).† Nonetheless, the spacing between $CeO_2\{7,\bar{7},10\}$ planes of 3.88 Å is consistent with the RHEED streak spacing observed along the Si$\langle 110 \rangle$ azimuth during growth. We are thus left with two possibilities, either $CeO_2(001)$/Si(001) growth or $CeO_2(011)$/Si(001) growth.

In the interest of resolving which of the two orientations resulted in our growth, we perform inspection of the CeO_2/Si(001) surface by SEM in Figure 7.3 to look for any identifying

†. Additionally, there are indeed coherent sets of Ce atoms describing this plane, with three Ce atoms in each of these planes per unit cell. The choice of plane, though odd, is at least not aphysical in generating the observed RHEED pattern.

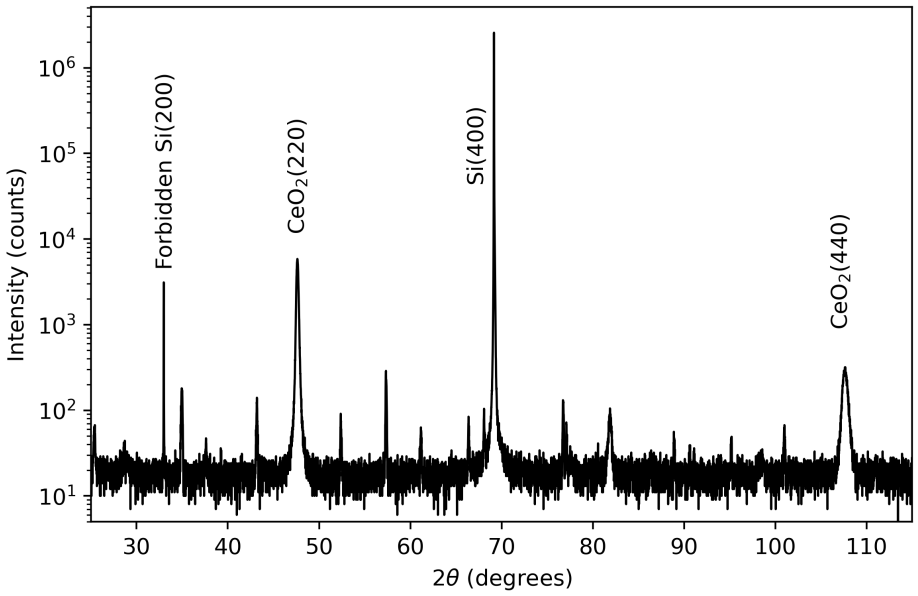

Figure 7.4: Wide ω-2θ X-ray diffraction scan of the CeO_2 thin film grown on Si(001) under standard growth conditions. We clearly observe CeO_2(220) and CeO_2(440) peaks, along with the expected Si(400) substrate peak. The forbidden Si(200) peak is weakly observed. No unlabelled peaks were identified to be related to CeO_2 or Si, and instead are likely be artifacts from the experimental apparatus.

---

surface features, particularly given the $\sim 74^\circ$ chevrons indicating faceting in Figure 7.2(b). We find a distinctive cross-hatching pattern formed by two domains of crystallites, with the two domains aligned with the Si$\langle 100 \rangle$ and Si$\langle 010 \rangle$ directions. Surveying the literature, this was observed by Inoue *et al.* (1993) under similar growth conditions, and is a strong indicator of epitaxial CeO_2(110) growth.[119]

We perform XRD on the CeO_2/Si(001) sample in Figure 7.4 and find that we have peaks corresponding to CeO_2(220) and CeO_2(440). This confirms we are growing CeO_2(110), in line with expectations in the literature.[119]

7.4 Remarks and next steps for Er:CeO_2 on Si(001) exploration

Our interest in exploring the possibility of Er:CeO_2(001) grown on Si(001) for purposes such as nanophotonics integration has thus yielded useful results. We have identified that, while

CeO_2 may be growing in the (110) orientation on Si(100), it still has viable optical properties for continued exploration.

We identified that, regardless of growth on Si(001) or STO(001), the inhomogeneous linewidth and spectral diffusion linewidth are both broader than on Si(111). This could indicate that while the growth window used for CeO_2(111) growth is viable for exploring epitaxy in the (001) orientation, it is by no means optimized for it. Thus we have a need for additional exploration of the CeO_2(001) growth window, to minimize broadening and decohering defects in preparation for when a method of CeO_2(001) on Si(001) is identified. We do note, however, that the multiple domains of CeO_2 upon on the Si(001) substrate do not appear to cause additional inhomogeneous broadening in contrast to the CeO_2(001) on STO(001) case, matching the result of comparing single crystal versus polycrystalline Er-doped TiO_2 grown via MBE.[20]

We also remark upon the similar degrees of quenching in the Er excited state lifetime T_1 between the growths on Si(001) and Si(111), as compared to the longer T_1 value obtained on STO(001). We speculate that this could indicate defects such as oxygen vacancies caused by the gettering of oxygen out of the CeO_2 and into the silicon substrate, in concordance with how oxygen annealing yielded longer lifetimes in Er:CeO_2(111) in Chapter 6, perhaps via removal of those same oxygen vacancies.

Next steps for this project will be the exploration of optimal growth parameters for CeO_2(001) growth – starting on STO(001) – and the investigation of other routes to CeO_2(001) on Si(001). We will likely start growth parameter exploration in the vicinity of the current growth window, perhaps investigating higher growth temperatures or altered substrate surface preparation techniques, to bypass the formation of common defects encountered in MBE. Regarding growth on Si(001), we may need to investigate the use of buffer layers such as STO on Si(001), which have canonically been used to obtain epitaxial oxides on silicon where the oxide may not template properly on the silicon surface. Via both of these explorations, we

hope to identify a route towards improving optical properties of CeO_2 on Si(001) to match or surprass those found on Si(111), with an eye towards future nanophotonics integration on (001)-oriented SOI.

CHAPTER 8

LEVERAGING ER ENERGY STRUCTURE FOR COMPUTATIONAL EXPLORATION

8.1 Identify hosts that yield brighter Er defects

While Er^{3+} ions are an ideal defect for quantum memory due to their 1.5 μm optical transition and long-coherence-time spin state, they suffer from one particular drawback: the erbium spontaneous emission rate.

Erbium is, in common parlance, a remarkably dim ion. Its radiative relaxation lifetimes T_1 from the Y levels to the Z levels generally occur on a timescale of milliseconds, across a wide variety of possible crystal hosts.[18] The result of this is that, for a quantum memory using a single ensemble of Er ions, the repetition rate of optical operations (e.g., extracting the spin state using optical readout) is limited to less than 1 kHz – orders of magnitude less than the desired 100 kHz to 100 GHz bandwidth targeted for quantum communication applications.[1]

In this chapter, therefore, we discuss methods for speeding up the radiative relaxation lifetimes of rare-earth ion defects, in this case focusing on Er^{3+}. We identify a viable method for doing this – careful selection of crystal hosts – and explore high-throughput computational methods for surveying a large number of materials to identify optimal hosts for brighter Er.

We start with discussion of the methods for speeding up relaxation from the Y levels to the Z levels in Er^{3+}. There are three methods that immediately arise with a sense of technological viability: The first method is the intentional introduction of proximal defects near our Er defect. Additional defects may provide additional relaxation pathways, and so the lifetime of the excited state is shortened. However, these additional relaxation pathways may not be radiative at the desired wavelengths, which causes the system to incur additional decoherence processes while decreasing overall efficiency – as such, we reject this method.

The second method is the engineering of nanophotonic cavities around the Er defect to modify the density of states and by consequence the radiative relaxation rate. This method is well-studied, with Purcell enhancements (multiplicative radiative relaxation rate increases) in the hundreds demonstrated for Er-doped oxide thin films on silicon,[21,22] leading to cavity-enhanced lifetimes on the order of 10 μs, or optical operation bandwidths closer to the order of 100 kHz.

The third method for increasing the radiative relaxation rate – which may work in tandem with nanophotonics engineering, leading to additional gains in bandwidth – is by careful selection of the host into which Er is placed. As will be discussed, the radiative relaxation rate is directly tied into the nature of the crystal field surrounding the ion, and we may exploit this to identify crystal hosts for which the Er relaxation rate is faster. This calculation is discussed in Section 8.2, the computational methods for performing this calculation at scale is discussed in Section 8.3 and then the results of this calculation applied over a large set of possible host materials obtained from the Materials Project[120] is evaluated in Section 8.4.

8.2 Calculating trivalent erbium oscillator strengths

A common metric on brightness is oscillator strength, defined as the ratio between the emission rate of our defect with the emission of a classical single-electron oscillator with the same transition energy.[121] The oscillator strength f is inversely proportional to the excited state lifetime T_1, as $f \sim 1/T_1$. For this project, we take the conversational descriptor that brighter Er corresponds to larger oscillator strengths, and dimmer Er to smaller oscillator strengths.

In this work, we are interested primarily in evaluating the electric dipole oscillator strength f_{ED}. Though the electric dipole transition is parity forbidden between the ${}^4I_{13/2}$ and ${}^4I_{15/2}$ levels since both levels are of the $4f$ configuration, admixing of higher states of the $5s$ and $5d$ configurations weakly allows the electric dipole transition. The admixing

process, which is dependent on the crystal host in which the Er ion is embedded, generally yields electric dipole oscillator strengths on the order of 10^{-6} for Er ions,[14] corresponding to excited state lifetimes in the millisecond regime.

The transition between ${}^4I_{13/2}$ and ${}^4I_{15/2}$ can also occur via the magnetic dipole transition process. However, the magnetic dipole oscillator strength for Er^{3+} is typically on the scale of 10^{-7} for the ${}^4I_{13/2}$ and ${}^4I_{15/2}$ transition.[122] It also does not change significantly depending on the crystal host, because the magnetic dipole transition is not parity forbidden – the main process by which it occurs is primarily dependent on the coupling between the total angular momenta and $\hat{z}$-quantized total angular momenta in the excited and ground state, and only weakly modified by the diagonalization of the crystal field levels in that basis.[36,37] As such, we focus our attention on the electric dipole process – both because it may contribute more to the Er brightness, and because we can do more to directly modify its brightness.

Judd and Ofelt identified a second-order perturbation method to account for the parity admixing of higher states,[123,124] which may be used to evaluate the oscillator strength for the Er electric dipole transition between the ${}^4I_{13/2}$ and ${}^4I_{15/2}$ levels.† The equation for this is as follows, for the mass of the electron m, transition frequency ν, Planck constant h, multiplicity of the ground state $2J+1$ per the total angular momentum J, polarization of the transition ρ, final and initial states $\langle\alpha|$ and $|\alpha'\rangle$, and electric dipole operator $D_\rho^{(1)}$:

$$f_{\mathrm{ED}} = \chi \frac{8\pi^2 m\nu}{3h(2J+1)} \sum_{\rho=-1}^{+1} \left| \langle\alpha| D_\rho^{(1)} |\alpha'\rangle \right|^2 \tag{8.1}$$

This equation also includes a material-specific local field correction factor χ, which accounts for the refractive index of the host.[123] Computing this constant requires knowledge of the refractive index, which is not a given for every material. As such, in this work we will discuss the oscillator strength without including this correction factor. This remains

†. Note that we are not discussing Judd-Ofelt theory as it is usually identified, per se, via the parameters Ω_λ. Rather, we are discussing here the precursor to Judd-Ofelt theory, which does not invoke phenomenological parameters and instead requires detailed knowledge of the crystal field – as will be discussed.

appropriate, as sometimes the correction factor is not included in the oscillator strength and is instead included in the definition of the emission rate constant.[88]

The electric dipole matrix elements may be computed through the following set of equations:[123]

$$\langle B|\, D_{\rho}^{(1)}\, \left|B'\right\rangle = \sum_{k,q,\text{ even }\lambda} (2\lambda+1)(-1)^{q+\rho} A_q^{(k)} \times \begin{pmatrix} 1 & \lambda & k \\ \rho & -q-\rho & q \end{pmatrix} \langle A|\, U_{q+\rho}^{(\lambda)}\, \left|A'\right\rangle \Xi(k,\lambda) \tag{8.2}$$

$$\Xi(k,\lambda) = 2\sum_{n',l'} (2l+1)(2l'+1)(-1)^{l+l'} \times \begin{Bmatrix} 1 & \lambda & k \\ l & l' & l \end{Bmatrix} \begin{pmatrix} l & 1 & l' \\ 0 & 0 & 0 \end{pmatrix} \begin{pmatrix} l' & k & l \\ 0 & 0 & 0 \end{pmatrix} \frac{\langle nl|\, r\, \left|n'l'\right\rangle \langle nl|\, r^k\, \left|n'l'\right\rangle}{\Delta(n'l')} \tag{8.3}$$

$$\langle A| = \sum_M a_M \left\langle l^N \gamma S L J M\right| \qquad \left|A'\right\rangle = \sum_{M'} a_{M'} \left|l^N \gamma' S' L' J' M'\right\rangle \tag{8.4}$$

Equations 8.2 and 8.3 detail the evaluation of the electric dipole matrix element for a single polarization ρ. The final and initial (ground and excited) states are $\langle B|$ and $\left|B'\right\rangle$, where $|B\rangle$ is the perturbed eigenvector produced from the admixing process upon the atomic $|A\rangle$ basis, which is described in Equation 8.4. k and q are the rank and component numbers, respectively, used to describe the spherical harmonics; λ is a summation index used when coupling to higher configuration states; n is the principal quantum number and l is the angular quantum number for the electron being evaluated; S, L, and J are the quantum numbers describing the rare-earth ion level, per Section 2.1.1. $\Delta(nl)$ is the energy splitting to higher configuration states (see Judd 1962 for more details[123]), r is the radial electron coordinate, and $U_k^{(q)}$ is the unit tensor evaluated for k and q. The symbols in parentheses

and curly braces are 3-j and 6-j symbols, respectively.[125] Finally, the coefficients $A_q^{(k)}$ are the crystal field coefficients determined in Section 2.1.2.

The evaluation of $\Xi(k,\lambda)$ requires knowledge of the transition energy $\Delta(n'l')$ and the radial wavefunction integrals. Values for both of these are provided by Judd,[123] but evaluation of Ξ can be improved by examining the radial wavefunctions by more modern density functional theory techniques.[126,127,128,129] It is otherwise straightforward to calculate using l and l', the angular quantum numbers of the ground and excited state.

Computing the matrix element of the unit tensor operator $U_{q+\rho}^{(k)}$ requires finding the requisite doubly reduced matrix element. First, we recall the definitions of the initial unperturbed states $\langle A|$ and final unperturbed states $\left|A'\right\rangle$, where we use the Russel-Saunders (LS) coupling and include the S and L as quantum numbers to complement J and its projection M (alternatively written as J_z). Thus we may evaluate the matrix element of the unit tensor operator in our unperturbed basis, according to the reduced matrix element definitions provided by Wybourne.[36]

$$\langle A|\, U_{q+\rho}^{(\lambda)} \left|A'\right\rangle = \sum_{M,M'} a_M a_{M'} \left\langle l^N \gamma S L J M \right| U_{q+\rho}^{(\lambda)} \left| l^N \gamma' S' L' J' M' \right\rangle \tag{8.5}$$

$$\begin{aligned}\left\langle l^N \gamma S L J M \right| U_{q+\rho}^{(\lambda)} \left| l^N \gamma' S' L' J' M' \right\rangle &= (-1)^{J-M+S+L+J'+\lambda} \sqrt{(2J+1)(2J'+1)} \\ &\times \begin{pmatrix} J & \lambda & J' \\ -M & q+\rho & M' \end{pmatrix} \begin{Bmatrix} J & J' & \lambda \\ L' & L & S \end{Bmatrix} \left\langle l^N \gamma S L \right| \left| U^{(\lambda)} \right| \left| l^N \gamma' S' L' \right\rangle \end{aligned} \tag{8.6}$$

The reduced matrix elements of the form $\langle \gamma S L|\, |U^(k)|\, \left|\gamma' S' L'\right\rangle$ in the final equation may then be looked up in Nielson & Koster.[130]

While the crystal field coefficents must be computed per-material, once those are provided and once the reduced matrix elements, radial integrals, and energies are looked up, the

evaluation of the matrix element per Equation 8.2 is straightforward: the summations only require basic loops, and the 3-j and 6-j symbols may be evaluated via computer algebra methods provided by readily available code modules.[131]

8.3 Computational methods for "bright" host evaluation

The evaluation of the oscillator strength of Er^{3+} in a particular crystal host takes place in two stages: First, the crystal field coefficients are evaluated for the selected host. Second, the coefficients are used to compute the oscillator strength per the previous section.

The crystal field coefficients are determined via the sum over the point charges in the crystal per Equation 2.15. When evaluating the sum, we place the Er^{3+} ion in a distinct cationic site in the proposed host crystal and treat that as the origin – with distinct sites labelled by the cation being replaced, the site symmetry of the replaced cation, and the coordination environment around the site. The latter two cases are necessary for materials like Y_2O_3 (where the Y cation may sit in two different site symmetries) and Y_2SiO_5 (where the Y cation may sit in two different coordination environments, but the same site symmetry). We additionally evaluate the host crystal for up to the three most probable oxidation states for the elemental constituents that lead to charge balance in the chemical formula for that host, using the Composition tool provided by the Python Materials Genomics library.[132]

Once evaluated, the crystal field coefficients are submitted to Equation 8.2 for the three different polarization values $\rho \in \{-1, 0, 1\}$, the outputs of which are used to evaluate f_{ED} per Equation 8.1.

Before proceeding with evaluation however, we note that a computational optimization may be obtained when judging many sets of crystal field coefficients. The summation over k, q, and λ in Equation 8.2 may be split into two – a sum over k and q, and a sum over λ for each value of k and q for an evaluation of polarization ρ.

$$\langle B| D_\rho^{(1)} \left|B'\right\rangle = \sum_{k,q} A_q^{(k)} \lambda_{kq,\rho} \tag{8.7}$$

$$\lambda_{kq,\rho} = \sum_{\text{even } \lambda} (2\lambda+1)(-1)^{q+\rho} \begin{pmatrix} 1 & \lambda & k \\ \rho & -q-\rho & q \end{pmatrix} \langle A| U_{q+\rho}^{(\lambda)} \left|A'\right\rangle \Xi(k,\lambda) \tag{8.8}$$

By pre-computing $\lambda_{kq,\rho}$ – which does not depend on the crystal host at all, and indeed only depends on the identity of the rare-earth being evaluated – and then looking up those values when evaluating the electric dipole matrix elements, we may reduce computation time for evaluating a single material by up to 95% (per testing on a single core of an AMD Ryzen 7 PRO 7840U CPU: 0.2 seconds to evaluate without caching, 0.04 seconds with caching).

To survey a large number of materials, we searched the Materials Project database[120] for all materials with a bandgap greater than 1 meV (corresponding to allowing optical transitions down to 1240 nm in wavelength – to ensure that the standard Er^{3+} transition wavelength of 1.5 μm is not impacted by a nearby conduction band). This results in ∼350,000 evaluated environments for Er^{3+} across ∼58,000 material structures. The oscillator strength of Er^{3+} in each of these ∼350,000 environments was calculated using the Midway2 supercomputing cluster resources provided by the University of Chicago's Research Computing Center, and the results of these calculations is discussed in the following section.

8.4 Results of computational survey on Er hosts

The first question that arises upon computing the oscillator strengths from the ∼350,000 Er^{3+} environments extracted from the Materials Project database is the reliability of the calculations. We are able to compare the calculated values with known values and we arrive at some preliminary agreement, per Table 8.1. We identify that our results tend towards overestimating oscillator strengths, but that the values obtained are of generally appropriate

Material	**Site Info**	$f_{\text{ED,calc}}$	$f_{\text{ED,lit}}$
$LiNbO_3$	Li site	2×10^{-6}	1×10^{-6}
$LiYF_4$	Li site	2×10^{-7}	2×10^{-7}
Y_2SiO_5	O-6 Y site	2×10^{-7}	3×10^{-7}
Y_2SiO_5	PB-7 Y site	9×10^{-8}	2×10^{-8}
$CaWO_4$	Ca site	2×10^{-7}	2×10^{-8}

Table 8.1: Initial comparison of calculated oscillator strength $f_{\text{ED,calc}}$ with literature values $f_{\text{ED,lit}}$. Literature values here are obtained from Thiel *et al.*[18] Sites are identified by cation, and coordination environment in the case of Y_2SiO_5.

scale and trend. Additional verification will be required as this project progresses, but we take this as a good sign for interpreting trends and developing rules of thumb for selecting hosts for brighter Er.

Looking at the aggregate list of values, we promptly notice oscillator strengths both orders of magnitude higher and orders of magnitude lower than the standard 10^{-6} found in the literature. To begin understanding what may cause the calculated Er brightness to be identified as brighter, we plot the oscillator strengths against the atomic number of the cation for which Er is substituted in Figure 8.1(a).

We observe that while the cation atomic number does not absolutely correlate with the calculated oscillator strength f_{ED} when Er^{3+} is substituted for that element, there is an envelope on the maximum oscillator strength, with larger oscillator strengths arising at lower substituted cation atomic number. This indicates to us that there is a trend involved with the distance between ions in the crystal – given that, for example, hydrogen ($Z = 1$) is a very small ion compared to zirconium ($Z = 40$), and can result in very small inter-atomic distances. However, we recognize the placement of Er^{3+} into a hydrogen site as aphysical without significant rearrangement of the ions around the hydrogen site. Since we are not currently equipped to perform the requisite molecular dynamics simulations for hundreds of thousands of materials, we will instead apply filters on the substituted cation radius. With our point of reference being Er^{3+} with a cationic radius of ∼97 picometers,[133] for

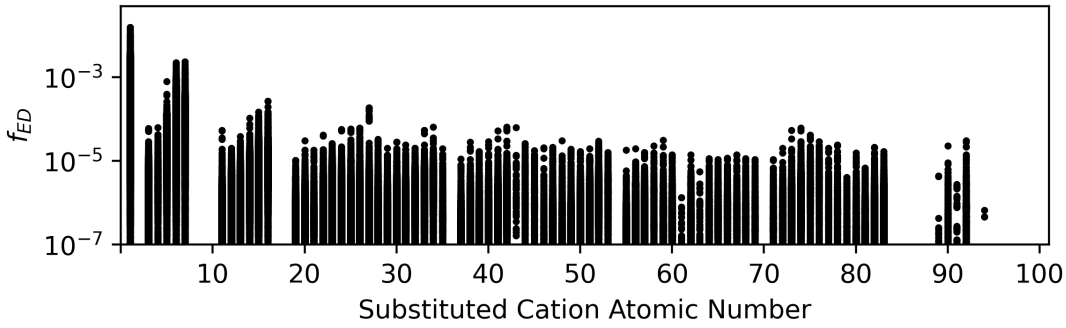

(a) Oscillator strengths plotted against atomic number, generated from the full list of ∼350,000 environments.

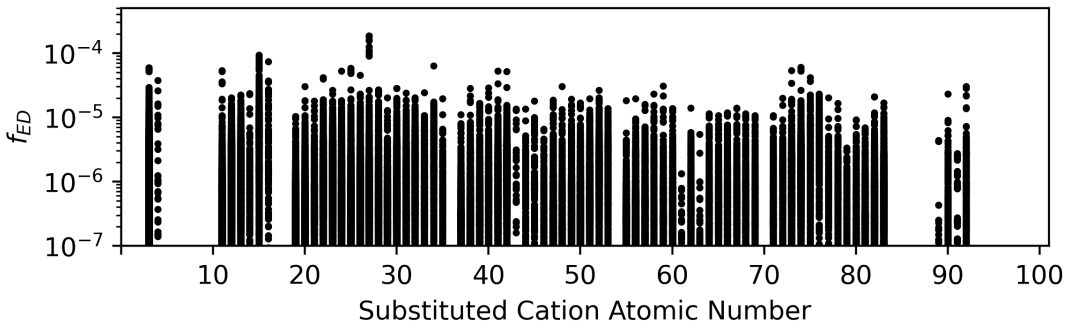

(b) Same set of oscillator strengths, now filtered to such that the minimum substituted cation radius size is ∼ 40 picometers.

Figure 8.1: Scatter plot of calculated oscillator strengths f_{ED} plotted against the atomic number of the substituted-for cation, with the full list of environments in (a) and with a filtered list of environments in (b). Each placed dot is one entry in the list of ∼350,000 environments into which Er^{3+} may be placed.

---

now we set the minimum cation radius to 40 picometers, the approximate ionic radius of titanium,[133] given the successful integration of Er into titanium sites in TiO_2.[20,21] We see in Figure 8.1(b) that the oscillator strengths organized by substituted cation atomic number after this filtering show that the envelope where f_{ED} increases with decreasing atomic number has largely vanished.

We may investigate further regarding the trend identified regarding distance between ions in the host crystal. In the process of generating the crystal field coefficients, we may obtain

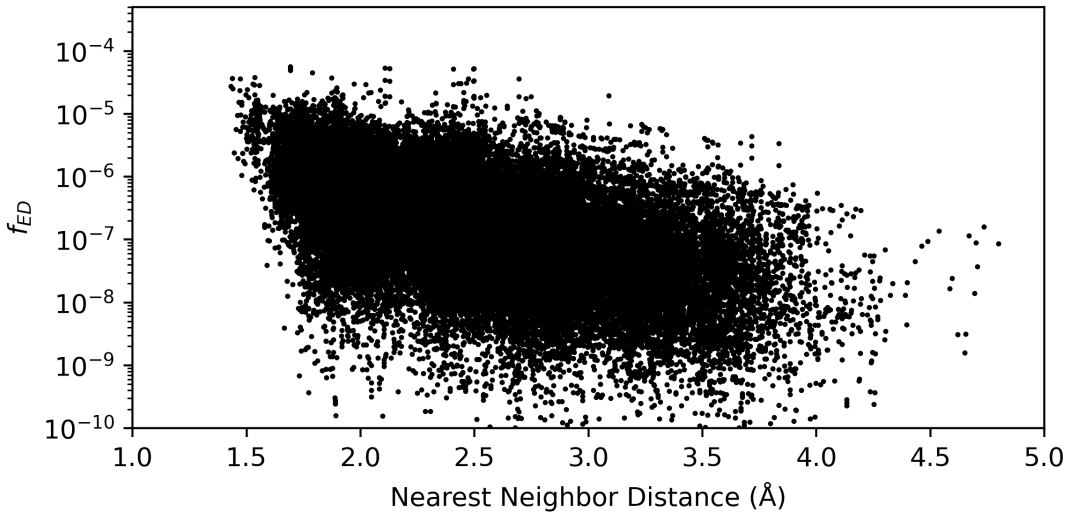

Figure 8.2: Scatter plot of calculated oscillator strengths f_{ED} plotted against the nearest-neighbor distance, defined as the distance between the evaluation Er^{3+} ion and the nearest ion to the Er in the host crystal. Each placed dot is one entry in the list of ∼350,000 environments, after cation size filtering, into which Er^{3+} may be placed. We identify a correlation between decreasing nearest-neighbor distance and oscillator strength with a Pearson correlation coefficient of $r = -0.3$.

---

the distance to the nearest neighbor of the Er ion, defined as the minimum value of $R_i \; \forall \; i$ in Equation 2.13. Plotting the oscillator strength against nearest-neighbor distance in Figure 8.2, we identify a weak correlation where smaller nearest-neighbor distances correspond to higher oscillator strengths (with a Pearson correlation coefficient of $r = -0.3$, a more significant correlation than the correlation with cation atomic number which takes $r = -0.02$). This is not a surprising result given the inverse relationship of the crystal field coefficients $A_q^{(k)}$ with R_i, but it is interesting to see that a wide range of oscillator strengths may still be obtained for a given nearest-neighbor distance: the overall structure of the surrounding crystal host still plays an intricate and significant role on Er^{3+} brightness.

Having made our ionic radius correction and identified some initial trends in our results, there are a selection of materials that we identify as reasonable for attempting experimental characterization – reasonable in this case meaning that the material is a ternary compound

Material	*Materials Project ID*	*Er Site Note*	$f_{\mathrm{ED,calc}}$
$\mathbf{NaTaN_2}$	mp-5475	Either Ta or Na site	5.3×10^{-5}
$\mathbf{MoS_2}$	mp-1434	Mo site	5.2×10^{-5}
$\mathbf{Be_2C}$	mp-1569	Be site	3.8×10^{-5}
AlN	mp-1330	Al site	2.2×10^{-5}
$\mathbf{CeO_2}$	mp-20194	Ce site	6.9×10^{-6}
$\mathbf{Y_2O_3}$	mp-2652	C_2 Y site	1.1×10^{-6}
Rutile $\mathbf{TiO_2}$	mp-2657	Ti site	7.2×10^{-7}
Anatase $\mathbf{TiO_2}$	mp-390	Ti site	2.1×10^{-7}
$\mathbf{Y_2O_3}$	mp-2652	C_{3i} Y site	1.6×10^{-7}

Table 8.2: List of some possible hosts for Er^{3+} and their computed oscillator strengths $f_{\mathrm{ED,calc}}$. $NaTaN_2$, MoS_2, Be_2C, and AlN are targets for follow-up experimental investigation. CeO_2, Y_2O_3, and TiO_2 are all hosts already investigated by our group in thin film format.

or binary compound, that the material is safe to handle (e.g., not radioactive), and has been tagged as experimentally identified in Materials Project. These materials, along with materials previously studied in our group, are listed with their respective oscillator strengths in Table 8.2. $NaTaN_2$, MoS_2, Be_2C, and AlN are targets for follow-up experimental investigation – by obtaining bulk samples, ion implanting with Er and subsequently annealing to activate the Er ions (per the method utilized by Phenicie *et al.*[134]), we may experimentally verify via PLE experiments whether, for example, MoS_2 is indeed an order of magnitude brighter than CeO_2.

8.5 Remarks and next steps on exploration of Er hosts

We have calculated the oscillator strengths for a broad range of possible host materials for Er^{3+} defects. Based on these calculations, a careful selection of host could lead to order of magnitude greater Er emission rates – which, when combined with the nanophotonics engineering referenced earlier, could push Er-based systems into the 1 GHz bandwidth regime: a significant improvement towards usable quantum communication schemes.

There are, certainly, limitations in the current method. One such example was highlighted

in the discussion of small cation sites – such an artifact must be recognized by careful analysis of the database being developed. Additionally, this method is suitable primarily for ionic materials. Covalent materials such as silicon that are not well described by an array of point charges must be considered via more advanced methods such as density functional theory, to properly account for the charge distribution around a rare-earth ion embedded in its matrix. However, we demonstrated that we may start to identify trends across materials, such as decreasing nearest-neighbor distance roughly correlating with increasing oscillator strength.

Despite these limitations, this project shows promise in identifying new hosts for enhancing the Er^{3+} quantum memory system, and continues the development of using high-throughput computation to identify optimal host materials for qubit defects, in a similar manner to works such as Kanai *et al.*[31] As described in the previous section, the next step for this project is to obtain Er-doped samples of promising hosts to experimentally confirm their brightness, and thus verify our host selection process using this technique.

CHAPTER 9

CONCLUSIONS AND FINAL REMARKS

Over the course of this thesis we have taken three major steps in the advancement of quantum communication, taking a defect-first approach towards development of our chosen platform. First, we have identified a viable quantum communication qubit platform in Er:CeO_2(111) grown on Si(111), with half-microsecond coherence times. Second, we have extended the viability of Er:CeO_2 by demonstrating experimental results that may lead to improved device fabrication via growth on Si(001) substrates, and later silicon-on-insulator. Third, we have used knowledge of our defect to enable computational survey techniques – inspired by the technique that lead to the initial selection of CeO_2 – to target follow-up materials that could provide additional benefits, in this case faster optical transitions, in the development of rare-earth based quantum communication technologies.

This thesis has demonstrated a holistic approach to exploring qubit systems for quantum communication, beginning in Chapter 2 with a full exploration of the energy structure of our qubit defect from the body of scientific literature, with the goal of identifying all manner of structure inherent to the defect itself. Then, we applied a set of key approximations to restrict the description of the defect to that which is usable for experimental evaluation. Indeed, for Er^{3+}, we remove the atomic nature, Coulombic electron interactions, and spin-orbit interaction from experimental consideration and take them as given, focusing instead on the crystal field levels and spin system that are most relevant to the development of quantum communication platforms with Er^{3+}. This brings us into line with common experimental parlance, but now with improved understanding of the system with which we are working – for example, relating ensemble broadening to the spin-spin interaction term of the rare-earth Hamiltonian.

We apply this same approach of developing comprehensive understanding of our system to the growth and characterization of our thin film samples, through Chapters 3 to 5. Through

well-tuned growth windows, careful consideration of sample processing, detailed microstructural study, and fundamentally informed optical measurements, we are able to proceed to thorough optical and microstructural characterization of Er:CeO_2 thin films grown on silicon. Benchmarking this system in Chapter 6 leads to understanding the processes involved with inhomogeneous linewidth broadening for both the spin and optical transitions, identification of quenching and subsequent reduction thereof in the optical transition used for flying qubit interconversion, and measurement of coherence times nearing the microsecond regime. All these things together yield quantum memory platforms that take important steps towards viability for metropolitan-scale quantum networks.

In continuing to work towards that goal, in Chapter 7 we begin the adaptation of the Er:CeO_2 system from being grown on Si(111) to being grown on Si(001). We identify epitaxial growth, albeit not in the desired orientation – though with reasonable optical properties that could lead to additional gains in chip-scale integration for our systems. In an alternative route towards scalability, in Chapter 8 we use the Er^{3+} energy structure reviewed in Chapter 2 to identify additional host materials with an eye towards gains in communication bandwidth via fundamental engineering of the defect host.

All told, this thesis represents steady progress on the grand challenge of quantum communication. We invoke the fundamentals of qubit design from the defect and host perspective, while consistently judging our systems on the criteria of coherence and scalability.

APPENDIX A

FITTING CLAUSIUS-CLAPEYRON EQUATIONS FOR FLUX MEASUREMENTS

As described in Section 3.5, part of the process of setting up a growth window is taking reliable fluxes of the available precursor materials, such as metallic cerium.

Here we will show that ion gauge sensitivity with respect to different molecules will not change the vaporization enthalpy calculation of a fitted pressure-vs-temperature measurement series.

The general form of the Clausius-Clapeyron equation is as follows:

$$\ln\left(\frac{P}{P_{\text{ref}}}\right) = -\frac{\Delta H}{R}\left(\frac{1}{T} - \frac{1}{T_{\text{ref}}}\right) \tag{A.1}$$

We have here the measured pressure P in torr, a reference pressure P_{ref} which we take to be 1 torr, the enthalpy of vaporization ΔH, the ideal gas constant R, the measured temperature T, and a reference temperature T_{ref}. We may use this formula as a fit function based on this formula, with fit parameters ΔH and T_{ref}.

To account for chemical sensitivity, we acknowledge that the measured pressure P will not be accurate to the true pressure P_{true}, due to ion gauge sensitivity changing based on the identity of the impinging molecules. Generally, this sensitivity is identified as the ionization efficiency, though a metric on this is the correction factor R_x, defined as the "chemical sensitivity" of the gauge to different molecules based upon the polarizability of the molecular species.[135]

In this case, we are more interested in how pressures may scale with the chemical sensitivity, rather than the exact form of the chemical sensitivity itself:

$$R_x \approx \frac{P}{P_{\text{true}}} \quad \Rightarrow \quad P_{\text{true}} \approx \frac{P}{R_x} \tag{A.2}$$

This may be substituted into the Clausius-Clapeyron equation. Factoring the equation out, we find that it may be combined with T_{ref} to form a fit parameter $b = \Delta H/RT_{\text{ref}} + \ln R_x$.

$$\begin{aligned} \ln\left(\frac{P}{R_x}\right) &= -\frac{\Delta H}{R}\left(\frac{1}{T} - \frac{1}{T_{\text{ref}}}\right) \\ \ln P - \ln R_x &= -\frac{\Delta H}{R}\frac{1}{T} + \frac{\Delta H}{R}\frac{1}{T_{\text{ref}}} \\ \ln P &= -\frac{\Delta H}{RT} + b \end{aligned} \tag{A.3}$$

In practice, we are not overly concerned with the value of b, but rather than the flux of a given source may be accurately described by a Clausius-Clapeyron equation with some combination of constants. We may also refer to the fitted enthalpy of vaporatization ΔH to gauge that the value is in the correct regime for the source – effusion cell thermocouples may be inaccurate by offsets of up to 100 ℃, which perturbs the fitted enthalpy from its true value since the measurements of the temperature T are inaccurate. It is reassuring, however, when enthalpy values are near their expected literature values. A value within a factor of 2-5 may be taken as an indicator that the expected material is being observed, especially given that we know with certainty what material we are putting in a given effusion cell.

APPENDIX B

SPIN-SPIN INTERACTION LINEWIDTH BROADENING

In this Appendix, we will go over the calculation of the Er-Er dipole-dipole interaction broadening. The statistical theory of line broadening, which may be used to derive this specific interaction broadening, relies on four key assumptions:[61,90]

1. Only one type of defect is involved in broadening
2. The defect causes a shift in resonance frequency in such a way that the contributions from each defect is additive
3. Positions of defects are not correlated (or rather, defect concentration is low)
4. The lattice can be approximated by a continuous medium

Stoneham's 1969 work[90] takes these four assumptions plus a basic statistical approach and produces the following equation:

$$I(\Delta\epsilon) = \frac{1}{2\pi}\int_{-\infty}^{+\infty} dx e^{-ix\Delta\epsilon} e^{-\rho J(x)} \ , \quad J(x) = \int_V dz p(z)\big(1 - e^{ix\epsilon(z)}\big) \tag{B.1}$$

Here in Equation B.1, we obtain the lineshape $I(\Delta\epsilon)$ for a energy shift $\Delta\epsilon$ from the resonance center, caused by a population of spatially distributed defects with a volumetric density ρ (units of # per volume), where each defect contributes an energy shift ϵ based on the defect's configuration coordinate z, which occurs with probability $p(z)$.

In our case, we are using EPR to observe the resonance condition from the Zeeman effect, which is as follows with g-factor g, a microwave field with frequency ν, magnetic field B, the Planck constant h, and the Bohr magneton μ_B:

$$h\nu = g\mu_B B \tag{B.2}$$

To obtain the perturbation to the resonance due to another nearby spin, we can look at the electron spin Hamiltonian with and without a second nearby spin. For a single electron, the magnetic field potential is simply the following, now including the magnetic moment μ, vector magnetic field $\boldsymbol{B}$, vector spin state $\boldsymbol{S}$, and reduced Planck constant $\hbar = h/2\pi$.

$$H_M = -\boldsymbol{\mu} \cdot \boldsymbol{B} = \frac{g\mu_B}{\hbar} \boldsymbol{S} \cdot \boldsymbol{B} \tag{B.3}$$

We take the magnetic field to only reside in the $\hat{z}$ direction, and apply the fact that $S_z = (\hbar/2)\sigma_z$ where $\sigma_z = |\uparrow\rangle\langle\uparrow| - |\downarrow\rangle\langle\downarrow|$ is the z Pauli matrix.

$$H_M = \frac{g\mu_B}{\hbar} S_z B_z = \frac{1}{2} g\mu_B B \sigma_z \tag{B.4}$$

This Hamiltonian is already diagonalized, and the difference between the energies $E_\downarrow = \langle\downarrow| H_M |\downarrow\rangle$ and $E_\uparrow = \langle\uparrow| H_M |\uparrow\rangle$ yields the resonance condition in Eq. B.2.

Let there now be a system of two spins 1 and 2 with distinct g-factors and spins. The two spins interact via their magnetic dipoles. We designated our resonance perturbation $\epsilon(z)$ to be the impact on the 1 spin resonance condition as perturbed by the 2 spin. The total two-spin Hamiltonian H is as follows, where $\boldsymbol{\mu}_i = g_i \mu_B \boldsymbol{S}_i/\hbar$ are the magnetic dipole moments of each spin. We may compute the total Hamiltonian as follows, where we have the two individual spin terms followed by the dipole-dipole interaction term.†

$$H = -\boldsymbol{\mu}_1 \cdot \boldsymbol{B} - \boldsymbol{\mu}_2 \cdot \boldsymbol{B} - \frac{\mu_0}{4\pi|\boldsymbol{r}|^3}\Big(3(\boldsymbol{\mu}_1 \cdot \hat{r})(\boldsymbol{\mu}_2 \cdot \hat{r}) - \boldsymbol{\mu}_1 \cdot \boldsymbol{\mu}_2\Big) \tag{B.5}$$

Expanding the expression of the magnetic dipoles and using $\boldsymbol{S} = (\hbar/2)\boldsymbol{\sigma}$ where $\boldsymbol{\sigma}$ is the (unitless) Pauli vector:

†. Part of showing this derivation is to elucidate the modern parlance of units in these Hamiltonian terms. As such, we note that the magnetic moments have units of energy over magnetic field, and so the first two terms are obviously units of energy. The interaction term is more complex, starting with the vacuum permeability which has units of, in SI: $[T]^2[m]^3/[J]$. Then we have the distance $|\boldsymbol{r}|$ with units $[m]$, and the magnetic moments each with units $[J]/[T]$. So, we obtain units of energy for the overall term.

$$H = \frac{g_1\mu_B}{2}\boldsymbol{\sigma}_1 \cdot \boldsymbol{B} + \frac{g_2\mu_B}{2}\boldsymbol{\sigma}_2 \cdot \boldsymbol{B} - \frac{\mu_0 g_1 g_2 \mu_B^2}{8\pi|\boldsymbol{r}|^3}\Big(3(\boldsymbol{\sigma}_1 \cdot \hat{\boldsymbol{r}})(\boldsymbol{\sigma}_2 \cdot \hat{\boldsymbol{r}}) - \boldsymbol{\sigma}_1 \cdot \boldsymbol{\sigma}_2\Big) \tag{B.6}$$

This yields three terms: The first term, which sets of the resonance condition that we wish to see the perturbation upon; the second term, which is the Zeeman splitting of the second spin; and the third term, the interaction between the two spins, governed by the distance between them $|\boldsymbol{r}|$, and the the direction $\hat{\boldsymbol{r}}$.

We have chosen to apply our magnetic field in the $\hat{z}$ axis, and so we quantize our spins in $\hat{z}$ accordingly. This sets the magnetic field to B_z, and sets $\hat{r}$ to $\hat{z}$ with a distance defined by $z = r\cos\theta$. We may additionally neglect the final term in the expression $\boldsymbol{\sigma}_1 \cdot \boldsymbol{\sigma}_2$ by assuming a low concentration of interacting spins such that only two spins are interacting on any given occasion.[62]

$$\begin{aligned} H &= \frac{g_1\mu_B}{2}\sigma_{z,1}B_z + \frac{g_2\mu_B}{2}\sigma_{z,2}B_z - \frac{\mu_0 g_1 g_2 \mu_B^2}{8\pi|\boldsymbol{r}|^3}\Big(3(\sigma_{z,1} \cdot \hat{\boldsymbol{z}})(\sigma_{z,2} \cdot \hat{\boldsymbol{z}}) - \boldsymbol{\sigma}_1 \cdot \boldsymbol{\sigma}_2\Big) \\ &= \frac{g_1\mu_B}{2}\sigma_{z,1}B_z + \frac{g_2\mu_B}{2}\sigma_{z,2}B_z - \frac{\mu_0 g_1 g_2 \mu_B^2}{8\pi|\boldsymbol{r}|^3}(3\cos^2\theta - 1)\sigma_{z,1}\sigma_{z,2} \end{aligned} \tag{B.7}$$

Explicitly expressing our Hamiltonian in tensor products accounting for the two spin spaces, we obtain the following, which we can solve directly.

$$H = \frac{1}{2}g_1\mu_B B\sigma_{z,1} \otimes \mathbb{I}_2 + \frac{1}{2}g_2\mu_B B\mathbb{I}_1 \otimes \sigma_{z,1} - \frac{\mu_0 g_1 g_2 \mu_B^2}{8\pi|\boldsymbol{r}|^3}(3\cos^2\theta - 1)\sigma_{z,1} \otimes \sigma_{z,2} \tag{B.8}$$

$$= \alpha\sigma_{z,1} \otimes \mathbb{I}_2 + \beta\mathbb{I}_1 \otimes \sigma_{z,1} - \gamma\sigma_{z,1} \otimes \sigma_{z,2} \tag{B.9}$$

Once again this expression is already diagonalized in our spin basis, so we immediately extract the energies of each spin condition.

$$\begin{aligned} \langle\uparrow\uparrow|H|\uparrow\uparrow\rangle &= \alpha+\beta-\gamma & \langle\uparrow\downarrow|H|\uparrow\downarrow\rangle &= \alpha-\beta+\gamma \\ \langle\downarrow\uparrow|H|\downarrow\uparrow\rangle &= -\alpha+\beta+\gamma & \langle\downarrow\downarrow|H|\downarrow\downarrow\rangle &= -\alpha-\beta-\gamma \end{aligned} \tag{B.10}$$

We have two scenarios to evaluate the resonance condition (the difference between the first spin's up and down states), where the second spin is either up or down. Observe that the unperturbed resonance is 2α.

$$\begin{aligned} \text{2nd spin-up: } \langle\uparrow\uparrow|H|\uparrow\uparrow\rangle - \langle\downarrow\uparrow|H|\downarrow\uparrow\rangle &= (\alpha+\beta-\gamma)-(-\alpha+\beta+\gamma) = 2\alpha-2\gamma \\ \text{2nd spin-down: } \langle\uparrow\downarrow|H|\uparrow\downarrow\rangle - \langle\downarrow\downarrow|H|\downarrow\downarrow\rangle &= (\alpha-\beta+\gamma)-(-\alpha-\beta-\gamma) = 2\alpha+2\gamma \end{aligned} \tag{B.11}$$

Thus we have the two cases for the energy shift ϵ away from the resonance condition as a function of $\boldsymbol{r}$ and the two possible perturbing spin states.

$$\epsilon(\boldsymbol{r},\pm) = \pm 2\gamma = \pm\frac{\mu_0 g_1 g_2 \mu_B^2}{4\pi|\boldsymbol{r}|^3}(3\cos^2\theta-1) \tag{B.12}$$

For simplicity in writing this equation in the context of evaluating our lineshape, we fold all non-spatial values into a single parameter $a = \mu_0 g_1 g_2 \mu_B^2/4\pi h$, where we have now re-included h for obtaining frequency units at the output of our evaluation. Thus, we have expressed the shift in resonance frequency of spin 1 due to a proximal spin 2.

$$\epsilon(\boldsymbol{r},\pm) = \pm\frac{a}{|\boldsymbol{r}|^3}(3\cos^2\theta-1) \tag{B.13}$$

We may now apply this energy shift ϵ in the context of Equation B.1. We begin by evaluating the integral $J(x)$. Let us assume that our system is at sufficiently high temperature that the two spin states of the perturbing spin 2 are equally populated (a reasonable assumption for 4 K measurements). For integration over a volume defined with the spherical coordinates (r, θ, ϕ), along with integration over a spin coordinate m_s, we take

$p(z)dz = r^2 \sin\phi dr d\theta d\phi dm_s$. Thus our integration actually becomes a sum across two terms, one for spin-up and one for spin-down, each with half the total population of spins N.

$$\begin{aligned} J(x) &= \int_V dz p(z)\big(1 - e^{ix\epsilon(z)}\big) \\ &= \int_0^R r^2 dr \int_0^\pi \sin\phi d\phi \int_0^{2\pi} d\theta \int_{m_s=\pm 1} dm_s \times \big(1 - e^{ix\epsilon(r,\theta,m_s)}\big) \\ &= 2\int_0^R r^2 dr \int_0^{2\pi} d\theta \Big[\frac{N}{2}\big(1 - e^{ix\epsilon(r,\theta)}\big) + \frac{N}{2}\big(1 - e^{-ix\epsilon(r,\theta)}\big)\Big] \\ &= \frac{4\pi^2 a}{9\sqrt{3}} \cdot |x| \end{aligned} \tag{B.14}$$

We may then put $J(x)$ into the expression for $I(\Delta\epsilon)$ and integrate once again:

$$I(\Delta\epsilon) = \frac{1}{2\pi}\int_{-\infty}^{\infty} dx e^{-ix\Delta\epsilon} e^{-\rho\cdot 4\pi^2 a|x|/9\sqrt{3}} = \frac{1}{\pi}\frac{2\pi^3 a\rho/9\sqrt{3}}{\Delta\epsilon^2 + (2\pi^2 a\rho/9\sqrt{3})^2} \tag{B.15}$$

This is precisely the equation for a Lorentzian distribution, which we take to have a full-width half-max of $\Gamma_{\text{d-d}}$.

$$I(\Delta\epsilon) = \frac{1}{\pi}\frac{\Gamma_{\text{d-d}}/2}{\Delta\epsilon^2 + (\Gamma_{\text{d-d}}/2)^2}, \qquad \Gamma_{\text{d-d}} = \frac{4\pi^2}{9\sqrt{3}}\rho a = \frac{\pi}{9\sqrt{3}}\frac{\mu_0 g_1 g_2 \mu_B^2}{h}\cdot\rho \tag{B.16}$$

If we select $g_1 = g_2 = g$ and a density of spinful defects with that g-factor, then the broadening of the resonance line due of the spin ensemble due to itself is the following $\Gamma_{\text{d-d}}$:

$$\Gamma_{\text{d-d}} = \frac{\pi}{9\sqrt{3}}\frac{\mu_0 g^2 \mu_B^2}{h}\rho \tag{B.17}$$

Evaluating this concentration for a density of spin-1/2 Er defects with a g-factor of 6.812(5), $\Gamma_{\text{d-d}}(\rho = 2 \text{ ppm Er}) = 0.2$ MHz and $\Gamma_{\text{d-d}}(\rho = 130 \text{ ppm Er}) = 15.2$ MHz as mentioned in the main text.

APPENDIX C

ANALYSIS OF TRENDS IN OPTICAL CHARACTERIZATION

C.1 Fitting the inhomogeneous linewidth doping dependence

In Figure 6.6 we characterize the inhomogeneous linewidth of the Z_1-Y_1 transition as a function of Er concentration. The equation for the inhomogeneous linewidth is determined from two possible relationships between Er^{3+} emitters and surrounding defects. In one scenario, the interaction energy between the emitter and a nearby charged defect varies as $\sim 1/r^2$ (where r is the defect-to-emitter distance) and one expects $\Gamma_{\text{inh}} \propto n^{2/3}$ where n is the defect density.[90] Alternatively, the effects of strain, random electric field gradients, or dipole-dipole interactions with interaction energy $\sim 1/r^3$ result in a linear dependence $\Gamma_{\text{inh}} \propto n$. Taking the linear combination of these two dependencies plus a constant term for non-dopant-driven broadening yields the following generic equation for the inhomogeneous linewidth:

$$\Gamma_{\text{inh}}(n) = a + bn^{2/3} + cn \tag{C.1}$$

As stated in the text, we take $n \sim n_{\text{Er}}$ for fitting the equation. Setting $c = 0$ lets us focus on the $\sim 1/r^2$ case, where we obtain $a = 11(3)$ GHz and $b = 1.3(2)$ GHz per ppm$^{2/3}$ for a coefficient of determination $R^2 = 0.87$. Setting $b = 0$ lets us focus on the $\sim 1/r^3$ case, where we obtain $a = 15(3)$ GHz and $c = 0.23(5)$ GHz per ppm for $R^2 = 0.79$. Fitting the generic equation where both b and c may vary results in $c \to 0$ and the same values for a and b as in the $\sim 1/r^2$ case, except with larger standard errors due to the third free parameter. Because the $\sim 1/r^2$ case yields a higher R^2, we describe it as a slightly better fit. However, because the two scenarios both capture the behavior of the small dataset and because the two R^2 values are similar, we state that either interaction energy scaling is possible – the Er-defect interaction may be either $\sim 1/R^2$ (charge-dipole), or $\sim 1/R^3$ (strain or second order

Stark effect) – according to analysis with Stoneham's models.[90] We note that the $\sim 1/R^2$ dependence requires presence of a static dipole formed in the excited Er that is unexpected in the centrosymmetric CeO_2 lattice, and may only be possible due to lattice distortions presented by microstructural imperfections.

C.2 Fitting the excited state lifetime doping dependence

In Figure 6.7 we use the Inokuti-Hirayama model[88,91] to analyze the results of the optical excited state lifetime of the Z_1-Y_1 transition. The model considers an optically active emitter of intrinsic lifetime $T_1^{(0)}$ surrounded by defects that can nonradiatively quench the excitation. The energy transfer from the emitter to the defects may occur via dipole-dipole interaction or via higher order (dipole-quadrupole, etc.) interactions. The resulting radiative decay lifetime T_1 is given by the following two equations:[88]

$$\phi(t) = \phi_0 \exp\Big[-\frac{t}{T_1^{(0)}} - \Gamma\Big(1-\frac{3}{\nu}\Big)\frac{n}{n_0}\Big(\frac{t}{T_1^{(0)}}\Big)^{3/\nu}\Big] \tag{C.2}$$

$$T_1 = \int_0^\infty t\phi(t)dt \Big/ \int_0^\infty \phi(t)dt \tag{C.3}$$

These equations yield the mean lifetime of the emitter T_1 as a function of the intrinsic lifetime of the emitter ($T_1^{(0)}$) surrounded by a concentration of quenching defects n (# per volume). Here the parameter n_0 represents a 'critical concentration' of the quenching defects (# per volume). The type of interaction is governed by the parameter $\nu \in \{6, 8, 10\}$ for electric dipole-dipole, electric dipole-quadrupole, and electric quadrupole-quadrupole interactions respectively. Finally, the excited state population as a function of time $\phi(t)$ is normalized by the parameter ϕ_0 representing the the number of emitters.

To fit our lifetime data as a function of erbium doping level using the Inokuti-Hirayama model, we fit for T_1 by using the intrinsic lifetime $T_1^{(0)}$ and critical concentration n_0 as free

parameters. The normalization constant ϕ_0 is factored out in Equation C.3. Numerical integration is used to evaluate Equation C.3.

Running the fit on the lifetime data with $\nu = 6$ produces an intrinsic lifetime of $T_1^{(0)} = 3.42(3)$ ms as discussed in the main text, and also yields a critical concentration of $n_0 = 474(46)$ ppm, though the identity of the quenching defect is not discussed. We choose $\nu = 6$ due to the electric dipole-dipole interaction being the longest-range interaction, but fitting $\nu = 8$ and $\nu = 10$ yield fits of equivalent quality with the same intrinsic lifetime, the only change being that the critical concentrations are fitted to 219(21) ppm and 295(28) ppm respectively.

C.3 Fitting the spectral diffusion linewidth doping dependence

In Figure 6.8 we fit the spectral diffusion as a function of Er concentration to a linear model based on the expected broadening from instantaneous spectral diffusion caused by dipole-dipole interactions with nearby excited Er ions.[95] That equation is shown below, and fitting the equation to the data in Figure 6.8 results in $a = 10.7(9)$ MHz and $b = 90(50)$ MHz per ppm.

$$\Gamma_{\mathrm{SD}} = a + bn \tag{C.4}$$

C.4 Full treatment of the annealing derivation and conclusions

With annealing, the density of unintended defects drops, resulting in narrowing inhomogeneous broadening and lengthening T_1 of the Er emitters. Here we assume a kinetic equation with first order reaction rate for the annealing of the defects as a function of time:

$$\frac{dn}{dt} = -K\big(n - n_f\big) \tag{C.5}$$

Here, n is the density of defects, K is the reaction rate constant, and n_f is the defect concentration at thermal equilibrium. The thermally activated reaction rate constant K is given by the Arrhenius relation $K \propto \big(\exp\{-E_A/k_BT\}\big)$ where E_A is the activation energy for the defect to hop between lattice sites, k_B is the Boltzmann constant, and T is the sample temperature. Far from equilibrium, assuming $n \gg n_f$, we have from Equation C.5:

$$n(t) = n_i \exp\big(-Kt\big)\ ,\ K \propto \exp\big(-E_A/k_BT\big) \tag{C.6}$$

where the defect density drops to $n(t)$ after annealing for a duration t from the initial "grown-in" concentration n_i. Similar dependencies to Equation C.6 have been seen in other works on similar polar oxides[136,137] as well.

The power-law dependence of the inhomogeneous linewidth on concentration is established in Figure 6.6. As discussed, some ambiguity in the appropriate power-law remains. Thus, without loss of generality we may apply the generic model of $\Gamma_{\text{inh}} = a + bn_t^{\alpha}$ where n_t is the density of grown-in defects (that impact the linewidth) remaining after dwelling for time t during annealing, and α is the generic exponent. It is possible that these as-grown defects affect Γ_{inh} through strain interactions, in which case $\alpha = 1$, and the power law dependence reverts to that in Equation C.1 with $b = 0$. Combining this generic power law with Equation C.6 we thus have:

$$\Gamma_{\text{inh}} = a + bn_i^{\alpha} \exp\big(-\alpha Kt\big) \tag{C.7}$$

Since we do not know the intrinsic number of defects and the duration of annealing is held constant between samples, we absorb those parameters along with the generic exponent α into the fit parameters b' and c to obtain the following function to be used for fitting:

$$\Gamma_{\text{inh}} = a + b' \exp\Big(-c \exp\big(-E_A/k_BT\big)\Big) \tag{C.8}$$

where a, b', c, and E_A are fitting parameters. Fitting using an adaptive gradient descent optimizer[138] yields the fitted parameters $a = 6.2$ GHz, $b' = 2.7$ GHz, $c = 1090$, and the fitted activation energy $E_A = 0.66$ eV for the inhomogeneous linewidth, indicating consistency with our model for a reaction-limited annihilation of defects under annealing, with a reaction rate that is thermally activated, likely diffusion limited, and has an Arrhenius-like dependence on temperature.

The increase of the excited state lifetime with increased annealing temperature is modeled with the Inokuti-Hirayama approach as discussed before. Again, we assume in our model that the population of the quenching defects surrounding the erbium emitters are annealed out – for which a thermally activated kinetic model, same as Equation C.6 is considered. Thus, in Equation C.2 and C.3, we take $n = n_i \exp\big(-Kt\big)$, $K \propto \exp\big(-E_A/k_BT\big)$. This leads to the following equations for T_1 as a function of annealing time t:

$$\phi(t') = \phi_0 \exp\Big[-\frac{t'}{T_1^{(0)}} - \Gamma\Big(1-\frac{3}{\nu}\Big)\Big(\frac{n_i}{n_0}\Big)\exp\big(-Kt\big)\Big(\frac{t'}{T_1^{(0)}}\Big)^{3/\nu}\Big],\ K = c\exp\big(-E_A/k_BT\big) \tag{C.9}$$

$$T_1 = \int_0^\infty t'\phi(t')dt' \Big/ \int_0^\infty \phi(t')dt' \tag{C.10}$$

Here $T_1^{(0)}$, (n_i/n_0), c and E_A act as free parameters for fitting. Again, fitting using an adaptive gradient descent approach leads to a good fit (Figure 5(c)) with $T_1^{(0)} = 5.7$ ms, $(n_i/n_0) = 0.79$, $c = 950$, and $E_A = 0.72$ eV. We have taken $\nu = 6$ representing ED-ED interaction. This is in the same regime of E_A arrived at for the inhomogeneous linewidth variation, and points to a common density of grown in defects that are being annihilated via thermally activated processes, thus leading to improvement of the optical characteristics of the Er emitters.

REFERENCES

[1] David D. Awschalom, Hannes Bernien, Rex Brown, Aashish Clerk, Eric Chitambar, Alan Dibos, Jennifer Dionne, Mark Eriksson, Bill Fefferman, Greg David Fuchs, Jay Gambetta, Elizabeth Goldschmidt, Supratik Guha, F. Joseph Heremans, Kent David Irwin, Ania Bleszynski Jayich, Liang Jiang, Jonathan Karsch, Mark Kasevich, Shimon Kolkowitz, Paul G. Kwiat, Thaddeus Ladd, Jay Lowell, Dmitri Maslov, Nadya Mason, Anne Y. Matsuura, Robert McDermott, Rod van Meter, Aaron Miller, Jason Orcutt, Mark Saffman, Monika Schleier-Smith, Manish Kumar Singh, Phil Smith, Martin Suchara, Farzam Toudeh-Fallah, Matt Turlington, Benjamin Woods, and Tian Zhong. A roadmap for quantum interconnects. Technical report, Argonne National Lab. (ANL), Argonne, IL (United States), 2022.

[2] David P DiVincenzo. The physical implementation of quantum computation. *Fortschritte der Physik: Progress of Physics*, 48(9-11):771–783, 2000.

[3] Sheng-Kai Liao, Wen-Qi Cai, Wei-Yue Liu, Liang Zhang, Yang Li, Ji-Gang Ren, Juan Yin, Qi Shen, Yuan Cao, Zheng-Ping Li, Feng-Zhi Li, Xia-Wei Chen, Li-Hua Sun, Jian-Jun Jia, Jin-Cai Wu, Xiao-Jun Jiang, Jian-Feng Wang, Yong-Mei Huang, Qiang Wang, Yi-Lin Zhou, Lei Deng, Tao Xi, Lu Ma, Tai Hu, Qiang Zhang, Yu-Ao Chen, Nai-Le Liu, Xiang-Bin Wang, Zhen-Cai Zhu, Chao-Yang Lu, Rong Shu, Cheng-Zhi Peng, Jian-Yu Wang, and Jian-Wei Pan. Satellite-to-ground quantum key distribution. *Nature*, 549(7670):43–47, Sep 2017. ISSN 1476-4687. doi:10.1038/nature23655. URL `https://doi.org/10.1038/nature23655`.

[4] Ji-Gang Ren, Ping Xu, Hai-Lin Yong, Liang Zhang, Sheng-Kai Liao, Juan Yin, Wei-Yue Liu, Wen-Qi Cai, Meng Yang, Li Li, Kui-Xing Yang, Xuan Han, Yong-Qiang Yao, Ji Li, Hai-Yan Wu, Song Wan, Lei Liu, Ding-Quan Liu, Yao-Wu Kuang, Zhi-Ping He, Peng Shang, Cheng Guo, Ru-Hua Zheng, Kai Tian, Zhen-Cai Zhu, Nai-Le Liu, Chao-Yang Lu, Rong Shu, Yu-Ao Chen, Cheng-Zhi Peng, Jian-Yu Wang, and Jian-Wei Pan. Ground-to-satellite quantum teleportation. *Nature*, 549(7670):70–73, Sep 2017. ISSN 1476-4687. doi:10.1038/nature23675. URL `https://doi.org/10.1038/nature23675`.

[5] Joe Lykken and David Awschalom. Quantum link: Building the u.s. quantum superhighway. *OSTI*, 10 2018. URL `https://www.osti.gov/biblio/1569247`.

[6] Gary Wolfowicz, F. Joseph Heremans, Christopher P. Anderson, Shun Kanai, Hosung Seo, Adam Gali, Giulia Galli, and David D. Awschalom. Quantum guidelines for solid-state spin defects. *Nat. Rev. Mat.*, 6(10):906–925, 2021. doi:10.1038/s41578-021-00306-y.

[7] Vladimir Bužek and Mark Hillery. Quantum copying: Beyond the no-cloning theorem. *Physical Review A*, 54(3):1844, 1996.

[8] David Awschalom, Karl K. Berggren, Hannes Bernien, Sunil Bhave, Lincoln D. Carr, Paul Davids, Sophia E. Economou, Dirk Englund, Andrei Faraon, Martin Fejer, Saikat

Guha, Martin V. Gustafsson, Evelyn Hu, Liang Jiang, Jungsang Kim, Boris Korzh, Prem Kumar, Paul G. Kwiat, Marko Lončar, Mikhail D. Lukin, David A.B. Miller, Christopher Monroe, Sae Woo Nam, Prineha Narang, Jason S. Orcutt, Michael G. Raymer, Amir H. Safavi-Naeini, Maria Spiropulu, Kartik Srinivasan, Shuo Sun, Jelena Vučković, Edo Waks, Ronald Walsworth, Andrew M. Weiner, and Zheshen Zhang. Development of quantum interconnects (quics) for next-generation information technologies. *PRX Quant.*, 2(1):017002, 2021. doi:10.1103/PRXQuantum.2.017002.

[9] Manish Kumar Singh, Liang Jiang, David D Awschalom, and Supratik Guha. Key device and materials specifications for a repeater enabled quantum internet. *IEEE Transactions on Quantum Engineering*, 2:1–9, 2021.

[10] Sreraman Muralidharan, Linshu Li, Jungsang Kim, Norbert Lütkenhaus, Mikhail D. Lukin, and Liang Jiang. Optimal architectures for long distance quantum communication. *Scientific Reports*, 6(1):20463, Feb 2016. ISSN 2045-2322. doi:10.1038/srep20463. URL `https://doi.org/10.1038/srep20463`.

[11] Argonne National Laboratory. New quantum loop provides long national testbed for quantum communication technology. *Argonne Press Release*, 2020. URL `https://www.anl.gov/article/new-quantum-loop-provides-long-national-testbed-for-quantum-communication-technology`.

[12] Yisheng Lei, Faezeh Kimiaee Asadi, Tian Zhong, Alex Kuzmich, Christoph Simon, and Mahdi Hosseini. Quantum optical memory for entanglement distribution. *Optica*, 10(11):1511–1528, 2023.

[13] Khabat Heshami, Duncan G England, Peter C Humphreys, Philip J Bustard, Victor M Acosta, Joshua Nunn, and Benjamin J Sussman. Quantum memories: emerging applications and recent advances. *Journal of modern optics*, 63(20):2005–2028, 2016.

[14] Guokui Liu and Bernard Jacquier. *Spectroscopic properties of rare earths in optical materials*, volume 83 of *Springer Series in Materials Science*. Springer Science & Business Media, 2006. ISBN 9783642062834.

[15] Miloš Rančić, Morgan P Hedges, Rose L Ahlefeldt, and Matthew J Sellars. Coherence time of over a second in a telecom-compatible quantum memory storage material. *Nat. Phys.*, 14(1):50–54, 2018. doi:10.1038/nphys4254.

[16] Marianne Le Dantec, Miloš Rančić, Sen Lin, Eric Billaud, Vishal Ranjan, Daniel Flanigan, Sylvain Bertaina, Thierry Chanelière, Philippe Goldner, Andreas Erb, Ren Bao Liu, Daniel Estève, Denis Vion, Emmanuel Flurin, and Patrice Bertet. Twenty-three–millisecond electron spin coherence of erbium ions in a natural-abundance crystal. *Sci. Adv.*, 7(51):eabj9786, 2021. doi:sciadv.abj9786.

[17] Ian R Berkman, Alexey Lyasota, Gabriele G de Boo, John G Bartholomew, Shao Q Lim, Brett C Johnson, Jeffrey C McCallum, Bin-Bin Xu, Shouyi Xie, Nikolay V Abrosi-

mov, et al. Millisecond electron spin coherence time for erbium ions in silicon. *arXiv preprint arXiv:2307.10021*, 2023.

[18] Charles W Thiel, Thomas Böttger, and RL Cone. Rare-earth-doped materials for applications in quantum information storage and signal processing. *J. Lumin.*, 131(3): 353–361, 2011. doi:10.1016/j.jlumin.2010.12.015.

[19] Paul Stevenson, Christopher M Phenicie, Isaiah Gray, Sebastian P Horvath, Sacha Welinski, Austin M Ferrenti, Alban Ferrier, Philippe Goldner, Sujit Das, Ramamoorthy Ramesh, Robert J Cava, Nathalie P de Leon, and Jeff D Thompson. Erbium-implanted materials for quantum communication applications. *Phys. Rev. B*, 105(22):224106, 2022. doi:10.1103/PhysRevB.105.224106.

[20] Manish Kumar Singh, Gary Wolfowicz, Jianguo Wen, Sean E Sullivan, Abhinav Prakash, Alan M Dibos, David D Awschalom, F Joseph Heremans, and Supratik Guha. Development of a scalable quantum memory platform–materials science of erbium-doped TiO_2 thin films on silicon. *arXiv preprint 2202.05376v2*, 2022.

[21] Alan M Dibos, Michael T Solomon, Sean E Sullivan, Manish K Singh, Kathryn E Sautter, Connor P Horn, Gregory D Grant, Yulin Lin, Jianguo Wen, and F Joseph Heremans. Purcell enhancement of erbium ions in TiO_2 on silicon nanocavities. *Nano Lett.*, 22(16):6530–6536, 2022. doi:10.1021/acs.nanolett.2c01561.

[22] Cheng Ji, Michael T. Solomon, Gregory D. Grant, Koichi Tanaka, Muchuan Hua, Jianguo Wen, Sagar K. Seth, Connor P. Horn, Ignas Masiulionis, Manish K. Singh, Sean E. Sullivan, F. Joseph Heremans, David D. Awschalom, Supratik Guha, and Alan M. Dibos. Nanocavity-mediated purcell enhancement of Er in TiO_2 thin films grown via atomic layer deposition. *arXiv preprint arXiv:2309.13490*, 2023.

[23] Manish Kumar Singh, Abhinav Prakash, Gary Wolfowicz, Jianguo Wen, Yizhong Huang, Tijana Rajh, David D Awschalom, Tian Zhong, and Supratik Guha. Epitaxial Er-doped Y_2O_3 on silicon for quantum coherent devices. *APL Mater.*, 8(3): 031111, 2020. doi:10.1063/1.5142611.

[24] Shobhit Gupta, Shihan Liu, Chao-Fan Wang, Yizhong Huang, and Tian Zhong. Towards khz optical linewidth, millisecond spin coherence erbium telecom qubits in epitaxial thin films. In *CLEO: Fundamental Science*, pages FTh1A–2. Optica Publishing Group, 2023. doi:10.1364/CLEO_FS.2023.FTh1A.2.

[25] Salim Ourari, Łukasz Dusanowski, Sebastian P. Horvath, Mehmet T. Uysal, Christopher M. Phenicie, Paul Stevenson, Mouktik Raha, Songtao Chen, Robert J. Cava, Nathalie P. de Leon, and Jeff D. Thompson. Indistinguishable telecom band photons from a single er ion in the solid state. *Nature*, 620(7976):977–981, Aug 2023. ISSN 1476-4687. doi:10.1038/s41586-023-06281-4.

[26] Sebastian P Horvath, Christopher M Phenicie, Salim Ourari, Mehmet T Uysal, Songtao Chen, Łukasz Dusanowski, Mouktik Raha, Paul Stevenson, Adam T Turflinger,

Robert J Cava, Nathalie P de Leon, and Jeff D Thompson. Strong purcell enhancement of an optical magnetic dipole transition. *arXiv preprint arXiv:2307.03022*, 2023.

[27] Jake Rochman, Tian Xie, John G Bartholomew, KC Schwab, and Andrei Faraon. Microwave-to-optical transduction with erbium ions coupled to planar photonic and superconducting resonators. *Nat. Commun.*, 14(1):1153, 2023. doi:10.1038/s41467-023-36799-0.

[28] Yong Yu, Dorian Oser, Gaia Da Prato, Emanuele Urbinati, Javier Carrasco Ávila, Yu Zhang, Patrick Remy, Sara Marzban, Simon Gröblacher, and Wolfgang Tittel. Frequency tunable, cavity-enhanced single erbium quantum emitter in the telecom band. *arXiv preprint arXiv:2304.14685*, 2023.

[29] Lorenz Weiss, Andreas Gritsch, Benjamin Merkel, and Andreas Reiserer. Erbium dopants in nanophotonic silicon waveguides. *Optica*, 8(1):40–41, Jan 2021. doi:10.1364/OPTICA.413330.

[30] Stephan Rinner, Florian Burger, Andreas Gritsch, Jonas Schmitt, and Andreas Reiserer. Erbium emitters in commercially fabricated nanophotonic silicon waveguides. *Nanophotonics*, 12(17):3455–3462, 2023. doi:10.1515/nanoph-2023-0287.

[31] Shun Kanai, F Joseph Heremans, Hosung Seo, Gary Wolfowicz, Christopher P Anderson, Sean E Sullivan, Mykyta Onizhuk, Giulia Galli, David D Awschalom, and Hideo Ohno. Generalized scaling of spin qubit coherence in over 12,000 host materials. *Proc. Natl. Acad. Sci. U.S.A.*, 119(15):e2121808119, 2022. doi:10.1073/pnas.2121808119.

[32] Stefan Stoll and Arthur Schweiger. Easyspin, a comprehensive software package for spectral simulation and analysis in epr. *J. Magn. Reson.*, 178(1):42–55, 2006. doi:10.1016/j.jmr.2005.08.013.

[33] Andrei Faraon, Andrei Ruskuc, Ioana Craiciu, Jonathan M Kindem, John G Bartholomew, Jake H Rochman, and Mi Lei. Towards optical quantum networks based on rare-earth ions and nanophotonics. In *Quantum Computing, Communication, and Simulation*, volume 11699, page 116990Y. SPIE, 2021. doi:10.1117/12.2581709. URL `https://doi.org/10.1117/12.2581709`.

[34] Tian Zhong and Philippe Goldner. Emerging rare-earth doped material platforms for quantum nanophotonics. *Nanophotonics*, 8(11):2003–2015, 2019. doi:10.1515/nanoph-2019-0185. URL `https://doi.org/10.1515/nanoph-2019-0185`.

[35] Stacy Gates-Rector and Thomas Blanton. The powder diffraction file: a quality materials characterization database. *Powder Diffr.*, 34(4):352–360, 2019. doi:10.1017/S0885715619000812.

[36] Brian G Wybourne and William F Meggers. *Spectroscopic properties of rare earths*. American Institute of Physics, 1965. ISBN 9780470965078.

[37] Brian R Judd. *Operator techniques in atomic spectroscopy*. McGraw-Hill Book Company, Inc., 1963.

[38] M_ T_ Hutchings. Point-charge calculations of energy levels of magnetic ions in crystalline electric fields. In *Solid state physics*, volume 16, pages 227–273. Elsevier, 1964.

[39] Clyde A Morrison. Lectures on crystal field theory. *Presented at Recife*, 1982.

[40] Josette El Haddad, Bruno Bousquet, Lionel Canioni, and Patrick Mounaix. Review in terahertz spectral analysis. *TrAC Trends in Analytical Chemistry*, 44:98–105, 2013.

[41] LH Aller, CW Ufford, and JH Van Vleck. Multiplet intensities for the nebular lines^ {4} s-_ {2} d of omicr ii. *Astrophysical Journal, vol. 109, p. 42*, 109:42, 1949.

[42] David A Glocker, S Ismat Shah, and Cynthia A Morgan. *Handbook of thin film process technology*, volume 2. Institute of Physics Bristol, UK, 1995.

[43] Richard W Johnson, Adam Hultqvist, and Stacey F Bent. A brief review of atomic layer deposition: from fundamentals to applications. *Materials today*, 17(5):236–246, 2014.

[44] Yury Kuzminykh, Ali Dabirian, Michael Reinke, and Patrik Hoffmann. High vacuum chemical vapour deposition of oxides:: A review of technique development and precursor selection. *Surface and coatings technology*, 230:13–21, 2013.

[45] William Nunn, Tristan K Truttmann, and Bharat Jalan. A review of molecular-beam epitaxy of wide bandgap complex oxide semiconductors. *Journal of materials research*, pages 1–19, 2021.

[46] Robin FC Farrow. *Molecular beam epitaxy: applications to key materials*. Elsevier, 1995.

[47] Matthew Brahlek, Arnab Sen Gupta, Jason Lapano, Joseph Roth, Hai-Tian Zhang, Lei Zhang, Ryan Haislmaier, and Roman Engel-Herbert. Frontiers in the growth of complex oxide thin films: past, present, and future of hybrid mbe. *Advanced Functional Materials*, 28(9):1702772, 2018.

[48] W. Braun. *Applied RHEED: Reflection High-Energy Electron Diffraction During Crystal Growth*. Springer, 1999.

[49] Shuji Hasegawa. Reflection high-energy electron diffraction. *Characterization of Materials*, 97:1925–1938, 2012.

[50] Tomohiro Inaba, Takehiko Tawara, Hiroo Omi, Hideki Yamamoto, and Hideki Gotoh. Epitaxial growth and optical properties of Er-doped CeO_2 on Si(111). *Opt. Mater. Express*, 8(9):2843–2849, 2018. doi:10.1364/OME.8.002843.

[51] Werner Kern. Chapter 1 - overview and evolution of silicon wafer cleaning technology. In Karen A. Reinhardt and Werner Kern, editors, *Handbook of Silicon Wafer Cleaning Technology (Third Edition)*, pages 3–85. William Andrew Publishing, third edition edition, 2018. ISBN 9780323510844. doi:10.1016/B978-0-323-51084-4.00001-0. URL https://www.sciencedirect.com/science/article/pii/B9780323510844000010.

[52] Kristine A Bertness. Smart pyrometry for combined sample temperature and reflectance measurements in molecular-beam epitaxy. *J. Vac. Sci. Technol. B.*, 18(3): 1426–1430, 2000. doi:10.1116/1.591396.

[53] Joachim Mayer, Lucille A Giannuzzi, Takeo Kamino, and Joseph Michael. Tem sample preparation and fib-induced damage. *MRS Bull.*, 32(5):400–407, 2007. doi:10.1557/mrs2007.63.

[54] Ana Iglesias-Juez, Gian Luca Chiarello, Gregory S Patience, and M Olga Guerrero-Pérez. Experimental methods in chemical engineering: X-ray absorption spectroscopy—xas, xanes, exafs. *The Canadian Journal of Chemical Engineering*, 100 (1):3–22, 2022.

[55] Azad Mohammed and Avin Abdullah. Scanning electron microscopy (sem): A review. In *Proceedings of the 2018 International Conference on Hydraulics and Pneumatics—HERVEX, Băile Govora, Romania*, volume 2018, pages 7–9, 2018.

[56] Weilie Zhou, Robert Apkarian, Zhong Lin Wang, and David Joy. Fundamentals of scanning electron microscopy (sem). *Scanning microscopy for nanotechnology: techniques and applications*, pages 1–40, 2007.

[57] Beverley J Inkson. Scanning electron microscopy (sem) and transmission electron microscopy (tem) for materials characterization. In *Materials characterization using nondestructive evaluation (NDE) methods*, pages 17–43. Elsevier, 2016.

[58] Y Chen, Govind P Kothiyal, Jasprit Singh, and Pallab K Bhattacharya. Absorption and photoluminescence studies of the temperature dependence of exciton life time in lattice-matched and strained quantum well systems. *Superlattices and Microstructures*, 3(6):657–664, 1987.

[59] Marc Levenson. *Introduction to Nonlinear Laser Spectroscopy 2e*. Elsevier, 2012.

[60] Jiefei Zhang, Gregory D Grant, Ignas Masiulionis, Michael T Solomon, Jasleen K Bindra, Jens Niklas, Alan M Dibos, Oleg G Poluektov, F Joseph Heremans, Supratik Guha, and David D Awschalom. Optical and spin coherence of Er^{3+} in epitaxial CeO_2 on silicon. *arXiv preprint arXiv:2309.16785*, 2023.

[61] S Geschwind, editor. *Electron Paramagnetic Resonance*. Plenum Press, New York, 1972. ISBN 0306305801.

[62] A. Abragam and B. Bleaney. *Electron Paramagnetic Resonance of Transition Ions*. Dover Publications, 1986.

[63] Gregory D Grant, Jiefei Zhang, Ignas Masiulionis, Swarnabha Chattaraj, Kathryn E Sautter, Sean E Sullivan, Rishi Chebrolu, Yuzi Liu, Jessica B Martins, Jens Niklas, et al. Optical and microstructural characterization of er3+ doped epitaxial cerium oxide on silicon. *APL Materials*, 12(2), 2024.

[64] Thomas Böttger, CW Thiel, RL Cone, and Y Sun. Effects of magnetic field orientation on optical decoherence in er 3+: Y 2 sio 5. *Physical Review B—Condensed Matter and Materials Physics*, 79(11):115104, 2009.

[65] Mamoru Yoshimoto, Hirotoshi Nagata, Tadashi Tsukahara, and Hideomi Koinuma. In situ rheed observation of CeO_2 film growth on Si by laser ablation deposition in ultrahigh-vacuum. *Jpn. J. Appl. Phys.*, 29(7A):L1199, 1990. doi:10.1143/JJAP.29.L1199.

[66] Hirotoshi Nagata, Mamoru Yoshimoto, Hideomi Koinuma, Eungi Min, and Nobuhiko Haga. Type-b epitaxial growth of CeO_2 thin film on Si(111) substrate. *J. Cryst. Growth*, 123(1-2):1–4, 1992. doi:10.1016/0022-0248(92)90004-3.

[67] Yukie Nishikawa, Noburu Fukushima, Naoki Yasuda, Kohei Nakayama, and Sumio Ikegawa. Electrical properties of single crystalline CeO_2 high-k gate dielectrics directly grown on Si(111). *Jpn. J. Appl. Phys.*, 41(4S):2480, 2002. doi:10.1143/JJAP.41.2480.

[68] C Barth, C Laffon, R Olbrich, A Ranguis, Ph Parent, and M Reichling. A perfectly stoichiometric and flat CeO_2 (111) surface on a bulk-like ceria film. *Sci. Rep.*, 6(1): 21165, 2016. doi:10.1038/srep21165.

[69] Takehiko Tawara, Giacomo Mariani, Kaoru Shimizu, Hiroo Omi, Satoru Adachi, and Hideki Gotoh. Effect of isotopic purification on spectral-hole narrowing in $^{167}Er^{3+}$ hyperfine transitions. *Appl. Phys. Express*, 10(4):042801, 2017. doi:10.7567/APEX.10.042801.

[70] Sihao Wang, Likai Yang, Mohan Shen, Wei Fu, Yuntao Xu, Rufus L Cone, Charles W Thiel, and Hong X Tang. Er:$LiNbO_3$ with high optical coherence enabling optical thickness control. *Phys. Rev. Appl.*, 18(1):014069, 2022. doi:10.1103/PhysRevApplied.18.014069.

[71] Mouktik Raha, Songtao Chen, Christopher M Phenicie, Salim Ourari, Alan M Dibos, and Jeff D Thompson. Optical quantum nondemolition measurement of a single rare earth ion qubit. *Nature Communications*, 11(1):1605, 2020. ISSN 2041-1723. doi:10.1038/s41467-020-15138-7. URL `https://doi.org/10.1038/s41467-020-15138-7`.

[72] Sacha Welinski, Philip J. T. Woodburn, Nikolai Lauk, Rufus L. Cone, Christoph Simon, Philippe Goldner, and Charles W. Thiel. Electron spin coherence in optically excited states of rare-earth ions for microwave to optical quantum transducers. *Phys. Rev. Lett.*, 122:247401, Jun 2019. doi:10.1103/PhysRevLett.122.247401. URL `https://link.aps.org/doi/10.1103/PhysRevLett.122.247401`.

[73] Tian Xie, Jake Rochman, John G. Bartholomew, Andrei Ruskuc, Jonathan M. Kindem, Ioana Craiciu, Charles W. Thiel, Rufus L. Cone, and Andrei Faraon. Characterization of $er^{3+} : YVo_4$ for microwave to optical transduction. *Phys. Rev. B*, 104:054111, Aug 2021. doi:10.1103/PhysRevB.104.054111. URL `https://link.aps.org/doi/10.1103/PhysRevB.104.054111`.

[74] V Narayanan, S Guha, M Copel, NA Bojarczuk, PL Flaitz, and M Gribelyuk. Interfacial oxide formation and oxygen diffusion in rare earth oxide–silicon epitaxial heterostructures. *Appl. Phys. Lett.*, 81(22):4183–4185, 2002. doi:10.1063/1.1524692.

[75] BT Thole, G Van der Laan, JC Fuggle, GA Sawatzky, RC Karnatak, and J-M Esteva. 3d x-ray-absorption lines and the $3d^9\ 4f^{n+1}$ multiplets of the lanthanides. *Phys. Rev. B*, 32(8):5107, 1985. doi:10.1103/PhysRevB.32.5107.

[76] Vinod K Paidi, Dale L Brewe, John W Freeland, Charles A Roberts, and Johan van Lierop. Role of Ce 4f hybridization in the origin of magnetism in nanoceria. *Phys. Rev. B*, 99(18):180403, 2019. doi:10.1103/PhysRevB.99.180403.

[77] Shih-Yun Chen, Chi-Hang Tsai, Mei-Zi Huang, Der-Chung Yan, Tzu-Wen Huang, Alexandre Gloter, Chi-Liang Chen, Hong-Ji Lin, Chien-Te Chen, and Chung-Li Dong. Concentration dependence of oxygen vacancy on the magnetism of CeO_2 nanoparticles. *J. Phys. Chem. C*, 116(15):8707–8713, 2012. doi:10.1021/jp2065634.

[78] L.A.J. Garvie and P.R. Buseck. Determination of ce4+/ce3+ in electron-beam-damaged ceo2 by electron energy-loss spectroscopy. *J. Phys. Chem. Solids*, 60(12): 1943–1947, 1999. ISSN 0022-3697. doi:10.1016/S0022-3697(99)00218-8.

[79] Tetsuichiro Hayakawa, Kazuhiro Egashira, Masashi Arakawa, Tomonori Ito, Shun Sarugaku, Kota Ando, and Akira Terasaki. X-ray absorption spectroscopy of $Ce_2O_3^+$ and $Ce_2O_5^+$ near Ce m-edge. *J. Phys. B: At. Mol. Opt.*, 49(7):075101, 2016. doi:10.1088/0953-4075/49/7/075101.

[80] Andris Antuzevics. Epr characterization of erbium in glasses and glass ceramics. *J. Low Temp. Phys.*, 46(12):1149–1153, 2020. doi:10.1063/10.0002465.

[81] Philip Rieger. *Electron spin resonance: analysis and interpretation*. Royal Society of Chemistry, 2007. ISBN 9780854043552.

[82] OH Laguna, MA Centeno, Magali Boutonnet, and José Antonio Odriozola. Fe-doped ceria solids synthesized by the microemulsion method for co oxidation reactions. *Applied Catalysis B: Environmental*, 106(3-4):621–629, 2011.

[83] Cornelis A.J. Ammerlaan and I. De Maat-Gersdorf. Zeeman splitting factor of the Er^{3+} ion in a crystal field. *Appl. Magn. Reson.*, 21(1):13–33, 2001. ISSN 09379347. doi:10.1007/BF03162436.

[84] R. M. Rakhmatullin, I. N. Kurkin, V. V. Pavlov, and V. V. Semashko. Epr, optical, and dielectric spectroscopy of er-doped cerium dioxide nanoparticles. *Phys. Status Solidi B Basic Res.*, 251(8):1545–1551, 2014. ISSN 15213951. doi:10.1002/pssb.201451116.

[85] Robert D Shannon. Revised effective ionic radii and systematic studies of interatomic distances in halides and chalcogenides. *Acta Crystallogr. A*, 32(5):751–767, 1976. doi:10.1107/S0567739476001551.

[86] Licia Minervini, Matthew O Zacate, and Robin W Grimes. Defect cluster formation in M_2O_3-doped CeO_2. *Solid State Ion.*, 116(3-4):339–349, 1999. doi:10.1016/S0167-2738(98)00359-2.

[87] Huizhi Bao, Xin Chen, Jun Fang, Zhiquan Jiang, and Weixin Huang. Structure-activity relation of Fe_2O_3-CeO_2 composite catalysts in CO oxidation. *Catal. Lett.*, 125:160–167, 2008. doi:10.1007/s10562-008-9540-3.

[88] E. Wolf and J.C. Dainty. *Progress in Optics*. Number v. 14 in Progress in Optics. North-Holland Publishing Company, 1976. ISBN 9780720415148.

[89] FA Kröger and HJ Vink. Relations between the concentrations of imperfections in crystalline solids. In *Solid State Phys.*, volume 3, pages 307–435. Elsevier, 1956. doi:10.1016/S0081-1947(08)60135-6.

[90] AM Stoneham. Shapes of inhomogeneously broadened resonance lines in solids. *Rev. Mod. Phys.*, 41(1):82, 1969. doi:10.1103/RevModPhys.41.82.

[91] Mitio Inokuti and Fumio Hirayama. Influence of energy transfer by the exchange mechanism on donor luminescence. *J. Chem. Phys.*, 43(6):1978–1989, 1965. doi:10.1063/1.1697063.

[92] Gary Wolfowicz, Christopher P Anderson, Berk Diler, Oleg G Poluektov, F Joseph Heremans, and David D Awschalom. Vanadium spin qubits as telecom quantum emitters in silicon carbide. *Sci. Adv.*, 6(18):eaaz1192, 2020. doi:10.1126/sciadv.aaz1192.

[93] Lucio Robledo, Hannes Bernien, Toeno Van Der Sar, and Ronald Hanson. Spin dynamics in the optical cycle of single nitrogen-vacancy centres in diamond. *New J. Phys.*, 13(2):025013, 2011. doi:10.1088/1367-2630/13/2/025013.

[94] Thomas Böttger, Y Sun, CW Thiel, and RL Cone. Spectroscopy and dynamics of Er^{3+}: Y_2SiO_5 at 1.5 μm. *Phys. Rev. B*, 74(7):075107, 2006. doi:10.1103/PhysRevB.74.075107.

[95] Felix R Graf, Alois Renn, Gert Zumofen, and Urs P Wild. Photon-echo attenuation by dynamical processes in rare-earth-ion-doped crystals. *Phys. Rev. B*, 58(9):5462, 1998. doi:10.1103/PhysRevB.58.5462.

[96] I. D. Abella, N. A. Kurnit, and S. R. Hartmann. Photon echoes. *Phys. Rev.*, 141: 391–406, Jan 1966. doi:10.1103/PhysRev.141.391. URL `https://link.aps.org/doi/10.1103/PhysRev.141.391`.

[97] B. I. Halperin P. w. Anderson and c. M. Varma. Anomalous low-temperature thermal properties of glasses and spin glasses. *The Philosophical Magazine: A Journal of Theoretical Experimental and Applied Physics*, 25(1):1–9, 1972. doi:10.1080/14786437208229210. URL https://doi.org/10.1080/14786437208229210.

[98] D. L. Huber, M. M. Broer, and B. Golding. Low-temperature optical dephasing of rare-earth ions in glass. *Phys. Rev. Lett.*, 52:2281–2284, Jun 1984. doi:10.1103/PhysRevLett.52.2281. URL https://link.aps.org/doi/10.1103/PhysRevLett.52.2281.

[99] G. P. Flinn, K. W. Jang, Joseph Ganem, M. L. Jones, R. S. Meltzer, and R. M. Macfarlane. Sample-dependent optical dephasing in bulk crystalline samples of y_2o_3:eu^{3+}. *Phys. Rev. B*, 49:5821–5827, Mar 1994. doi:10.1103/PhysRevB.49.5821. URL https://link.aps.org/doi/10.1103/PhysRevB.49.5821.

[100] Flurin Könz, Y. Sun, C. W. Thiel, R. L. Cone, R. W. Equall, R. L. Hutcheson, and R. M. Macfarlane. Temperature and concentration dependence of optical dephasing, spectral-hole lifetime, and anisotropic absorption in eu^{3+}: Y_2sio_5. *Phys. Rev. B*, 68:085109, Aug 2003. doi:10.1103/PhysRevB.68.085109. URL https://link.aps.org/doi/10.1103/PhysRevB.68.085109.

[101] Y. Sun, C. W. Thiel, and R. L. Cone. Optical decoherence and energy level structure of $0.1\%tm^{3+}$:$linbo_3$. *Phys. Rev. B*, 85:165106, Apr 2012. doi:10.1103/PhysRevB.85.165106. URL https://link.aps.org/doi/10.1103/PhysRevB.85.165106.

[102] Diana Serrano, Senthil Kumar Kuppusamy, Benoît Heinrich, Olaf Fuhr, David Hunger, Mario Ruben, and Philippe Goldner. Ultra-narrow optical linewidths in rare-earth molecular crystals. *Nature*, 603(7900):241–246, 2022. ISSN 1476-4687. doi:10.1038/s41586-021-04316-2. URL https://doi.org/10.1038/s41586-021-04316-2.

[103] Rikuto Fukumori, Yizhong Huang, Jun Yang, Haitao Zhang, and Tian Zhong. Sub-kilohertz optical homogeneous linewidth and dephasing mechanisms in er^{3+}:y_2o_3 ceramics. *Phys. Rev. B*, 101:214202, Jun 2020. doi:10.1103/PhysRevB.101.214202. URL https://link.aps.org/doi/10.1103/PhysRevB.101.214202.

[104] Y Sun, C.W Thiel, R.L Cone, R.W Equall, and R.L Hutcheson. Recent progress in developing new rare earth materials for hole burning and coherent transient applications. *Journal of Luminescence*, 98(1):281–287, 2002. ISSN 0022-2313. doi:https://doi.org/10.1016/S0022-2313(02)00281-8. URL https://www.sciencedirect.com/science/article/pii/S0022231302002818. Proceedings of the Seventh International Meeting on Hole Burning, Single Molecules and Related Spectroscopies: Science and Applications.

[105] K.M Salikhov, S.A Dzuba, and A.M Raitsimring. The theory of electron spin-echo signal decay resulting from dipole-dipole interactions between paramagnetic centers in solids. *Journal of Magnetic Resonance (1969)*, 42(2):255–276, 1981. ISSN 0022-2364. doi:https://doi.org/10.1016/0022-2364(81)90216-X. URL https://www.sciencedirect.com/science/article/pii/002223648190216X.

[106] Tim R. Eichhorn, Claire A. McLellan, and Ania C. Bleszynski Jayich. Optimizing the formation of depth-confined nitrogen vacancy center spin ensembles in diamond for quantum sensing. *Phys. Rev. Mater.*, 3:113802, Nov 2019. doi:10.1103/PhysRevMaterials.3.113802. URL https://link.aps.org/doi/10.1103/PhysRevMaterials.3.113802.

[107] B. Car, L. Veissier, A. Louchet-Chauvet, J.-L. Le Gouët, and T. Chanelière. Optical study of the anisotropic erbium spin flip-flop dynamics. *Phys. Rev. B*, 100:165107, Oct 2019. doi:10.1103/PhysRevB.100.165107. URL https://link.aps.org/doi/10.1103/PhysRevB.100.165107.

[108] S. R. Hastings-Simon, B. Lauritzen, M. U. Staudt, J. L. M. van Mechelen, C. Simon, H. de Riedmatten, M. Afzelius, and N. Gisin. Zeeman-level lifetimes in $er^{3+} : y_2sio_5$. *Phys. Rev. B*, 78:085410, Aug 2008. doi:10.1103/PhysRevB.78.085410. URL https://link.aps.org/doi/10.1103/PhysRevB.78.085410.

[109] Danny EP Vanpoucke, Patrick Bultinck, Stefaan Cottenier, Veronique Van Speybroeck, and Isabel Van Driessche. Aliovalent doping of CeO_2: Dft study of oxidation state and vacancy effects. *J. Mater. Chem. A*, 2(33):13723–13737, 2014. doi:10.1039/C4TA02449D.

[110] Debarati Das, Jyoti Prakash, UK Goutam, S Manna, Santosh K Gupta, and K Sudarshan. Oxygen vacancy and valence engineering in CeO_2 through distinct sized ion doping and their impact on oxygen reduction reaction catalysis. *Dalton Trans.*, 51(48): 18572–18582, 2022. doi:10.1039/D2DT03198A.

[111] A. M. Dibos, M. Raha, C. M. Phenicie, and J. D. Thompson. Atomic source of single photons in the telecom band. *Phys. Rev. Lett.*, 120:243601, Jun 2018. doi:10.1103/PhysRevLett.120.243601. URL https://link.aps.org/doi/10.1103/PhysRevLett.120.243601.

[112] Jonathan M Kindem, Andrei Ruskuc, John G Bartholomew, Jake Rochman, Yan Qi Huan, and Andrei Faraon. Control and single-shot readout of an ion embedded in a nanophotonic cavity. *Nature*, 580(7802):201–204, 2020. ISSN 1476-4687. doi:10.1038/s41586-020-2160-9. URL https://doi.org/10.1038/s41586-020-2160-9.

[113] L. Jiang, J. S. Hodges, J. R. Maze, P. Maurer, J. M. Taylor, D. G. Cory, P. R. Hemmer, R. L. Walsworth, A. Yacoby, A. S. Zibrov, and M. D. Lukin. Repetitive readout of a single electronic spin via quantum logic with nuclear spin ancillae. *Science*, 326(5950):

267–272, 2009. doi:10.1126/science.1176496. URL https://www.science.org/doi/abs/10.1126/science.1176496.

[114] Sang-Yun Lee, Matthias Widmann, Torsten Rendler, Marcus W Doherty, Thomas M Babinec, Sen Yang, Moritz Eyer, Petr Siyushev, Birgit J M Hausmann, Marko Loncar, Zoltán Bodrog, Adam Gali, Neil B Manson, Helmut Fedder, and Jörg Wrachtrup. Readout and control of a single nuclear spin with a metastable electron spin ancilla. *Nature Nanotechnology*, 8(7):487–492, 2013. ISSN 1748-3395. doi:10.1038/nnano.2013.104. URL https://doi.org/10.1038/nnano.2013.104.

[115] T Inoue, T Ohsuna, L Luo, XD Wu, CJ Maggiore, Y Yamamoto, Y Sakurai, and JH Chang. Growth of (110)-oriented ceo2 layers on (100) silicon substrates. *Applied physics letters*, 59(27):3604–3606, 1991.

[116] Tadahiko Hirai, Kazuhiro Teramoto, Hiroshi Koike, Kazuhito Nagashima Kazuhito Nagashima, and Yasuo Tarui Yasuo Tarui. Initial stage and growth process of ceria, yttria-stabilized-zirconia and ceria-zirconia mixture thin films on Si(100) surfaces. *Jpn. J. Appl. Phys.*, 36(8R):5253, 1997. doi:10.1143/JJAP.36.5253.

[117] T Ami, Y Ishida, N Nagasawa, A Machida, and M Suzuki. Room-temperature epitaxial growth of CeO_2(001) thin films on Si(001) substrates by electron beam evaporation. *Appl. Phys. Lett.*, 78(10):1361–1363, 2001. doi:10.1063/1.1351849.

[118] Jun Zhang, WEI Feng, YANG Zhimin, CHEN Qiuyun, CHEN Jun, and WANG Shuming. Structure and chemical states of highly eptiaxial ceo2 (001) films grown on srtio3 substrate by laser molecular beam epitaxy. *Journal of Rare Earths*, 31(12):1191–1194, 2013.

[119] Tomoyasu Inoue, Tetsu Ohsuna, Yasuhiro Obara, Yasuhiro Yamamoto, Masataka Satoh, and Yoshinobu Sakurai. Stripe-shaped facetted morphology and domain structure of epitaxial CeO_2(110) layers on Si(100) substrates. *J. Cryst. Growth*, 131(3-4): 347–351, 1993. doi:10.1016/0022-0248(93)90184-X.

[120] Anubhav Jain, Shyue Ping Ong, Geoffroy Hautier, Wei Chen, William Davidson Richards, Stephen Dacek, Shreyas Cholia, Dan Gunter, David Skinner, Gerbrand Ceder, et al. Commentary: The materials project: A materials genome approach to accelerating materials innovation. *APL materials*, 1(1), 2013.

[121] Robert C Hilborn. Einstein coefficients, cross sections, f values, dipole moments, and all that. *Am. J. Phys*, 50(11):982–986, 1982.

[122] W To Carnall, PR Fields, and BG Wybourne. Spectral intensities of the trivalent lanthanides and actinides in solution. i. pr3+, nd3+, er3+, tm3+, and yb3+. *The Journal of Chemical Physics*, 42(11):3797–3806, 1965.

[123] Brian R Judd. Optical absorption intensities of rare-earth ions. *Physical review*, 127 (3):750, 1962.

[124] GS Ofelt. Intensities of crystal spectra of rare-earth ions. *The journal of chemical physics*, 37(3):511–520, 1962.

[125] M. Rotenberg. *The 3-j and 6-j Symbols*. Number pt. 2 in The 3-j and 6-j Symbols. Technology Press, Massachusetts Institute of Technology, 1959. URL `https://books.google.com/books?id=1LwNAQAAIAAJ`.

[126] Arthur J Freeman and RE Watson. Theoretical investigation of some magnetic and spectroscopic properties of rare-earth ions. *Physical Review*, 127(6):2058, 1962.

[127] KMS Saxena and Gulzari Malli. Accurate numerical hartree-fock self-consistent-field wave functions for rare-earth ions. *Physical Review A*, 3(4):1278, 1971.

[128] MA Coulthard. Relativistic hartree-fock calculations of some properties of rare earth atoms and ions. *Journal of Physics B: Atomic and Molecular Physics*, 6(11):2224, 1973.

[129] B Hourahine, S Sanna, B Aradi, C Köhler, and Th Frauenheim. A theoretical study of erbium in gan. *Physica B: Condensed Matter*, 376:512–515, 2006.

[130] CW Nielson and George F. Koster. *Spectroscopic coefficients for the p^n, d^n, and f^n configurations*. MIT Press, 1963.

[131] Aaron Meurer, Christopher P Smith, Mateusz Paprocki, Ondřej Čertík, Sergey B Kirpichev, Matthew Rocklin, AMiT Kumar, Sergiu Ivanov, Jason K Moore, Sartaj Singh, et al. Sympy: symbolic computing in python. *PeerJ Computer Science*, 3:e103, 2017.

[132] Shyue Ping Ong, William Davidson Richards, Anubhav Jain, Geoffroy Hautier, Michael Kocher, Shreyas Cholia, Dan Gunter, Vincent L Chevrier, Kristin A Persson, and Gerbrand Ceder. Python materials genomics (pymatgen): A robust, open-source python library for materials analysis. *Computational Materials Science*, 68:314–319, 2013.

[133] RD t Shannon and CT Prewitt. Revised values of effective ionic radii. *Acta Crystallographica Section B: Structural Crystallography and Crystal Chemistry*, 26(7):1046–1048, 1970.

[134] Christopher M. Phenicie, Paul Stevenson, Sacha Welinski, Brendon C. Rose, Abraham T. Asfaw, Robert J. Cava, Stephen A. Lyon, Nathalie P. de Leon, and Jeff D. Thompson. Narrow optical line widths in erbium implanted in tio2. *Nano Letters*, 19 (12):8928–8933, Dec 2019. ISSN 1530-6984. doi:10.1021/acs.nanolett.9b03831. URL `https://doi.org/10.1021/acs.nanolett.9b03831`.

[135] John E Bartmess and Rosina M Georgiadis. Empirical methods for determination of ionization gauge relative sensitivities for different gases. *Vacuum*, 33(3):149–153, 1983.

[136] HY Xu, YH Huang, S Liu, KW Xu, F Ma, and Paul K Chu. Effects of annealing ambient on oxygen vacancies and phase transition temperature of VO_2 thin films. *RSC Adv.*, 6(83):79383–79388, 2016. doi:10.1039/C6RA13189A.

[137] AI Popov, MA Monge, R González, Y Chen, and EA Kotomin. Dynamics of f-center annihilation in thermochemically reduced MgO single crystals. *Solid State Commun.*, 118(3):163–167, 2001. doi:10.1016/S0038-1098(01)00062-X.

[138] Diederik P Kingma and Jimmy Ba. Adam: A method for stochastic optimization. *arXiv preprint arXiv:1412.6980*, 2014.

[139] Koichi Momma and Fujio Izumi. Vesta 3 for three-dimensional visualization of crystal, volumetric and morphology data. *Journal of applied crystallography*, 44(6):1272–1276, 2011.